UNIVERSITY OF CALIFORNIA, SAN DIEGO

Broadband Synthetic Aperture Matched Field Geoacoustic Inversion

A dissertation submitted in partial satisfaction of the
requirements for the degree
Doctor of Philosophy

in

Electrical Engineering
(Signal and Image Processing)

by

Bien Aik Tan

Committee in charge:

Professor William S. Hodgkiss, Chair
Professor Peter Gerstoft, Co-Chair
Professor William A. Coles
Professor William A. Kuperman
Professor Barnaby J. Rickett
Doctor Caglar Yardim

2014

The dissertation of Bien Aik Tan is approved, and it is acceptable in quality and form for publication on microfilm and electronically:

_____

_____

_____

_____

_____
Co-Chair

_____
Chair

University of California, San Diego

2014

DEDICATION

To my Father and Mother. For always being my pillars of support. I want to make them proud.

To Nina, my wife. I like to thank her for the love, support and encouragement she had given me.

To Charlotte, my daugther. She is my bundle of joy.

TABLE OF CONTENTS

Signature Page iii

Dedication iv

Table of Contents v

List of Figures vii

List of Tables xi

Acknowledgements xii

Vita xiv

Abstract of the Dissertation xvi

Chapter 1 Introduction 1

Chapter 2 Broadband synthetic aperture geoacoustic inversion 8
2.1 Introduction 8
2.2 Theory 9
2.2.1 Waveguide Doppler - normal mode representation 9
2.2.2 Likelihood and cost functions 20
2.2.3 Synthetic Aperture Formation 24
2.2.4 Source Spectrum 24
2.3 Simulations 25
2.3.1 Sensitivity analysis for static source and receiver with a single LFM pulse 26
2.3.2 Multiple LFM pulses for a static source and receiver 27
2.3.3 Multiple LFM pulses for a moving source and static receiver 29
2.4 Experimental Data Analysis 33
2.4.1 Matched-field geoacoustic inversion 37
2.5 Conclusions 41

Chapter 3 Recursive Bayesian synthetic aperture geoacoustic inversion in the presence of motion dynamics 45
3.1 Introduction 45
3.2 Theory 46
3.2.1 Waveguide Doppler theory model for acceleration dynamics 48
3.2.2 Likelihood functions 51

3.2.3 Recursive Bayesian estimation 52
3.2.4 Recursive Monte Carlo integration and importance sampling 54
3.2.5 Adaptive importance sampling 56
3.3 Recursive Bayesian Simulation 58
3.4 Experimental Data Analysis 66
3.4.1 Data preprocessing and inversion results 67
3.5 Conclusions 75

Chapter 4 Change-point detection for recursive Bayesian geoacoustic inversions 77
4.1 Introduction 77
4.2 Theory 79
4.2.1 Change-point detection 79
4.3 Simulation 82
4.4 Conclusions 88

Chapter 5 Conclusion and Future Research 91
5.1 Conclusion 91
5.2 Future Work 92

Bibliography 94

LIST OF FIGURES

Figure 1.1: Generic inversion model 1
Figure 1.2: Typical matched field geoacoustic inversion in a (a) towed source and bottom moored horizontal and vertical line array receiver configurations and (b) a bottom moored source and a towed horizontal line array receiver configuration. 2
Figure 1.3: Horizontally stratified ocean with a horizontally moving source and receiver. The source is moving at initial velocity $\mathbf{v}_{s1}$ and bearing φ_{s1}, while the receiver is moving at initial velocity $\mathbf{v}_{r1}$ and bearing φ_{r1}. 3
Figure 1.4: (a) Top view of a constant velocity source with changing radial velocity to the receiver. (b) Source–receiver range and radial velocity curves near CPA. Here, the change in source radial velocity in the dotted box approximately is linear. 6

Figure 2.1: Horizontally stratified ocean with horizontally moving source and receiver. The source is moving at velocity $\mathbf{v}_s$ and bearing φ_s, while the receiver is moving at velocity $\mathbf{v}_r$ and bearing φ_r. . 10
Figure 2.2: A single source frequency ω_s maps to several mode-dependent propagation frequencies ω due to source motion and undergoes further different shifts into receiver frequencies ω_r due to receiver motion. 18
Figure 2.3: Frequency and modal dispersion from the waveguide Doppler effect for a $f_s = 500$ Hz harmonic source using the KRAKEN model. (a) Static case overlaid with moving source case (b) Static case overlaid with moving receiver case. 21
Figure 2.4: A section of the 100–900 Hz ($T_r = T = 1$ s) source spectrum for $P = [1, 4, 32]$ LFM pulses in (a) magnitude and (b) phase. . 26
Figure 2.5: Sensitivity plots for a static source / receiver case. 28
Figure 2.6: Histograms of four-parameter inversions for the static source and receiver case. The histograms are for the Monte Carlo simulation corresponding to 200 noise realizations with SNR fixed at -6 dB and number of LFM pulses $P = [1, 2, 4, 8, 16, 32, 64]$. . 29
Figure 2.7: Histograms of four-parameter inversions for the moving source / static receiver case, SNR $= -6$ dB, and number of LFM pulses P with corresponding synthetic aperture of [2.5, 5, 10, 20, 40, 80, 160] m for (a) Uniform Doppler, and (b) Waveguide Doppler. 32
Figure 2.8: (a) Simulated received spectrum (499–501 Hz) for P=[1, 4, 32] with corresponding synthetic aperture of [2.5, 10, 80] m. (b) Same as (a) but prior to modal summation. 34

Figure 2.9: Histograms of four-parameter waveguide Doppler based inversions for the moving source / static receiver case, SNR = −6 dB and number of LFM pulses P with corresponding synthetic aperture of [2.5, 5, 10, 20, 40, 80, 160] m. 35
Figure 2.10: SW06 experiment site, bathymetry, source and receiver positions on JD238 (26 Aug 2006) 2000–2059 UTC. 36
Figure 2.11: Power spectral density of received signal 36
Figure 2.12: (a) SW06 SHARK interpolated sound speed profile from 1830–2229 UTC. Temperature sensor depths (×): 2, 4, 6, 7, 11, 13, 15, 18, 22, 26, 33, 41, 56, 71, 78 m. (b) Mean SSP and EOFs derived from SHARK SSPs. 38
Figure 2.13: Section of SW06 received signal spectrum with LFM pulses $P = [1, 4, 64]$. 39
Figure 2.14: SW06 64 s data inversion scatter plots for [z_s, z_w, v_s, h_{sed}] and $P = 64$ with a synthetic aperture of 160 m for (a) waveguide Doppler model and (b) uniform Doppler model. 42
Figure 2.15: SW06 64 s data inversion scatter plots for [ρ_{sed}, c_1, s, c_{bot}], and $P = 64$ with a synthetic aperture of 160 m for (a) waveguide Doppler model and (b) uniform Doppler model. 43
Figure 2.16: SSP inversion results using SW06 experimental data and $P = 64$ with waveguide Doppler and uniform Doppler models. 44

Figure 3.1: Horizontally stratified ocean with a horizontally moving source and receiver. The source is moving at initial velocity $\mathbf{v}_{s1}$ and bearing φ_{s1}, while the receiver is moving at initial velocity $\mathbf{v}_{r1}$ and bearing φ_{r1}. 47
Figure 3.2: Recursive Bayesian approach. The lth measurement is $\mathbf{y}_l$ and $\mathbf{m}$ is the vector of model parameters. For illustration purpose, $\mathbf{m}$ is depicted here as a scalar. The posterior density $p(\mathbf{m}|\mathbf{y}_{1:l})$ is represented with a set of samples of $\mathbf{m}$ and weights. 48
Figure 3.3: (a) Top view of a constant velocity source with changing radial velocity to the receiver. (b) Source–receiver range and radial velocity curves near CPA. Here, the change in source radial velocity in the dotted box approximately is linear. 49
Figure 3.4: Importance density evolution with l. 57
Figure 3.5: True marginal PPD via 24^4 exhaustive-search based samples with SNR fixed at 0 dB and number of LFM pulses (a) $L = 1$ (b) $L = 64$. (c) Estimated marginal PPD via AIS 18120 samples with SNR fixed at 0 dB and number of LFM pulses $L = 64$. . . 63
Figure 3.6: True 1-D marginal PPD evolution with $L = 1, \ldots, 64$: (a) acceleration not modeled in the replica field (b) acceleration modeled in the replica field. (c) Estimated 1-D marginal PPD evolution with $[L = 1, \ldots, 64]$ with acceleration modeled. 64

Figure 3.7: AIS importance distribution $x(\mathbf{m}; L)$ marginalized onto α_{sed} for $L = [1, 32, 64]$. 65
Figure 3.8: Likelihood function $p(\mathbf{y}_{1:64}|m_i)$ while fixing the remaining model parameters to the baseline value (see Table 3.3) for moving/static source-receiver configurations. 66
Figure 3.9: SW06 experiment site, bathymetry, source and receiver positions on JD238 (26 Aug 2006) 2000–2059 UTC. 68
Figure 3.10: R/V Knorr range and radial velocity to VLA1. Highlighted is the period of time corresponding to the 64 s data analyzed. . . 68
Figure 3.11: LFM pulse matched filtering for coarse synchronization. 69
Figure 3.12: SW06 data recursive Bayesian inversion results using the waveguide Doppler model with acceleration modeled in the replica for $L = 1$. 72
Figure 3.13: SW06 data recursive Bayesian inversion results using the waveguide Doppler model with no acceleration modeled in the replica for $L = 64$. 73
Figure 3.14: SW06 data recursive Bayesian inversion results using the waveguide Doppler model with acceleration modeled in the replica for $L = 64$. 74

Figure 4.1: Horizontally stratified ocean with a horizontally moving source and receiver. The source is moving at initial velocity $\mathbf{v}_{s1}$ and bearing φ_{s1} while the receiver is moving at initial velocity $\mathbf{v}_{r1}$ and bearing φ_{r1}. 84
Figure 4.2: Source and receiver are moving in the same r_x direction and at the same speed. Shown above are the source and receiver positions just prior and after the abrupt change in sediment thickness. 84
Figure 4.3: Evolution of 1-D marginal PPD with SNR fixed at 0 dB, and number of LFM pulses $L = 1$ to 128 with change-point detected at $r = 64$. Only the 95% HPD portion (non-white) PPD is plotted. 85
Figure 4.4: Evolution of change-point likelihood L with SNR fixed at 0 dB, and number of LFM pulses $L = 1$ to 71 with change-point detected ($\beta = 10$ dB) at $r = 64$ and $L = 71$. 86
Figure 4.5: Evolution of 1-D marginal PPD with SNR fixed at 0 dB, and number of LFM pulses $L = 1$ to 128 without change-point detection. The inversion (based on constant model parameters) is allowed to proceed despite an abrupt change. 87
Figure 4.6: The source-receiver separation is constant and the geoacoustic properties are assume range-independent in the r_y direction. Shown above are the source and receiver positions in the midst of gradual change in sediment thickness. 88

Figure 4.7: Evolution of 1-D marginal PPD with SNR fixed at 0 dB, and number of LFM pulses $L = 1$ to 128 with change-point detection. True sediment thickness changes gradually from 22 m to 17 m. Only the 95% HPD portion (non-white) PPD is plotted. 89
Figure 4.8: Evolution of change-point likelihood L with SNR fixed at 0 dB, and number of LFM pulses $L = 1$ to 63 with change-point detected on gradual change in H_{sed} ($\beta = 10$ dB) at $r = 41$ and $L = 63$. 90

LIST OF TABLES

Table 2.1: Source, propagation and receiver frequencies mapping relationships. 18
Table 2.2: Baseline model parameters. 27
Table 2.3: SW06 data inversion parameters search bounds and results for $P = 64$. 40

Table 3.1: Assumptions for the forward model and inversion approach. . . . 60
Table 3.2: Pseudo code for recursive Bayesian estimation using adaptive importance sampling. 61
Table 3.3: Baseline model parameters. 62
Table 3.4: Mapping relationships for the source, propagation and receiver frequencies. 70
Table 3.5: SW06 data inversion parameters prior bounds and MAP results for $L = 64$. 71

Table 4.1: Baseline model parameters. 83

ACKNOWLEDGEMENTS

I would like to thank my advisors Professors William Hodgkiss, Peter Gerstoft, and Dr. Caglar Yardim for their invaluable guidance, encouragement, patience and support during my Ph.D. work. Bill has kept me on track for my Ph.D. and is supportive of my research directions which were critical when research work don't seem to be getting results. I am grateful for Peter who is always available for countless discussions and kindly hosted parties for the research group. I thank Caglar for sharing his knowledge and experience with me.

I am also thankful to my thesis committee members Professors William Coles, William Kuperman and Barnaby Rickett for being wonderful mentors and supporters. They gave constructive feedback and help improved my Ph.D.. Professor William Kuperman is an excellent instructor for the computation ocean acoustic course which gave me the much-needed underwater acoustic foundation for my Ph.D. work. He also took time off his busy schedule to advise me on my Ph.D. and waveguide Doppler.

I would like to thank everybody at the Marine Physical Laboratory (MPL) for their help and friendship. I like to express gratitude to Dr. Hee Chun Song for many discussions on waveguide Doppler and underwater acoustic communications. I also had the privilege to work with him in his Pacific Ocean research cruise for long-range acoustic communications. I also like to thank Dave Ensberg for his help on the research logs and data on the Shallow Water 2006 experiment.

This Ph.D. work is supported by DSO National Laboratories of Singapore and the Office of Naval Research Grant No. N00014-11-0320, to them I would like to express my profound thanks for their financial support.

Especially I feel blessed by having a really supportive and understanding family. My father, mother, wife, daughter and sisters. I love them all.

This dissertation is a collection of papers that were published or submitted for publication. Chapter 2, in portion, is a reprint of material in the Journal of Acoustical Society of America as: B.A. Tan, P. Gerstoft, C. Yardim, W. Hodgkiss, "Broadband synthetic aperture geoacoustic inversion", *J. Acoust. Soc. Am.*, 134(1), 312–322, 2013.

Chapter 3, in full, is a reprint of material in the Journal of Acoustical Society of America as: B.A. Tan, P. Gerstoft, C. Yardim, W. Hodgkiss, "Recursive Bayesian synthetic aperture geoacoustic inversion in the presence of motion dynamics", *J. Acoust. Soc. Am.*, in press, 2014.

Chapter 4 is being prepared for submission to *J. Acoust. Soc. Am.* as: B. A. Tan, P. Gerstoft, C. Yardim, W. S. Hodgkiss, "Change-point detection for recursive Bayesian geoacoustic inversions".

VITA

2001	Bachelor of Engineering, Department of Electrical and Computer Engineering, National University of Singapore
2006	Master of Engineering, Department of Electrical and Computer Engineering, and Temasek Marine Science Institute, National University of Singapore
2014	Doctor of Philosophy in Electrical Engineering (Signal and Image Processing), University of California, San Diego
2001–Present	Senior Member of Technical Staff, DSO National Laboratories, Singapore

PUBLICATIONS

Journals

B. A. Tan, P. Gerstoft, C. Yardim, W. S. Hodgkiss, "Broadband synthetic aperture geoacoustic inversion", *J. Acoust. Soc. Am.*, vol. 134, no. 1, pp. 312-322, 2013.

B. A. Tan, P. Gerstoft, C. Yardim, W. S. Hodgkiss, "Recursive Bayesian synthetic aperture geoacoustic inversion in the presence of motion dynamics", *J. Acoust. Soc. Am.*, in press, 2014.

B. A. Tan, P. Gerstoft, C. Yardim, W. S. Hodgkiss, "Change-point detection for Recursive Bayesian geoacoustic inversion", to be submitted to *J. Acoust. Soc. Am.*.

Thesis

B. A. Tan, "Multichannel communication based on adaptive equalization in very shallow water acoustic channels", Master Thesis, National University of Singapore, 2007.

Conference proceedings

B. A. Tan, P. Gerstoft, C. Yardim, W. S. Hodgkiss, "Synthetic aperture geoacoustic inversion in the presence of radial velocity and acceleration dynamics", *OCEANS 2013 MTS/IEEE Conference Proceedings*, San Diego, California, pp. 1-6, 2013.

K. Zhong, S. S. Quek, T. A. Koh, B. A. Tan, "A real-time coded OFDM acoustic modem in very shallow underwater communications", *OCEANS 2006 Asia Pacific IEEE Conference Proceedings*, Singapore, pp. 1-5, 2007.

B. A. Tan, S. S. Quek, N. Zou, "Characterization of multipath acoustic channels in very shallow waters for communications", *OCEANS 2006 Asia Pacific IEEE Conference Proceedings*, Singapore, pp. 1-8, 2007.

B. A. Tan, M. Motani, M. Chitre, S. S. Quek, "Multichannel communication based on adaptive equalization in very shallow water acoustic channels", *Acoustics 2006 Australian Acoustical Society* , Christchurch, New Zealand, pp. 515-522, 2006.

B. A. Tan, M. Motani, T. J. Lim, "A note on polynomial complexity optimal multiuser detection for certain non-orthogonal CDMA signals", *ICCS 2002 IEEE Conference Proceedings*, Singapore, vol. 2, pp. 889-893, 2002.

Presentations, posters and abstracts

B. A. Tan, P. Gerstoft, C. Yardim, W. S. Hodgkiss, "Recursive Bayesian synthetic aperture geoacoustic inversion in the presence of motion dynamics", *2nd International Conference and Exhibition on Underwater Acoustics 2014*, Rhodes island, Greece, 2014.

B. A. Tan, P. Gerstoft, C. Yardim, W. S. Hodgkiss, "Synthetic aperture geoacoustic inversion in the presence of radial acceleration dynamics", *J. Acoust. Soc. Am.*, vol. 134, pp. 3990, 2013.

B. A. Tan, C. Yardim, P. Gerstoft, W. S. Hodgkiss, "Broadband synthetic aperture matched field geoacoustic inversion with a single hydrophone", *J. Acoust. Soc. Am.*, vol. 132, pp. 2093, 2012.

B. A. Tan, P. Gerstoft, C. Yardim, W. S. Hodgkiss, "Geoacoustic inversion in shallow water using broadband synthetic aperture and single hydrophone acoustic data", *J. Acoust. Soc. Am.*, vol. 130, pp. 2391, 2011.

ABSTRACT OF THE DISSERTATION

Broadband Synthetic Aperture Matched Field Geoacoustic Inversion

by

Bien Aik Tan

Doctor of Philosophy in Electrical Engineering
(Signal and Image Processing)

University of California, San Diego, 2014

Professor William S. Hodgkiss, Chair
Professor Peter Gerstoft, Co-Chair

A typical geoacoustic inversion procedure involves powerful source transmissions received on a large-aperture receiver array. A more practical approach is to use a moving single source/receiver, broadband, frequency-coherent matched-field inversion strategy that exploits coherently repeated transmissions to improve estimation of the geoacoustic parameters. The long observation time creates a synthetic aperture due to relative source-receiver motion. To correlate well with the measured field, waveguide Doppler and normal mode theory is applied. However, this method uses a waveguide Doppler model that constrains the source/receiver radial velocity to be constant. As a result, the inversion performance degrades

when source/receiver acceleration exists. Furthermore, processing a train of pulses all-at-once does not take advantage of the natural incremental acquisition of new pulses along with the ability to assess the temporal evolution of parameter uncertainty. Therefore, a recursive Bayesian estimation approach is developed that coherently processes the data pulse-by-pulse and incrementally updates estimates of parameter uncertainty. It also approximates source/receiver acceleration by assuming piecewise constant but linearly changing source/receiver velocities. When the source/receiver acceleration exists, it is shown that modeling acceleration can reduce further the parameter estimation biases and uncertainties. Finally, the above methods depended on the assumption of constant underlying geophysical model parameters. A change-point detection method is proposed to detect the change in the model parameters using the importance samples and corresponding weights that already are available from the recursive Bayesian inversion. If the model parameters change abruptly, a change-point will be detected and the inversion will restart with the pulse measurement after the change-point. If the model parameters change gradually, the inversion (based on constant model parameters) may proceed to estimate an averaged value of the parameters until the accumulated model parameter mismatch is significant and triggers the detection of a change-point. These form the heuristics for controlling the coherent integration time in recursive Bayesian inversion. Examples are based either on synthetically generated acoustic fields using the waveguide Doppler model or a set of low SNR, 100–900 Hz LFM pulse data from a moving source-receiver pair in the Shallow Water 2006 experiment.

Chapter 1

Introduction

Based on the signal measured at a receiver that is some distance away from the source, the general idea of geoacoustic inversion is to optimize the waveguide geoacoustic model parameters by minimizing the difference between the measured and the replica (modeled) acoustic fields (see Figs. 1.1 and 1.2). In doing this, seafloor properties are estimated without resorting to costly direct measurements such as coring. Knowing the seafloor acoustic properties is important for various applications such as sonar performance prediction and operation [1–3], source localization [4,5] and detection and classification of underwater man-made objects [6,7].

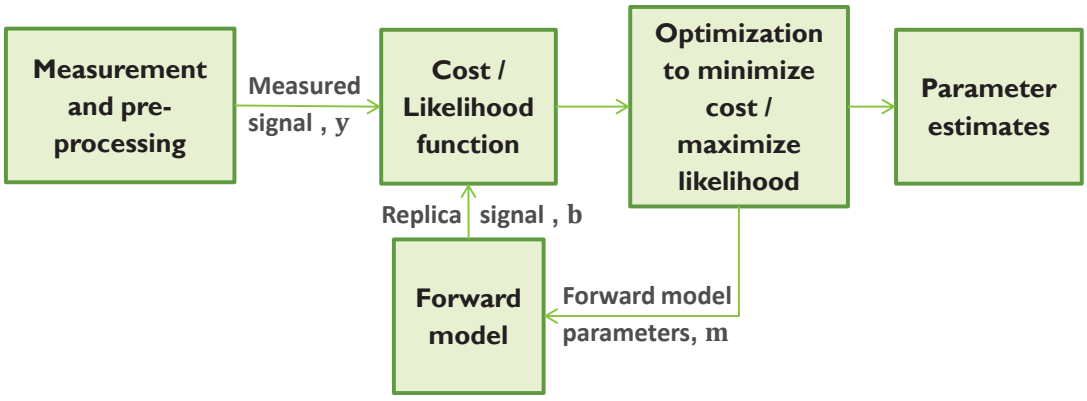

Figure 1.1: Generic inversion model

Typically, matched-field geaocoustic inversion experiments use large-aperture

arrays and powerful transmissions to achieve high signal to noise ratio (SNR). The large aperture arrays usually span a large fraction of the entire water column or cover a long distance horizontally (see Fig. 1.2). Deploying large aperture arrays is useful because they improve SNR and the spatial diversity of the measurements. However, their deployments can be time consuming and complex.

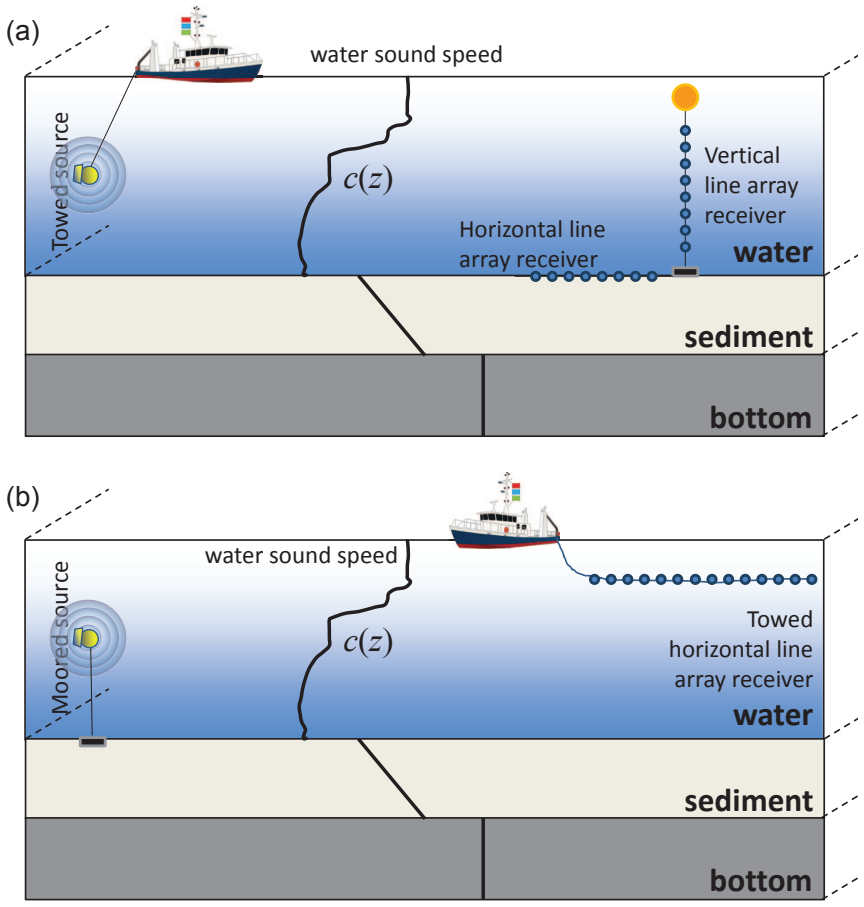

Figure 1.2: Typical matched field geoacoustic inversion in a (a) towed source and bottom moored horizontal and vertical line array receiver configurations and (b) a bottom moored source and a towed horizontal line array receiver configuration.

Alternatively, single-receiver/synthetic aperture inversion methods are preferable operationally due to ease of deployment [5,8–20]. Furthermore, low SNR methods are attractive due to their ability to use low powered sources, e.g. battery powered acoustic sources [21], resulting in less disturbance to marine mammals [11].

Having a combined mobile, low SNR and single source/receiver method makes it well suited for rapid environment assessment [21–25] using a horizontally moving source and/or receiver. The source or receiver may be towed horizontally by a ship or an autonomous underwater vehicle (AUV) (see Fig. 1.3). Alternatively, a battery powered acoustic source may be dropped onto the ocean bottom to aid AUV-based geoacoustic inversion [21]. AUV-based inversions recently have been gaining research interest due to its operational attractiveness [1,22–25]. Four main

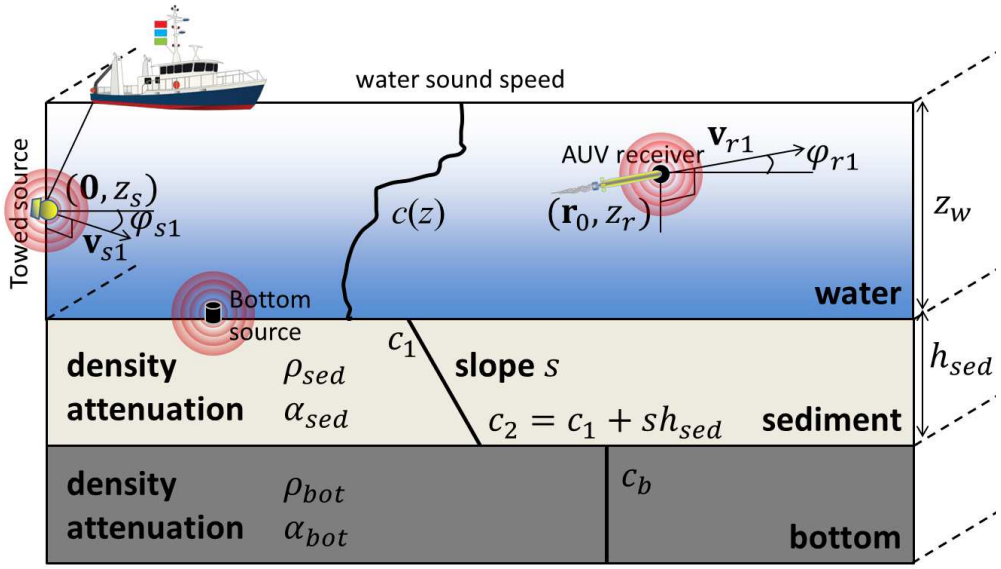

Figure 1.3: Horizontally stratified ocean with a horizontally moving source and receiver. The source is moving at initial velocity $\mathbf{v}_{s1}$ and bearing φ_{s1}, while the receiver is moving at initial velocity $\mathbf{v}_{r1}$ and bearing φ_{r1}. The range origin is the source position at time zero when the source begins transmitting.

types of single-receiver/synthetic aperture based geoacoustic inversion/source localization methods have been proposed: (1) dispersion curve analysis [8–11], (2) the matched impulse response method [5,12–16], (3) matched field processing [17,18], and (4) synthetic aperture modal inverse techniques [19,20].

Ship noise is a good source of opportunity for carrying out inversions. Using relative dispersion curves combined with waveguide invariant principles, ship noise data is utilized in the geoacoustic inversion in Ref. [11] using just one receiver with a few dB SNR. However, due to the method's incoherent process where intensity

(without phase) in a relative wavenumber space (without wavenumber reference) is used, any true multi-layered waveguide can only be represented by a simple Pekeris waveguide [11]. Other dispersion based inversions [8–10] are done using imploding glass bulbs or air guns (impulsive sources). These methods [8–10] work well only for low frequency sources ($f < 200$ Hz) and use long propagation distances ($r > 7$ km) to separate the dispersion between the modes.

Refs. [12–14] are related to matched impulse response geoacoustic inversions where Refs. [12,13] addressed source motion compensation for high bandwidth-time product LFMs receptions. To the best of the author's knowledge, other moving source or receiver inversion methods [11–13] mitigated Doppler effects in the received signal instead of modeling waveguide Doppler in the forward model, which may result in residual errors. Lastly, a single receiver synthetic aperture modal inverse technique will require the source or receiver to traverse distances up to a few kilometers to have sufficient wavenumber resolution to transform the measured transmission loss curve into the wavenumber spectrum for mode matching [19,20].

In contrasts, matched-field geoacoustic inversion do not have the limitations mentioned above. A high SNR matched-field inversion using a slow drifting compact four-receiver array is demonstrated in Ref. [17]. Ref. [18] showed in simulation that a static single source/receiver matched field inversion is sufficient for matched field inversion if a coherent processor in frequency is used. This dissertation takes a step further by focusing on matched field inversions methods for mobile, single source and receiver configurations in low SNR conditions.

The initial focus of this research is on a single-source/receiver, broadband, frequency coherent matched-field inversion procedure [26] where there is source and/or receiver motion. It comprises long-time coherent integration of multiple broadband transmissions, recasting dynamic time-varying geometric model parameters into initial-value and constant parameters via a trajectory-based waveguide Doppler normal mode model and assumes constant underlying geophysical model parameters. It exploits coherently repeated transmissions to improve estimation of the geoacoustic parameters in low SNR conditions. This reduces estimation uncertainty without resorting to a single powerful source transmission. The long

observation time improves the SNR and creates a synthetic aperture due to relative source-receiver horizontal motion.

Due to the repeated transmissions and longer observation time, the observed source spectrum becomes increasingly Doppler sensitive. Hence source/receiver motion has to be taken in account using waveguide Doppler theory where each horizontal wavenumber or mode undergoes a different Doppler shift [26–32]. The theory of waveguide Doppler and modal propagation used throughout this dissertation is based on Schmidt and Kuperman [29,30] and is reviewed in detail in Chapter 2. Similar waveguide Doppler modeling has been used in narrowband synthetic aperture modal inverse methods [19,20,33,34].

Modeling waveguide Doppler requires coupling the source spectrum to the Green's function of the medium. As a result, the source spectrum must be known. Assuming the source spectrum is known, the impact of exploiting coherently multiple transmissions and waveguide Doppler on single-receiver matched-field inversions is examined. Chapter 2 presents the formulation of this inversion problem, simulation results as well as results from the analysis of low SNR, 100–900 Hz LFM data from the Shallow Water 2006 experiment.

Though successful, the approach in Chapter 2 is limited to constant source and receiver radial velocities. This assumption is violated in the region near the closest point of approach (CPA) or when the radial velocities change (see Fig. 1.4). Chapter 3 improves the broadband synthetic aperture geoacoustic inversion approach for cases where the radial velocity of the source/receiver changes over the total observation time. This is done through pulse-by-pulse coherent processing which in turn allows different source/receiver velocities. Thus, it introduces a waveguide Doppler approximation to source and receiver acceleration.

Furthermore, processing a train of pulses all-at-once does not take advantage of the natural incremental acquisition of new data along with the ability to assess the temporal evolution of parameter uncertainty. Here, an equivalent pulse-by-pulse coherent processing approach using Bayesian updating is developed. This Bayesian approach reduces parameter uncertainty by recursively improving the posterior density as new data is made available. With the Bayesian formulation,

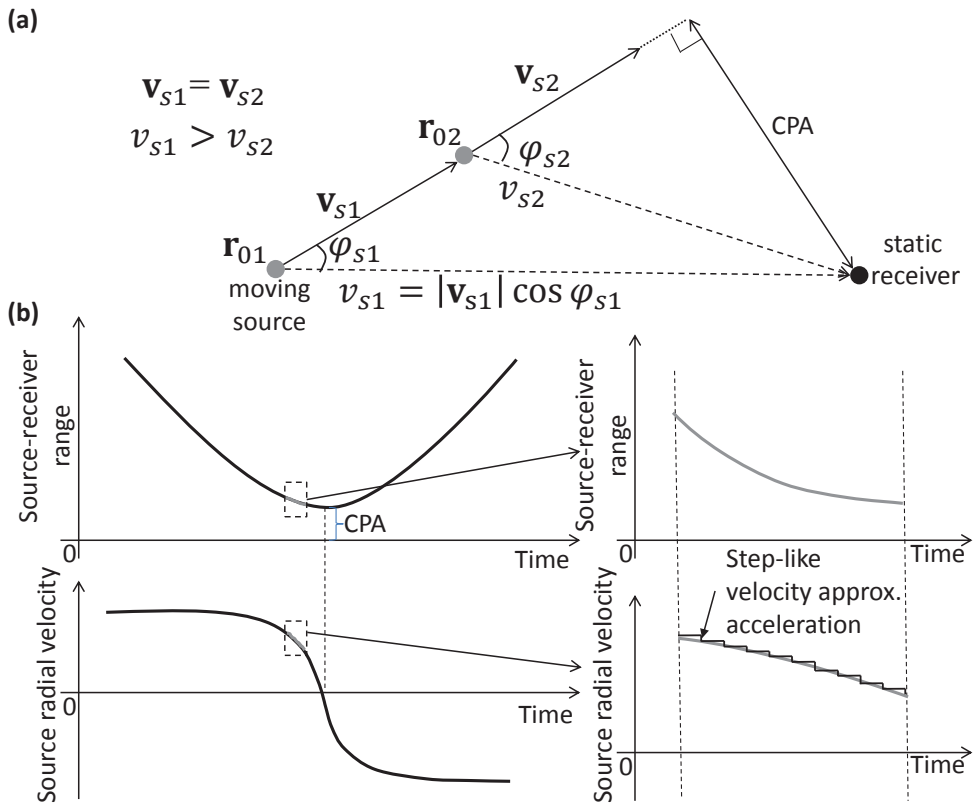

Figure 1.4: (a) Top view of a constant velocity source with changing radial velocity to the receiver due to the geometry of source/receiver positions. (b) Source–receiver range and radial velocity curves near CPA. Here, the change in source radial velocity in the dotted box approximately is linear with time corresponding to a constant acceleration.

the estimated posterior distribution provides quantitative uncertainty analysis [35]. It may also be used to infer uncertainties in another usage domain (e.g. transmission loss [3]). This recursive Bayesian approach allows new data to be added incrementally without having to wait for all data to be present before processing can take place [36]. At present, most single source and receiver methods [5,8–16,18,19,26], except [37], do not use the Bayesian approach for uncertainty analysis.

The formulation for the recursive Bayesian synthetic aperture geoacoustic inversion in the presence of motion dynamics is detailed in Chapter 3. Simulation results are presented as well as results from the analysis of low SNR, 100–900 Hz LFM data from the Shallow Water 2006 experiment.

A key assumption for the methods both in Chapter 2 and Chapter 3 is constant underlying model parameters. Because of the long-time coherent observation and source-receiver motion, change in the underlying model parameters due to time or space is anticipated. In Chapter 4, an inversion method is proposed for abrupt and gradual change in the underlying model parameters. A model parameter change-point detection method [38–43] is proposed to detect the change in the model parameters using the importance samples and corresponding weights that already are available from the recursive Bayesian inversion developed in Chapter 3. If a model parameter changes abruptly, a change-point will be detected and the inversion will restart with the pulse measurement after the change-point. If the model parameters change gradually, the inversion (based on constant model parameters) may proceed to estimate an average value of the parameters until the accumulated model parameter mismatch error is significant and triggers the detection of a change-point. These form the heuristics for controlling the coherent integration time in recursive Bayesian inversion detailed in Chapter 4.

Lastly, conclusions from this research and suggestions for future work are provided in Chapter 5.

Chapter 2

Broadband synthetic aperture geoacoustic inversion

2.1 Introduction

Typically, matched-field inversion experiments use large-aperture arrays and powerful transmissions with high SNR. However, single-receiver/synthetic aperture inversion methods are preferable operationally due to ease of deployment [5,8–20]. Furthermore, low SNR methods are attractive due to their ability to use low powered sources, e.g. battery powered acoustic sources [21], resulting in less disturbance to marine mammals [11]. This chapter focuses on matched field inversion for mobile, single source-receiver configurations in low SNR conditions.

Four main types of single-receiver/synthetic aperture based geoacoustic inversion/source localization methods have been proposed: (1) dispersion curve analysis [8–11], (2) the matched impulse response method [5,12–16], (3) matched field processing [17,18], and (4) synthetic aperture modal inverse techniques [19,20].

Ship noise is a good source of opportunity for carrying out inversions. Using relative dispersion curves combined with waveguide invariant principles, ship noise data is inverted for a simple Pekeris waveguide in Ref. [11] using just one receiver with a few dB SNR. Other dispersion based inversions [8–10] are done using imploding glass bulbs or air guns (impulsive sources). These methods work well

only for low frequency sources ($f < 200$ Hz) and use long propagation distances to separate the dispersion between the modes.

Here, a single-receiver, broadband, frequency-coherent matched-field inversion procedure is formulated to exploit coherently repeated transmissions to reduce estimation uncertainty without resorting to powerful source transmissions. Due to the repeated transmissions and longer observation time, the overall source spectrum becomes increasingly Doppler sensitive. In addition, the source-receiver relative motion also creates a longer synthetic aperture that is utilized in the inversion. To correlate well with the measured field, waveguide Doppler and normal mode theory is applied [27–32]. Similar waveguide Doppler modeling has been used in narrowband synthetic aperture modal inverse methods [19,20,33,34]. Other moving source or receiver inversion methods [11–13] mitigated Doppler effects in the received signal instead of the forward model, which may result in residual errors.

Modeling waveguide Doppler requires coupling the source spectrum to the Green's function of the medium. As a result, the source spectrum needs to be known. Assuming the source spectrum is known, the impact of exploiting coherently multiple transmissions and waveguide Doppler on single-receiver matched-field inversions is examined. The method is well suited for low SNR scenarios as well as rapid environment assessment using a horizontally moving source and receiver. The theory of waveguide Doppler and modal propagation is reviewed in Section 2.2, followed by the formulation of the inversion problem. Simulation results are presented in Section 2.3. Section 2.4 presents results from the analysis of experimental data.

2.2 Theory

2.2.1 Waveguide Doppler - normal mode representation

The Doppler effect, due to source and/or receiver motion, on a signal propagating in free space is described by a simple Galilean transformation [44]. However, in a waveguide, the Doppler effect is more complicated due to the multipath phenomenon, e.g. Refs. [27–32]. In this dissertation, the range-independent waveguide

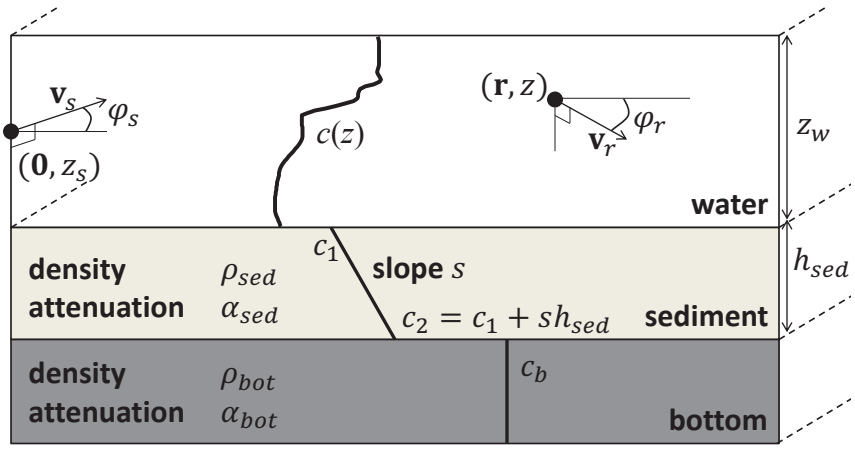

Figure 2.1: Horizontally stratified ocean with horizontally moving source and receiver. The source is moving at velocity $\mathbf{v}_s$ and bearing φ_s, while the receiver is moving at velocity $\mathbf{v}_r$ and bearing φ_r. Range origin is defined as the source position at time zero when the source begins transmitting.

Doppler theory is adopted to synthesize the field [29,30]. This implies that each horizontal wavenumber or mode will undergo a different Doppler shift. The scenario considered is depicted in Fig. 2.1.

Reasons for choosing the Schmidt and Kuperman [29,30] waveguide Doppler model are: (1) it has both spectral and modal solutions which can be adapted from several commonly used acoustic models, (2) it recognizes the non-reciprocity of source and receiver motion which means that the Doppler is a function of source and receiver motion and not of relative motion alone, and (3) the solution is in the frequency domain thus directly applicable to frequency coherent matched field processing. However, the model only allows horizontal motion which is adequate since most moving underwater sources and receivers are horizontally towed or propelled.

The theory begins off with the wave equation incorporating only the source motion which produces a range-time domain solution. Receiver motion is subsequently included but the solution exhibits a time-wavenumber coupling in the wavenumber integral and is ill-suited for numerical implementation. Fortunately, this time-wavenumber coupling can be removed by converting the solution into the range-frequency domain. With some approximations, a numerically tractable

solution using wavenumber integration (spectral method) is derived. Lastly, with additional approximations, a numerically and relatively more efficient solution using the normal mode theory is presented and is used throughout this dissertation.

Doppler effect by source motion

The theory begins with the Cartesian coordinate inhomogeneous wave equation, incorporating only the source motion. It represents a moving harmonic point source with constant horizontal velocity vector $\mathbf{v}_s$ and source frequency ω_s. $S(\omega_s)$ is the source spectrum representing the amplitude and phase of the harmonic point source.

$$\nabla^2\psi(\mathbf{r},z;t) - \frac{1}{c^2}\frac{\partial^2\psi(\mathbf{r},z;t)}{\partial t^2} = -\delta(\mathbf{r}-\mathbf{v}_s t)\delta(z-z_s)S(\omega_s)e^{-i\omega_s t} \tag{2.1}$$

Following the Fourier transform conventions and derivations in Schmidt and Kuperman [29,30],

$$f(t) = \frac{1}{2\pi}\int_{-\infty}^{\infty} f(\omega)e^{-i\omega t}\mathrm{d}\omega \tag{2.2}$$

$$f(\omega) = \int_{-\infty}^{\infty} f(t)e^{i\omega t}\mathrm{d}t \tag{2.3}$$

The Helmholtz equation is derived via the following

$$\begin{aligned}\nabla^2\frac{1}{2\pi}\int_{-\infty}^{\infty}\psi(\mathbf{r},z;\omega)e^{-i\omega t}\mathrm{d}\omega - \frac{1}{c^2}\frac{\partial^2}{\partial t^2}\frac{1}{2\pi}\int_{-\infty}^{\infty}\psi(\mathbf{r},z;\omega)e^{-i\omega t}\mathrm{d}\omega \\ = -\frac{1}{2\pi}\int_{-\infty}^{\infty}\int_{-\infty}^{\infty}\delta(\mathbf{r}-\mathbf{v}_s t)\delta(z-z_s)S(\omega_s)e^{-i\omega_s t}e^{i\omega t}\mathrm{d}t\, e^{-i\omega t}\mathrm{d}\omega\end{aligned} \tag{2.4}$$

$$\begin{aligned}\frac{1}{2\pi}\int_{-\infty}^{\infty}\left[\nabla^2\psi(\mathbf{r},z;\omega) - \frac{(i\omega)^2}{c^2}\psi(\mathbf{r},z;\omega)\right]e^{-i\omega t}\mathrm{d}\omega \\ = \frac{1}{2\pi}\int_{-\infty}^{\infty}\left[\int_{-\infty}^{\infty} -\delta(\mathbf{r}-\mathbf{v}_s t)\delta(z-z_s)S(\omega_s)e^{-i\omega_s t}e^{i\omega t}\mathrm{d}t\right]e^{-i\omega t}\mathrm{d}\omega\end{aligned} \tag{2.5}$$

$$[\nabla^2 + k_\omega^2]\psi(\mathbf{r},z;\omega) = -\delta(z-z_s)S(\omega_s)\int_{-\infty}^{\infty}\delta(\mathbf{r}-\mathbf{v}_s t)e^{i(\omega-\omega_s)t}\mathrm{d}t \tag{2.6}$$

where $k_\omega = \frac{\omega}{c}$ is the medium wavenumber at propagation frequency ω. Because of source motion, the problem is not axisymmetric. Therefore, a two-dimensional Fourier transform is used to reduce the spatial dimension of the Helmholtz equation.

$$\psi(\mathbf{r}, z; \omega) = \int \psi(\mathbf{k}, z; \omega) e^{i\mathbf{k}\cdot\mathbf{r}} \mathrm{d}^2\mathbf{k} \tag{2.7}$$

$$\psi(\mathbf{k}, z; \omega) = \frac{1}{(2\pi)^2} \int \psi(\mathbf{r}, z; \omega) e^{-i\mathbf{k}\cdot\mathbf{r}} \mathrm{d}^2\mathbf{r} \tag{2.8}$$

Using Eq.(2.7) and Eq.(2.8) on Eq.(2.6) in a similar method described in Eq.(2.4), Eq.(2.6) is transform into a depth-separated wave equation.

$$\begin{aligned}[\nabla^2 + k_\omega^2] \int \psi(\mathbf{k}, z; \omega) e^{i\mathbf{k}\cdot\mathbf{r}} \mathrm{d}^2\mathbf{k} = \int \frac{1}{(2\pi)^2} \int - \delta(z - z_s) S(\omega_s) \\ \times \int_{-\infty}^{\infty} \delta(\mathbf{r} - \mathbf{v}_s t) e^{i(\omega - \omega_s)t} \mathrm{d}t \, e^{-i\mathbf{k}\cdot\mathbf{r}} \mathrm{d}^2\mathbf{r} \, e^{i\mathbf{k}\cdot\mathbf{r}} \mathrm{d}^2\mathbf{k}\end{aligned} \tag{2.9}$$

$$\begin{aligned}\int \Big[\frac{\partial^2}{\partial z^2} + (k_\omega^2 - k^2)\Big] \psi(\mathbf{k}, z; \omega) e^{i\mathbf{k}\cdot\mathbf{r}} \mathrm{d}^2\mathbf{k} = \int -\frac{\delta(z - z_s)}{(2\pi)} \frac{1}{2\pi} \\ \times \int e^{i(\omega - \omega_s - \mathbf{k}\cdot\mathbf{v}_s)t} \mathrm{d}t \, S(\omega_s) e^{i\mathbf{k}\cdot\mathbf{r}} \mathrm{d}^2\mathbf{k}\end{aligned} \tag{2.10}$$

$$\Big[\frac{\partial^2}{\partial z^2} + (k_\omega^2 - k^2)\Big] \psi(\mathbf{k}, z; \omega) = -\frac{\delta(z - z_s)}{(2\pi)} \delta(\omega - \omega_s - \mathbf{k}\cdot\mathbf{v}_s) S(\omega_s) \tag{2.11}$$

with $k = |\mathbf{k}|$ is the horizontal wavenumber, and where the following identities,

$$\int \delta(\mathbf{r} - \mathbf{v}_s t) e^{-i\mathbf{k}\cdot\mathbf{r}} \mathrm{d}^2\mathbf{r} = e^{-i\mathbf{k}\cdot\mathbf{v}_s t} \tag{2.12}$$

and

$$\frac{1}{2\pi} \int e^{i(\omega - \omega_s - \mathbf{k}\cdot\mathbf{v}_s)t} \mathrm{d}t = \delta(\omega - \omega_s - \mathbf{k}\cdot\mathbf{v}_s), \tag{2.13}$$

are used.

Eq.(2.11) is a standard depth-separated wave equation of the form given in Section 2.4.1.1 of Jensen et. al. [30] with the solution,

$$\psi(\mathbf{k}, z; \omega) = S(\omega_s) \delta(\omega - \omega_s - \mathbf{k}\cdot\mathbf{v}_s) g(k, z; \omega) \tag{2.14}$$

where $g(k, z; \omega)$ is the depth-dependent Green's function for the waveguide at propagation frequency ω. From Eq.(2.14), the mode-dependent frequency shifts on the

source spectrum as the dirac delta function operates like an indicator function to turn on the Green's function only when $\omega = \omega_s + \mathbf{k} \cdot \mathbf{v}_s$.

The range-time domain solution can be obtain by using the Fourier transform defined in Eq.(2.7) to change the above solution into the range-frequency domain and then using inverse Fourier transform defined in Eq.(2.2).

$$\psi(\mathbf{r}, z; t) = \frac{1}{2\pi} \int_{-\infty}^{\infty} \Big[\int \psi(\mathbf{k}, z; \omega) e^{i\mathbf{k}\cdot\mathbf{r}} \mathrm{d}^2\mathbf{k} \Big] e^{-i\omega t} \mathrm{d}\omega \tag{2.15}$$

Substituting Eq.(2.14) into Eq.(2.15), the range-time domain solution for the field becomes

$$\psi(\mathbf{r}, z; t) = \frac{1}{2\pi} \int S(\omega_s) g(\mathbf{k}, z; \omega_s + \mathbf{k} \cdot \mathbf{v}_s) e^{-i[(\omega_s + \mathbf{k}\cdot\mathbf{v}_s)t - \mathbf{k}\cdot\mathbf{r}]} \mathrm{d}^2\mathbf{k} \tag{2.16}$$

So far the range-time domain field due to source horizontal motion $\mathbf{v}_s$ and a **single** source excitation frequency ω_s is described. To compute the field, the Green's function for each wavenumber vector $\mathbf{k}$ at **propagation** frequency is evaluated,

$$\omega = \omega_s + \mathbf{k} \cdot \mathbf{v}_s. \tag{2.17}$$

Also, for the source motion only case, the receiver frequency ω_r is equal to the propagation frequency ω. However, when the receiver moves horizontally in a waveguide, it will introduce another set of mode dependent frequency shifts on the propagation frequencies. Therefore, when there is receiver motion, the receiver frequency ω_r is **not** equal to the propagation frequency ω.

Broadband Doppler effect by source and receiver motion

In this section, receiver motion is included and the solution for a bandlimited source spectrum is presented. Redefining receiver position vector, $\mathbf{r}$, as a function of receiver velocity and time,

$$\mathbf{r} = \mathbf{r_0} + \mathbf{v}_r t \tag{2.18}$$

where $\mathbf{r_0}$ is the receiver position at $t = 0$ and $\mathbf{v}_r$ is the receiver velocity vector. Substituting Eq.(2.18) into Eq.(2.16) modifies the range-time domain solution for the field to

$$\psi(\mathbf{r_0} + \mathbf{v}_r t, z; t) = \frac{1}{2\pi} \int S(\omega_s) g(\mathbf{k}, z; \omega_s + \mathbf{k} \cdot \mathbf{v}_s) e^{-i\{[\omega_s + \mathbf{k}\cdot(\mathbf{v}_s - \mathbf{v}_r)]t - \mathbf{k}\cdot\mathbf{r_0}\}} \mathrm{d}^2\mathbf{k} \tag{2.19}$$

From Eq.(2.19), following points are noted:

- source and receiver motions' asymmetrical effect on integration kernel (Green's function). Only source velocity matters if the argument is based on source frequencies.
- source and receiver motions symmetrical frequency shifting effect on the exponential.
- Hence, if $\mathbf{v}_s = \mathbf{v}_r$, there is no frequency shift. But the Green's function is still affected by the source velocity. This non-reciprocity in velocity is seldom appreciated. On the other hand, this effect is negligible as shown in Schmidt and Kuperman [29,30].

As mentioned earlier, the time-wavenumber coupling makes it necessary to evaluate the integral for each time and wavenumber instances. This is numerically intractable. Schmidt and Kuperman circumvented this problem by making the following modifications which is to include a bandlimited source spectrum and an integration over time and space to express the field in the frequency domain. The field is now summed for a bandlimited frequency source excitation in Eq.(2.20).

$$\psi(\mathbf{r_0} + \mathbf{v}_r t, z, t) = \frac{1}{(2\pi)^2} \int\int S(\omega_s) g(\mathbf{k}, z; \omega_s + \mathbf{k} \cdot \mathbf{v}_s) \times e^{-i\{[\omega_s + \mathbf{k}\cdot(\mathbf{v}_s - \mathbf{v}_r)]t - \mathbf{k}\cdot\mathbf{r_0}\}} \mathrm{d}^2\mathbf{k}\, \mathrm{d}\omega_s \quad (2.20)$$

Applying the Fourier transform as defined in Eq.(2.3) to Eq.(2.20).

$$\begin{aligned}
\psi(\mathbf{r}, z, \omega_r) &= \int \psi(\mathbf{r_0} + \mathbf{v}_r t, z, t) e^{i\omega_r t} \mathrm{d}t \\
&= \frac{1}{(2\pi)^2} \int\int S(\omega_s) g(\mathbf{k}, z; \omega_s + \mathbf{k}\cdot\mathbf{v}_s) \\
&\qquad\qquad \int e^{-i\{[\omega_s - \omega_r + \mathbf{k}\cdot(\mathbf{v}_s - \mathbf{v}_r)]t\}} \mathrm{d}t \, \mathrm{d}\omega_s \, e^{i\mathbf{k}\cdot\mathbf{r_0}} \mathrm{d}^2\mathbf{k} \\
&= \frac{1}{(2\pi)} \int\int S(\omega_s) g(\mathbf{k}, z; \omega_s + \mathbf{k}\cdot\mathbf{v}_s) \\
&\qquad\qquad \delta[\omega_s - \omega_r + \mathbf{k}\cdot(\mathbf{v}_s - \mathbf{v}_r)] \mathrm{d}\omega_s \, e^{i\mathbf{k}\cdot\mathbf{r_0}} \mathrm{d}^2\mathbf{k} \\
&= \frac{1}{(2\pi)} \int S[\omega_r - \mathbf{k}\cdot(\mathbf{v}_s - \mathbf{v}_r)] g(\mathbf{k}, z; \omega_r + \mathbf{k}\cdot\mathbf{v}_r) e^{i\mathbf{k}\cdot\mathbf{r_0}} \mathrm{d}^2\mathbf{k} \\
&= \frac{1}{(2\pi)} \int S[\omega_s^{(\mathbf{k})}] g(\mathbf{k}, z; \omega_r + \mathbf{k}\cdot\mathbf{v}_r) e^{i\mathbf{k}\cdot\mathbf{r_0}} \mathrm{d}^2\mathbf{k}
\end{aligned} \tag{2.21}$$

where $\mathbf{r}$ represents a straight line, Eq.(2.18), describes the receiver trajectory because the frequency domain solution integrates over time. ω_r is the receiver frequency and $\omega_s^{(\mathbf{k})}$ is the mode dependent Doppler-shifted source frequency.

$$\omega_s^{(\mathbf{k})} = \omega_r - \mathbf{k}\cdot(\mathbf{v}_s - \mathbf{v}_r) \tag{2.22}$$

Comparing Eq.(2.21) to the static case, there are two differences. Firstly, in the moving case, the source spectrum frequency is wavenumber and velocity dependent. This result in coupling the source spectrum and the Green's function together in the integrand. On the contrary, in the static case, the source spectrum frequency is wavenumber independent and is applied outside the integral. Secondly, in the moving case, the Green's function propagation frequency is wavenumber and velocity dependent. Separately, it can also be noted that the **propagation** frequency is also,

$$\omega = \omega_r + \mathbf{k}\cdot\mathbf{v}_r \tag{2.23}$$

For clarity, $\mathbf{k}$ is always evaluated at propagation frequency ω in the Green's function. Up to this point, Eq. (2.21) is exact within the theory of linear acoustics. Linear acoustics presumes that the turbulence caused by the ambient flow across the source or receiver is negligible [44]. Therefore, it is implicit that source or

receiver velocities v,

$$A1 : v/c \ll 1. \tag{2.24}$$

Another assumption is

$$A2 : \mathbf{v}_r \text{ and } \mathbf{v}_s \text{ are constants and horizontal,} \tag{2.25}$$

which result in the simplified field described in Eq. (2.21).

Wavenumber Integration Representation

Eq.(2.21) is computationally intensive due to the 2-D wavenumber integral. The wavenumber integration is reduced to a single dimension by making a third assumption. That is, the source – receiver separation R is large compared to the distance moved $\delta R_{\delta t}$ by the source or receiver during the signal transmission or reception δt respectively.

$$A3 : \delta R_{\delta t} \ll R,\ R = |\mathbf{r}| \quad \Rightarrow \quad \delta\varphi_r \approx 0, \delta\varphi_s \approx 0 \tag{2.26}$$

This means that the radial velocities approximately are constant.

$$v_r = |\mathbf{v}_r| \cos\varphi_r, \quad v_s = |\mathbf{v}_s| \cos\varphi_s \tag{2.27}$$

As a result, the 2-D Fourier integral can be replaced by the Hankel transform on the horizontal wavenumber.

$$\begin{aligned} \psi(L, z, \omega_r) &\approx \int_0^\infty S[\omega_s^{(k)}] G(k, z; \omega_r + k v_r) J_0(k\, r_0) k \,\mathrm{d}k \\ &= \frac{1}{2} \int_{-\infty}^\infty S[\omega_s^{(k)}] G(k, z; \omega_r + k v_r) H_0^{(1)}(k\, r_0) k \,\mathrm{d}k \end{aligned} \tag{2.28}$$

where

$$\omega_s^{(k)} = \omega_r - k(v_s - v_r) \tag{2.29}$$

and

$$H_0^{(1)}(k r_0) = \sqrt{\frac{2}{\pi k r_0}} e^{i(k r_0 - \frac{\pi}{4})} \tag{2.30}$$

Eq.(2.28) can be numerically computed by existing wavenumber integration code such as OASES [45] to compute the Doppler shifted field. From Eq.(2.28), to compute the field at **receiver** frequency ω_r, the depth dependent Green's function have to be evaluated for every wavenumber k at the **propagation** frequency $\omega = \omega_r + k v_r$, and multiplied by the source spectrum at the **source** frequency $\omega_s^{(k)}$.

Normal Mode Representation

The wavenumber spectral representation given in Eq.(2.28) can now be converted into a normal mode representation which is computationally less intensive. This is done by using the normal mode approximation (as a result of ignoring branch line contribution) of the depth dependent Green's function mentioned in Sect 5.3 of Jensen et. al [30] and is shown below.

$$G(k,z;\omega) \approx \frac{1}{2\pi\rho(z_s)} \sum_n \frac{\Psi_n(z)\Psi_n(z_s)}{k^2 - k_n^2} \tag{2.31}$$

where k_n and Ψ_n are the modal wavenumbers and modal functions of the homogeneous form of Eq.(2.11) evaluated at propagation frequencies ω. Substituting Eq. (2.31) into Eq. (2.28), the Doppler shifted field via normal mode representation is approximated in the following:

$$\begin{aligned}
&\psi(L,z,\omega_r) \\
&\approx \frac{1}{2}\int_{-\infty}^{\infty} S[\omega_s^{(k)}] G(k,z;\omega_r + kv_r) H_0^{(1)}(kr_0) k\, dk \qquad (2.32)\\
&\approx \frac{1}{4\pi\rho(z_s)}\int_{-\infty}^{\infty} S[\omega_s^{(k)}] \sum_n \frac{\Psi_n(z;\omega_r + k_n v_r)\Psi_n(z_s;\omega_r + k_n v_r)}{(k-k_n)(k+k_n)} H_0^{(1)}(k_n r_0) k\, \mathrm{d}k \qquad (2.33)
\end{aligned}$$

Applying Cauchy integral, residue theorem and omitting the solution for negative horizontal wavenumbers

$$\begin{aligned}
&\psi(L,z,\omega_r) \\
&\approx \frac{2\pi i}{4\pi\rho(z_s)} \sum_n S\big[\omega_r - k_n(v_s - v_r)\big] \frac{\Psi_n(z;\omega_r + k_n v_r)\Psi_n(z_s;\omega_r + k_n v_r)}{2k_n} H_0^{(1)}(k_n r_0) k_n \qquad (2.34)\\
&\approx \frac{i}{4\rho(z_s)} \sum_n S[\omega_s^{(k_n)}] \Psi_n(z;\omega_r + k_n v_r)\Psi_n(z_s;\omega_r + k_n v_r) H_0^{(1)}(k_n r_0) \qquad (2.35)
\end{aligned}$$

where

$$\omega_s^{(k_n)} = \omega_r - k_n(v_s - v_r). \tag{2.36}$$

Table 2.1 summarizes the relationship of source, propagation and receiver frequencies where the first row is with respect to receiver frequency ω_r and the second

Table 2.1: Source, propagation and receiver frequencies mapping relationships.

Source	Propagation	Receiver
$\omega_s^{(k_n)} = \omega_r - k_n(v_s - v_r)$	$\omega = \omega_r + k_n v_r$	ω_r
ω_s	$\omega = \omega_s + k_n v_s$	$\omega_r^{(k_n)} = \omega_s + k_n(v_s - v_r)$

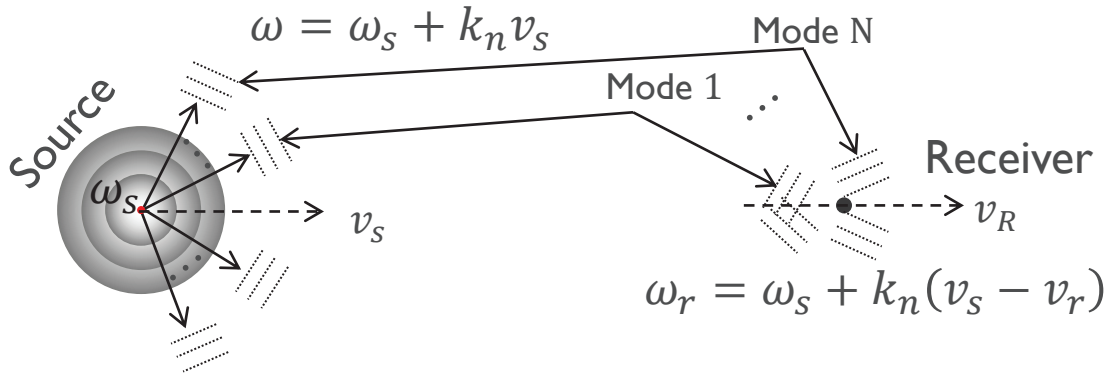

Figure 2.2: A single source frequency ω_s maps to several mode-dependent propagation frequencies ω due to source motion and undergoes further different shifts into receiver frequencies ω_r due to receiver motion.

is with respect to source frequency ω_s. The latter source-to-receiver frequency mapping relationships is depicted in Fig. 2.2.

For numerical efficiency, constructing the field in Eq. (2.35) is facilitated by some approximations to the propagation modal wavenumbers and functions that are computed instead from ω_r. It is assumed that the changes in the modal functions are negligible over the Doppler frequency shifts. In addition, modal cutoffs or additions introduced by Doppler frequency shifts are ignored.

$$A4 : \Psi(z;\omega) \approx \Psi(z;\omega_r) \approx \Psi(z;\omega_s). \tag{2.37}$$

$$A5 : \text{Modal cutoffs/additions are neglected.} \tag{2.38}$$

Hence, the modal functions evaluated at ω can be approximated from modal functions at ω_r or ω_s. Propagation modal wavenumber k_n then is approximated using Taylor's approximation. For the higher order terms to be negligible, the wavenumber change due to the shift in propagation frequency is assumed locally

linear [29,30]. This means that the frequency shift with respect to source or receiver frequency is small assuming Eq. (2.24). Let k_n be a function of angular frequency ω, which is $k_n = k_n(\omega)$.

$$\begin{aligned} A6 : k_n = k_n(\omega_r + k_n v_r) &\approx k_n(\omega_r) + \frac{\mathrm{d}k_n(\omega_r)}{\mathrm{d}\omega_r} k_n v_r \\ &\approx \frac{k_{rn}}{(1 - \frac{v_r}{u_{rn}})} \end{aligned} \tag{2.39}$$

where $u_{rn} = \frac{\mathrm{d}\omega_r}{\mathrm{d}k_n(\omega_r)}$ is the nth modal group velocity and $k_{rn} = k_n(\omega_r)$ is the nth modal wavenumber, both evaluated at ω_r . This approximation works backward from the receiver frequency. A forward k_n approximation based on ω_s also can be done using the same method in Eq. (2.39).

$$A7 : k_n = k_n(\omega_s + k_n v_s) \approx \frac{k_{sn}}{(1 - \frac{v_s}{u_{sn}})} \tag{2.40}$$

where $u_{sn} = \frac{\mathrm{d}\omega_s}{\mathrm{d}k_n(\omega_s)}$ is the nth modal group velocity and $k_{sn} = k_n(\omega_s)$ is the nth modal wavenumber, both evaluated at ω_s.

Substituting Eqs. (2.37) and (2.39) into Eq. (2.35), the Doppler shifted field via normal mode representation is obtained:

$$\psi(\mathbf{r}, z, \omega_r) \approx \frac{ie^{-i\frac{\pi}{4}}}{\sqrt{8\pi}\rho(z_s)} \sum_n S[\omega_s^{(k_n)}] \Psi_n(z; \omega_r) \Psi_n(z_s; \omega_r) \frac{e^{ik_n r_0}}{\sqrt{k_n r_0}} \tag{2.41}$$

In the case where the wavenumber k_{rn} is perturbed to manifest mode-dependent absorption losses, the resulting complex propagation wavenumber k_n can still be approximated using Eq. (2.39). The steps for generating the Doppler shifted field using normal modes are summarized as follows:

For any arbitrary receiver frequency ω_r,

- Compute the normal modes as per the static case evaluated at ω_r giving $\{\Psi_n(z_s; \omega_r), \Psi_n(z; \omega_r), k_{rn}, u_{rn}\}$
- With u_{rn} and v_r known, compute the propagation horizontal wave number k_n using Eq. (2.39)
- Extract the source spectrum $S[\omega_r - k_n(v_s - v_r)]$ and compute $\psi(\mathbf{r}, z, \omega_r)$ as defined in Eq. (2.41)

For a static field computation, $\omega_r = \omega_s$. On the other hand, with relative motion, a waveguide Doppler field computation at ω_r traces back to multiple source frequencies, see Eqs. (2.36) and (2.41). This backward mode-dependent frequency mapping is the main difference when compared to the static field computation.

Normal mode interpretation of waveguide Doppler

One way of viewing the frequency and wavenumber shifts of each mode is to evaluate the modal contributions of a harmonic point source. The ocean model used is illustrated in Fig. 2.1. The model parameters are tabulated in Table 2.2. KRAKEN [46] is used to compute the modes and wavenumbers. The contributions to the received field for each mode in frequency-wavenumber space are plotted in Fig. 2.3 as color-coded dots representing magnitudes normalized by the strongest mode. Fig. 2.3 is obtained by using Eqs. (2.41) and (2.40), and the second row of Table 2.1 to express the field by forward mapping the harmonic source frequency to multiple receiver frequencies. Fig. 2.3(a) shows a source moving away from the static receiver and Fig. 2.3(b) is the receiver moving away from a static source. Both plots include the static example as reference. The choice of speed is exaggerated to illustrate the Doppler effect. The 10 m/s receiver motion only case shifts the receiver frequencies. However, the –10 m/s moving source shifts both the receiver frequencies as well propagation horizontal wavenumbers. This illustrate the non-reciprocity of source/receiver motion, that waveguide Doppler is not a function of relative motion. This non-reciprocity in velocity is seldom appreciated. On the other hand, this effect is negligible as shown in Schmidt and Kuperman [29,30].

2.2.2 Likelihood and cost functions

The problem of matched field inversion to infer parameters characterizing the ocean environment is nonlinear due to the nonlinear relationship between the acoustic field and the parameters. Section 2.2.2 describes the maximum likelihood (ML) formulations for the frequency-coherent likelihood and cost functions of a single receiver in additive colored noise.

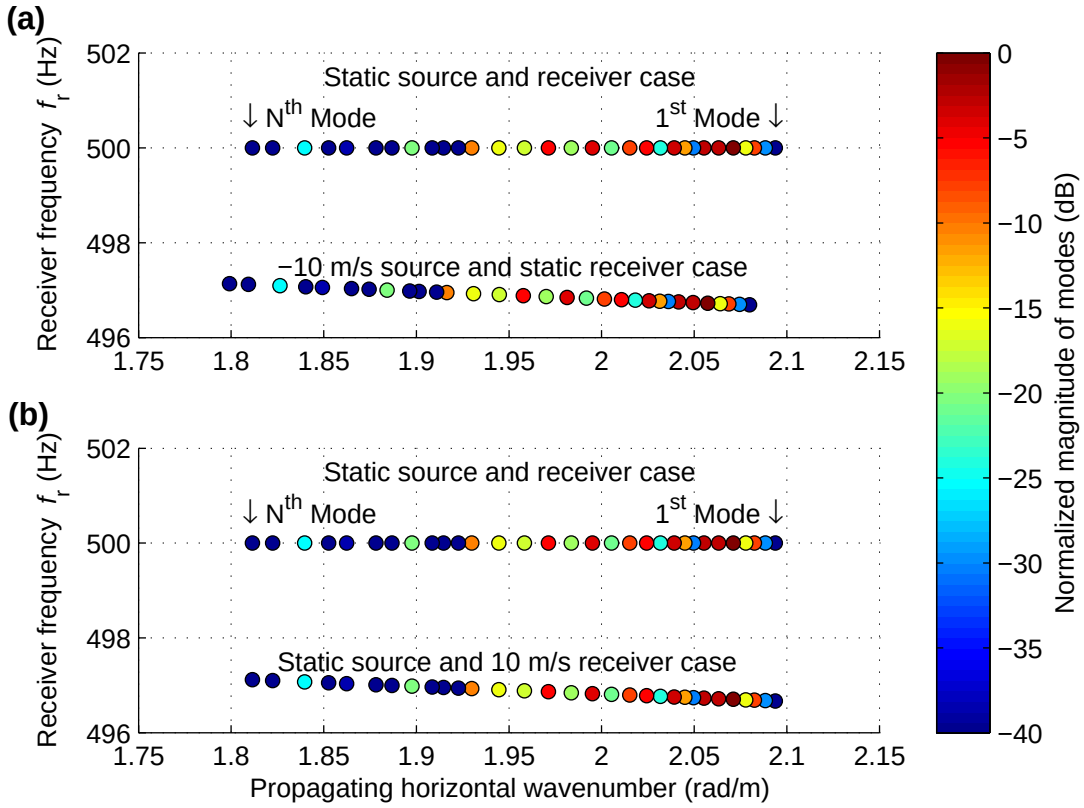

Figure 2.3: Frequency and modal dispersion from the waveguide Doppler effect for a $f_s = 500$ Hz harmonic source using the KRAKEN model. (a) Static case overlaid with moving source case (b) Static case overlaid with moving receiver case.

Frequency-coherent likelihood and cost functions of a moving source and receiver

A broadband data model for frequency-coherent match-field based geoacoustic inversion has been proposed [2,47,48]. Here, this model is improved by including source/receiver motion and realistic noise assumptions,

$$\mathbf{y} = \alpha\mathbf{E}(\xi)\mathbf{d}(\mathbf{m}) + \mathbf{w} = \alpha\mathbf{b}(\xi, \mathbf{m}) + \mathbf{w}, \tag{2.42}$$

where $\mathbf{y} = [y(\omega_{r1}) \dots y(\omega_{rJ})]^{\mathrm{T}}$ is the Fourier transform of the observed time series synchronized to the pulse transmission for J discrete frequencies. α is the complex scalar factor for unknown amplitude scaling and a frequency independent phase shift. $\mathbf{E}(\xi) = \mathrm{diag}[e^{i\omega_{r1}\xi} \dots e^{i\omega_{rJ}\xi}]$ where ξ is the timing error between the source and receiver clocks. The corresponding replica field $\mathbf{d}(\mathbf{m}) = [\psi(\omega_{r1}, \mathbf{m}) \dots \psi(\omega_{rJ}, \mathbf{m})]^{\mathrm{T}}$ is generated using Eq. (2.41) with vector $\mathbf{m}$. $\mathbf{m}$ is a subset of forward model parameters that are being optimized (see Fig. 2.1).

The distribution of the error vector $\mathbf{w} = [w(\omega_{r1}) \dots w(\omega_{rJ})]^{\mathrm{T}}$ defines the likelihood function. Error comprises ambient noise and modeling errors. In high SNRs, array-coherent frequency-incoherent techniques often neglect ambient noise but recognize modeling errors as dominant [49,50].

For low SNR frequency-coherent processing, the colored ambient noise might be a significant source of error. The frequency-dependent noise is modeled as a wide sense stationary (WSS) noise $u[n]$ with power spectral density $\gamma_u P_{uu}(\omega_r)$ where γ_u is a scaling factor, used for varying SNR in simulations and scaling the noise spectrum in inversions using real data. $P_{uu}(\omega_r)$ is estimated from the noise only data prior to signal transmission.

Taking a N-point discrete Fourier transform (DFT) of $u[n]$, let $\mathbf{w}$ be the DFT of $\mathbf{u}$ evaluated at frequencies $[\ \omega_{r1} \dots \omega_{rJ}\ ]$ with $J \leqslant N$. We will define the frequency domain noise $\mathbf{w}$ as complex Gaussian with mean $\mathrm{E}[\mathbf{w}] = \mathbf{0}$ for $\omega_r \neq 0$ and autocovariance [51]

$$\mathbf{C}_{\mathbf{w}} = \mathrm{E}[\mathbf{w}\mathbf{w}^{\mathrm{H}}] = N\gamma_u \mathrm{diag}[P_{uu}(\omega_{r1}) \ \dots \ P_{uu}(\omega_{rJ})]. \tag{2.43}$$

Thus, it is assumed that the error vector $\mathbf{w} \sim \mathcal{CN}(\mathbf{0}, \mathbf{C}_{\mathbf{w}})$. Factoring $\mathbf{C}_{\mathbf{w}} = \gamma\tilde{\mathbf{C}}_{\mathbf{w}}$

with reparameterized $\gamma = N\gamma_u$, the likelihood function can be expressed as [52]

$$L(\xi, \mathbf{m}, \alpha, \gamma) = \frac{1}{(\pi\gamma)^J |\tilde{\mathbf{C}}_\mathbf{w}|} \times$$
$$\exp\big\{ -[\mathbf{y} - \alpha\mathbf{b}(\xi, \mathbf{m})]^{\mathrm{H}} \tilde{\mathbf{C}}_\mathbf{w}^{-1} [\mathbf{y} - \alpha\mathbf{b}(\xi, \mathbf{m})] \;/\; \gamma \big\}. \tag{2.44}$$

The unknown complex scaling factor α and noise parameter γ are estimated by maximum likelihood estimation (MLE). Computing the MLE of α, $\hat{\alpha}$ and γ, $\hat{\gamma}$ via $\frac{\partial \ln L(\xi,\mathbf{m},\alpha,\gamma)}{\partial \alpha} = 0$ and $\frac{\partial \ln L(\xi,\mathbf{m},\alpha,\gamma)}{\partial \gamma} = 0$ respectively, gives

$$\hat{\alpha} = \frac{\mathbf{b}^{\mathrm{H}} \tilde{\mathbf{C}}_\mathbf{w}^{-1} \mathbf{y}}{\mathbf{b}^{\mathrm{H}} \tilde{\mathbf{C}}_\mathbf{w}^{-1} \mathbf{b}} \tag{2.45}$$

$$\hat{\gamma} = \frac{(\mathbf{y} - \alpha\mathbf{b})^{\mathrm{H}} \tilde{\mathbf{C}}_\mathbf{w}^{-1} (\mathbf{y} - \alpha\mathbf{b})}{J} = \frac{\beta(\xi, \mathbf{m})}{J}, \tag{2.46}$$

where $\beta(\xi, \mathbf{m})$ is the covariance-weighted Bartlett function [49], obtained by substituting $\alpha = \hat{\alpha}$, defined as

$$\beta(\xi, \mathbf{m}) = \mathbf{y}^{\mathrm{H}} \tilde{\mathbf{C}}_\mathbf{w}^{-1} \mathbf{y} - \frac{|\mathbf{y}^{\mathrm{H}} \tilde{\mathbf{C}}_\mathbf{w}^{-1} \mathbf{b}|^2}{\mathbf{b}^{\mathrm{H}} \tilde{\mathbf{C}}_\mathbf{w}^{-1} \mathbf{b}}. \tag{2.47}$$

Substituting Eqs. (2.45–2.47) into Eq. (2.44), the optimized inversion parameters obtained via the maximization of the log-likelihood function are

$$\begin{aligned} \big\{\xi, \mathbf{m}\big\}_{ML} &= \arg\max_{\xi,\mathbf{m}} \Big[\ln L(\xi, \mathbf{m}) \Big] \\ &= \arg\min_{\xi,\mathbf{m}} \Big[J \ln \beta(\xi, \mathbf{m}) + J(\ln \pi - \ln J + 1) + \ln |\tilde{\mathbf{C}}_\mathbf{w}| \Big] \\ &= \arg\min_{\xi,\mathbf{m}} \Big[10 \;\; \log_{10} \Phi(\xi, \mathbf{m}) \Big], \end{aligned} \tag{2.48}$$

where the cost function

$$\Phi(\xi, \mathbf{m}) = \frac{\beta(\xi, \mathbf{m})}{\mathbf{y}^{\mathrm{H}} \tilde{\mathbf{C}}_\mathbf{w}^{-1} \mathbf{y}} = 1 - \frac{|\mathbf{y}^{\mathrm{H}} \tilde{\mathbf{C}}_\mathbf{w}^{-1} \mathbf{b}|^2}{\mathbf{y}^{\mathrm{H}} \tilde{\mathbf{C}}_\mathbf{w}^{-1} \mathbf{y} \mathbf{b}^{\mathrm{H}} \tilde{\mathbf{C}}_\mathbf{w}^{-1} \mathbf{b}} \tag{2.49}$$

is the normalized covariance-weighted Bartlett function. In $\mathbf{y}^{\mathrm{H}} \tilde{\mathbf{C}}_\mathbf{w}^{-1} \mathbf{b}$, the correlation between the measured and the replica spectrum is inversely weighted by the noise spectrum.

2.2.3 Synthetic Aperture Formation

Extending the temporal duration of the source to a train of P repeated transmissions, the source spectrum is

$$S(f) = \sum_{p=0}^{P-1} \exp(i2\pi f p T_r) S_c(f), \tag{2.50}$$

where T_r is the pulse repetition interval (PRI) and $S_c(f)$ is the spectrum of the common or repeated source transmission. Substituting Eq. (2.50) into Eq. (2.41) also extends the moving source or receiver trajectory field. In essence, a synthetic aperture is formed since the waveguide Doppler field is computed by integrating over the source and receiver horizontal trajectory referenced to the source-receiver separation at $t = 0$. The source-receiver synthetic aperture length or relative displacement is $PT_r(v_s - v_r)$ m.

The extended duration transmission and relative motion means that the synthetic aperture length is longer than the one with a single LFM pulse. As explained later in Sect. 2.3.3, without the waveguide Doppler model, the mismatch between the measured (waveguide Doppler) and the replica (uniform Doppler [2,13]) complex field will increase with P and synthetic aperture length. This mismatch error then will map into the parameter estimation error.

2.2.4 Source Spectrum

A common broadband source used in geoacoustic inversion is the LFM pulse. It is the source used for the simulations in Sect. 2.3 and experimental data analysis in Sect. 2.4. Comparing Eq. (2.42) with other models [2,47,48] and examining Eq. (2.41), the source spectrum is coupled within, and non-commutable with, the integral of the Green's function due to source/receiver motion. This coupling results in very fine frequency indexing to the source spectrum for each mode. Hence, an analytic Fourier expression of the source spectrum is desirable. The time domain expression of the LFM pulse is

$$s_c(t) = \sin\left[\frac{\pi(f_2 - f_1)t^2}{T} + 2\pi f_1 t\right], \tag{2.51}$$

where f_1 and f_2 is the start and stop frequency respectively and T is the pulse width. Using the same Fourier transform convention [29,30], the frequency domain expression of the LFM pulse is

$$\begin{aligned} S_c(f) &= \int_0^T \sin\left[\frac{\pi(f_2-f_1)t^2}{T} + 2\pi f_1 t\right] e^{i2\pi f t} dt \\ &= \frac{B}{4\sqrt{\pi}}\, e^{-B^2(f_1+f)^2} \Bigg(e^{2B^2(f_1^2+f^2)} \{\mathrm{erf}[B(f_2-f)] - \mathrm{erf}[B(f_1-f)]\} \\ &\quad + i\mathrm{erf}[iB(f_2+f)] - i\mathrm{erf}[iB(f_1+f)] \Bigg), \end{aligned} \tag{2.52}$$

where $\mathrm{erf}(z) = (2/\pi)\int_0^z e^{-t^2} dt$ is the error function and $B = (\sqrt[4]{-1}\sqrt{\pi T})/\sqrt{f_2 - f_1}$.

Fig. 2.4 shows a section of the source spectrum for various P LFM pulses using Eqs. (2.50) and (2.52). Magnitudes have been normalized by the single LFM spectrum magnitude for comparison. The overall source spectrum $S(f)$ will result in periodic spectral peaks occurring every $1/T_r$ for $P \geqslant 2$. The null-to-null bandwidth for each peak is $2/(PT_r)$. In addition, the spectral peaks increase 6 dB for every doubling of P. Correspondingly, the noise spectrum level only increases by 3 dB, Eq. (2.43). These spectral peaks are good frequency sampling points although, as shown later in Sect. 2.3.3, source/receiver motion will require more frequency sampling points around these peaks. The overall source spectrum of multiple LFM pulses also approaches a multi-tone comb resulting in an inversion technique that is sensitive to waveguide Doppler, see Sect. 2.3.3.

2.3 Simulations

Based on the theory, this section will demonstrate three main points. First, Sect. 2.3.1 provides the inversion sensitivities for a simple static source/receiver setup using a single LFM pulse transmission. Then, in Sect. 2.3.2, Monte Carlo inversions at a fixed SNR for a static source/receiver show that estimation uncertainty is reduced by coherently exploiting multiple LFM pulse transmissions. Finally, in Sect. 2.3.3, for a moving source and static receiver case, both waveguide Doppler and a denser frequency sampling scheme are needed to preserve the uncertainty reduction.

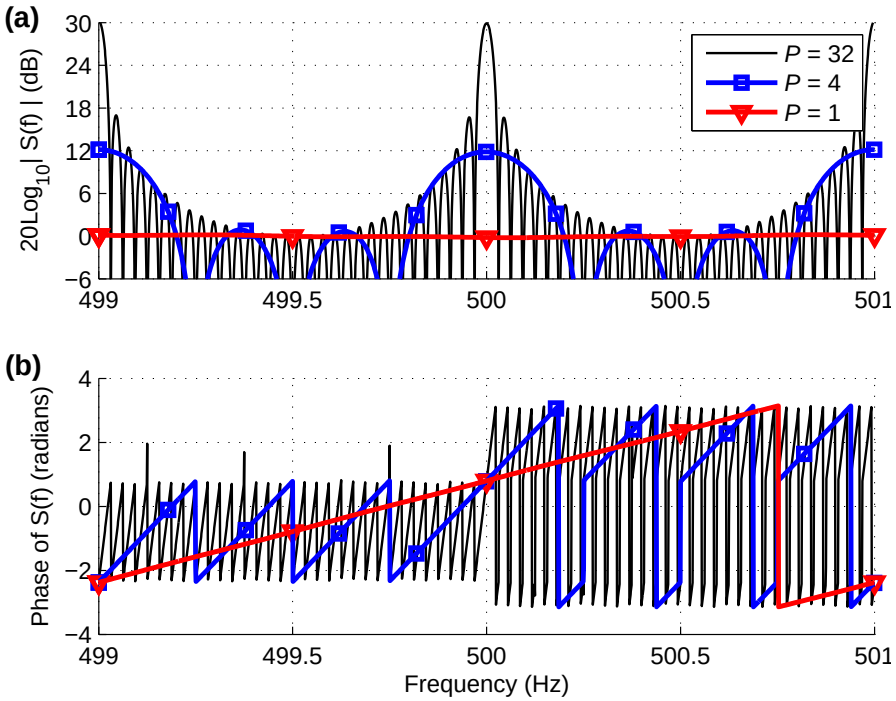

Figure 2.4: A section of the 100–900 Hz ($T_r = T = 1$ s) source spectrum for $P = [1, 4, 32]$ LFM pulses in (a) magnitude and (b) phase.

The ocean model is illustrated in Fig. 2.1. The model parameters are tabulated in Table 2.2. These range-independent parameters were based on previous SW06 inversion results [53–56]. The source is a 100–900 Hz LFM pulse with 1 s pulse width and PRI. Colored noise was generated using the measured power spectrum of SW06 noise data (see Fig. 2.11). The source is moving towards the static receiver. Frequency sampling usually is fixed at $\Delta f = 5$ Hz. The forward model used is KRAKEN [46].

2.3.1 Sensitivity analysis for static source and receiver with a single LFM pulse

Sensitivity plots for several parameters of a single LFM pulse noiseless reception and a static source and a receiver is simulated in Fig. 2.5. For each parameter, sensitivity plot is created by sweeping the parameter under test in the cost function while keeping the rest of the parameters at their baseline value. Be-

Table 2.2: Baseline model parameters.

Model parameters	value	Model parameters	value
Src range, r_0 (m)	2000	Sed. density, ρ_{sed} (g/cm^3)	1.8
Src depth, z_s (m)	30	Sed. attn., α_{sed} (dB/λ)	0.2
Rcv depth, z (m)	45	Sed. top. vel., c_1 (m/s)	1630
Src vel., v_s (m/s)	2.5	Sed. vel. slope, s (1/s)	0
Rcv vel., v_r (m/s)	0	Bot. density, ρ_{bot} (g/cm^3)	2.1
Water depth, z_w (m)	80	Bot. attn., α_{bot} (dB/λ)	0.2
Sed. depth, h_{sed} (m)	22	Bot. vel., c_b (m/s)	1740

cause the cost function Φ approaches negative infinity in dB for a perfectly matched field, the maximizing function $10\log_{10}(1-\Phi)$ is plotted instead. As expected, the geometric parameters such as water depth and source range are the most sensitive. These are followed by sediment velocity and density with intermediate sensitivity. The remaining bottom related parameters, such as sediment thickness and bottom halfspace velocity, are the least sensitive.

2.3.2 Multiple LFM pulses for a static source and receiver

Low SNR scenarios may arise from propagation loss or source level restrictions. In this simulation, with SNR fixed at -6 dB (calculated over LFM pulse bandwidth), coherently processing multiple LFM pulse receptions (source spectrum is Eq. (3.4)) can reduce data uncertainty (see Fig. 2.6). Frequency sampling is fixed at $\Delta f = 5$ Hz. Monte Carlo inversions of 200 noise realizations per P setting were carried out to assess uncertainty of the parameter estimates. Only four representative parameters (z_s, h_{sed}, c_1 and c_{bot}) of various sensitivities were chosen to keep the parameter search space small. The inversions were optimized using a genetic algorithm (GA). The values of the GA parameters are as follows: population size 16, selection 0.5, crossover 0.8, mutation 0.1, iterations 8, and parallel populations 8. Their parameter estimate distributions are plotted in Fig. 2.6 as histograms. The histograms are more informative than error bars (mean and

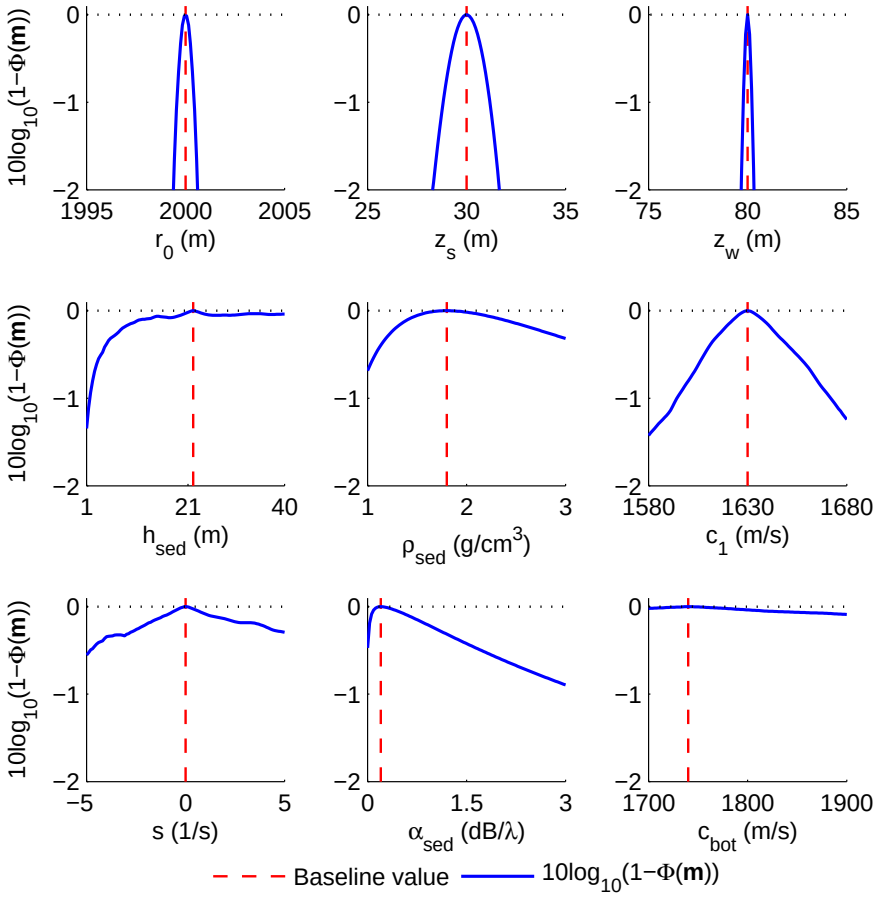

Figure 2.5: Sensitivity plots for a static source / receiver case.

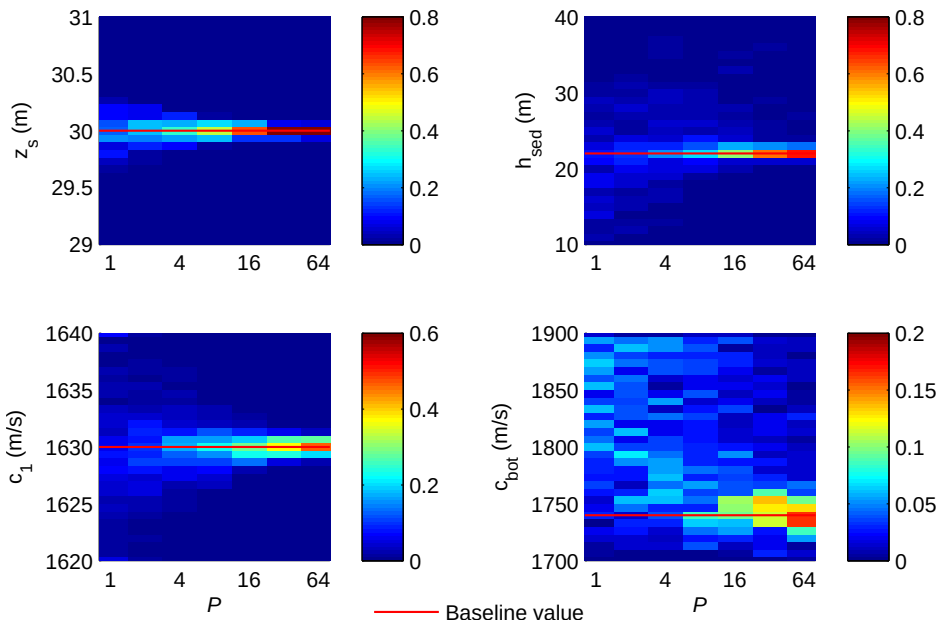

Figure 2.6: Histograms of four-parameter inversions for the static source and receiver case. The intensity plots are the histograms for the Monte Carlo simulation corresponding to 200 noise realizations with SNR fixed at -6 dB and number of LFM pulses $P = [1, 2, 4, 8, 16, 32, 64]$. Histograms are stacked vertically along the horizontal axis. Color bars indicate the relative frequency values.

standard deviation) as the cost surface may be skewed or have multiple minima giving rise to skewed or multiple peak histograms. Generally, bottom parameters (sediment thickness h_{sed} and bottom velocity c_b) required higher P values for low estimation uncertainty.

2.3.3 Multiple LFM pulses for a moving source and static receiver

For a moving source and static receiver case, there are mode-dependent frequency and wavenumber shifts. It is shown here that waveguide Doppler theory and a denser frequency sampling scheme are needed to exploit multiple LFM pulses coherently.

Applicability of waveguide Doppler processing

Waveguide Doppler [27–32] is more significant in certain circumstances. It depends on the type of shallow water waveguide, the source spectrum and the length of the source/receiver trajectory. When the bottom is hard, higher order modes will be relatively stronger than those for soft bottom. Correspondingly, the waveguide Doppler phenomenon will be more pronounced. Another factor is the source spectrum. Because a waveguide Doppler field traces back to several source frequencies, see Eq.(2.41), source spectrums (complex value) that vary more with frequency are more sensitive to waveguide Doppler. Lastly, the replica field for a moving source/receiver trajectory often is approximated with a static point field computation. Due to long observation time, this fails when the synthetic aperture exceeds several wavelengths during signal transmission and reception, respectively [31]. Here, the disparity arises from a moving source with a source spectrum consisting of concatenated LFM pulses. In this case, waveguide Doppler modeling is needed.

In Fig. 2.7(a), the moving source simulation is similar to previous static simulation except that the measured field is based on waveguide Doppler theory while the replica field assumes uniform Doppler [2,13]. Under the uniform Doppler assumption, the source spectrum is frequency shifted as if in free space, Eq. (2.53). The resulting source spectrum $S[\omega_s^{(v_s)}]$ then is propagated through the normal mode model, where all the modes are given the same Doppler shift for a given frequency.

$$\omega_s^{(v_s)} = \omega_r \left[1 - \frac{v_s}{c(z_s)} \right]. \tag{2.53}$$

At a given receiver frequency, the waveguide Doppler field comprises several contributing source frequencies due to mode-dependent Doppler, Eq. (2.41). When uniform Doppler is assumed, the source spectrum gets decoupled from the Green's function since Doppler is mode-independent. Therefore, a uniform Doppler field has only one contributing source frequency defined in Eq. (2.53). The mismatch between the waveguide and the uniform Doppler field increases with increasing P. This is because increasing P also increases the phase response slope of the source spectrum, see Fig. 2.4(b). These translate to parameter estimation errors. This is

observed in Fig. 2.7(a) (source depth z_s and top sediment velocity c_1). Generally, the parameter estimation histograms degrade with increasing P.

If no source motion is incorporated in the replica field, the estimation histograms will degrade even more (not shown here). When the replica is generated using waveguide Doppler theory, Fig. 2.7(b), there is decreasing parameter uncertainty for increasing $P \leqslant 16$. Thereafter, the parameter estimation degrades due to inadequate frequency sampling. In both cases, frequency sampling is done every 5 Hz for $P \leqslant 4$ since the peaks are either not present or difficult to detect due to noise [see Fig.(2.4)]. However, for $P \geqslant 8$, frequency sampling is done at every five spectral peaks (peaks are slightly more than $1/T_r = 1$ Hz apart due to Doppler).

Frequency Sampling

Ideally, all FFT frequencies in the LFM pulse band should be included in the processing. Practically, frequency sampling can be done at a far wider interval as long as there is no range aliasing lobes in the cost surface within the range search space [57]. The frequency sampling interval also should sample adequately the frequency-selective faded or interference-fringe received spectrum which contains information on the shallow water multipath impulse response [58,59]. This sampling criterion is approximately the inverse of the maximum multipath delay spread [17].

A moving source adds complexity to the frequency sampling approach. Fig. 2.8(a) is a simulated noiseless received spectrum from a moving source with spectrum shown in Fig. 2.4 propagating through the waveguide Doppler model described in Fig. 2.1 and Table 2.2. The 6 dB peak increments observed in the source spectrum for each doubling of pulses, see Fig. 2.4, is less consistent in the received spectrum in Fig. 2.8(a). For example, the 30 dB difference between $P = 1$ and $P = 32$ peaks in Fig. 2.4 corresponds to 36 dB in Fig. 2.8(a). Prior to modal summation, the spectrum for each mode is plotted in Fig. 2.8(b) to show their different modal Doppler shifts. Contrary to the static case, the mode-dependent Doppler in the complex-valued $S[\omega_s^{(k_n)}]$, as indicated in Fig. 2.8(b) and Eq. (2.41), will impose a different inter-modal interference which may cause the

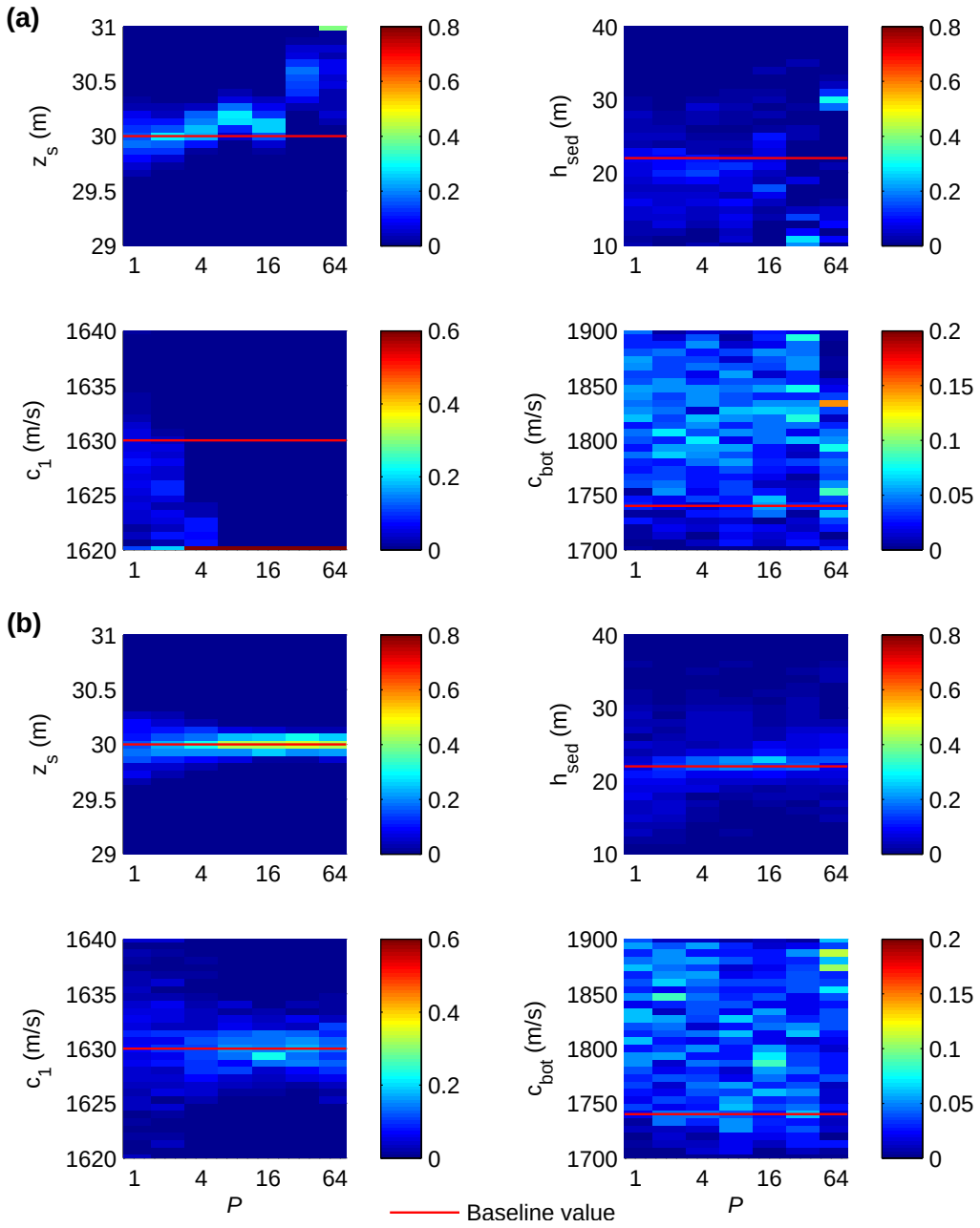

Figure 2.7: Histograms of four-parameter inversions for the moving source / static receiver case, SNR = −6 dB, and number of LFM pulses P with corresponding synthetic aperture of [2.5, 5, 10, 20, 40, 80, 160] m for (a) Uniform Doppler, and (b) Waveguide Doppler.

peak increments to deviate from 6 dB per doubling of pulses.

Note that as P increases, the spectral main lobes becomes smaller. Concentrating the energy into a narrowband lobe such that it is not larger than the Doppler spread, which is defined here as the Doppler difference between the most and least significant modes, will cause the modes to influence separate frequency bands. For $P = 32$, the peaks in Fig. 2.8(a) will have less influence of higher order modes due to the different modal Doppler shifts and stronger lower order modes [Fig. 2.8(b)]. Hence, sampling the spectral peaks will result in the loss of information from higher order modes. This has two effects [60]. First, there will be a loss of deeper bottom penetration as higher order modes have higher vertical wavenumbers (higher grazing angles). Second, there will be a loss of bottom resolution due to the loss of shorter vertical wavelength of higher order modes. These give higher estimation uncertainty for the bottom parameters as P becomes large, which is evident in Fig. 2.7(b) (see histograms for c_1 and h_{sed} for $P > 16$).

To correct this, it is necessary to sample multiple frequency points per spectral lobe in order to include all the modes within the Doppler spread, which in this case is $\pm$ 0.2 Hz. The results in Fig. 2.9 are obtained with this sampling approach and the performance is as good as the static case in Fig. 2.6. To save on computation, the replica field is evaluated only at the peak frequencies. The fields for the surrounding frequencies are computed using the modal functions at the peak frequencies and extrapolated wavenumbers via Taylor's approximation $k_n(\omega_r + \delta\omega_r) \approx k_n(\omega_r) + \delta\omega_r/u_{rn}$, see Eq. (2.39).

2.4 Experimental Data Analysis

The SW06 experiment was carried out near the shelf break on the New Jersey continental shelf from July to September 2006. A low SNR data set was chosen with a constant radial velocity moving source and static receiver over a range independent track, see Fig. 2.10. The acoustic data is from a 44.6 m deep single receiver, Channel 8 of a vertical line array (VLA1). On JD238 2029 UTC ($t = 0$), 64 LFM pulse (100–900 Hz) transmissions were made from a 30

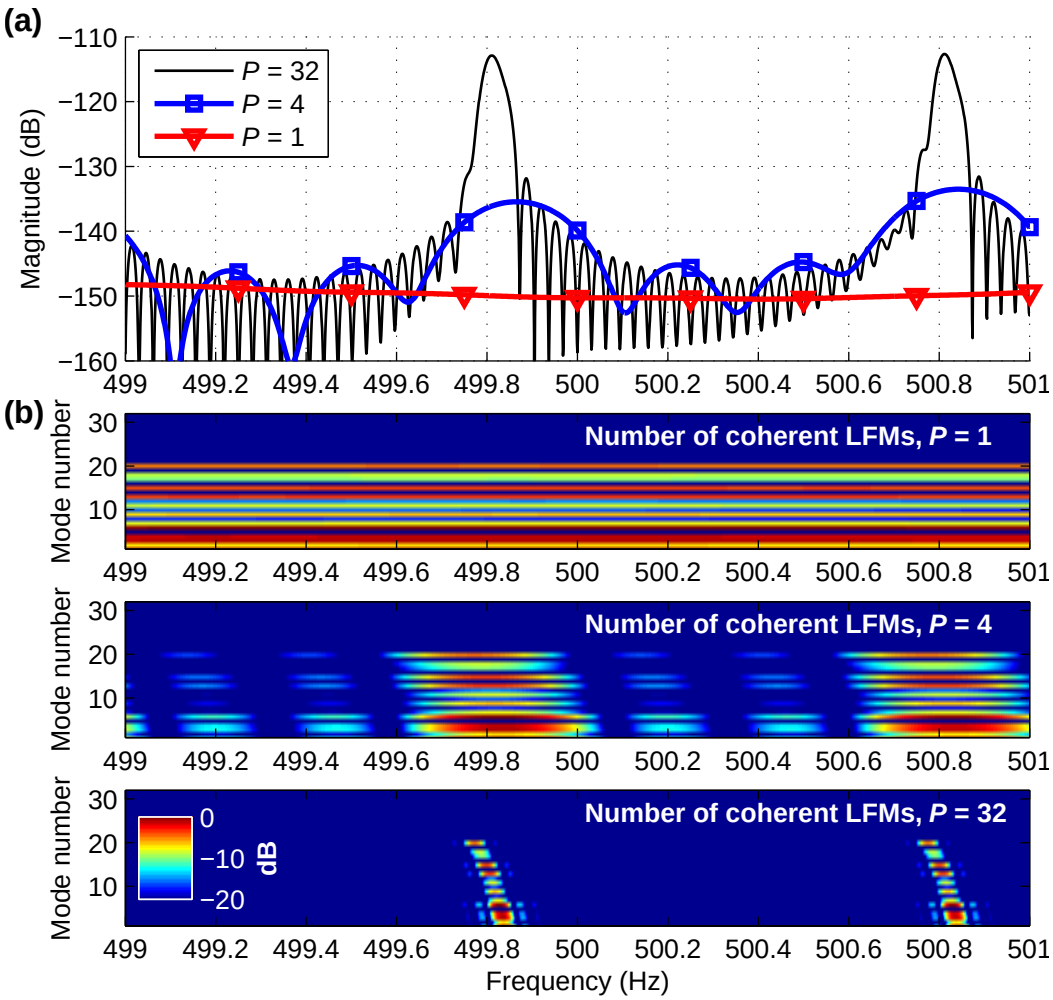

Figure 2.8: (a) Simulated received spectrum (499–501 Hz) for P=[1, 4, 32] with corresponding synthetic aperture of [2.5, 10, 80] m. (b) Same as (a) but prior to modal summation.

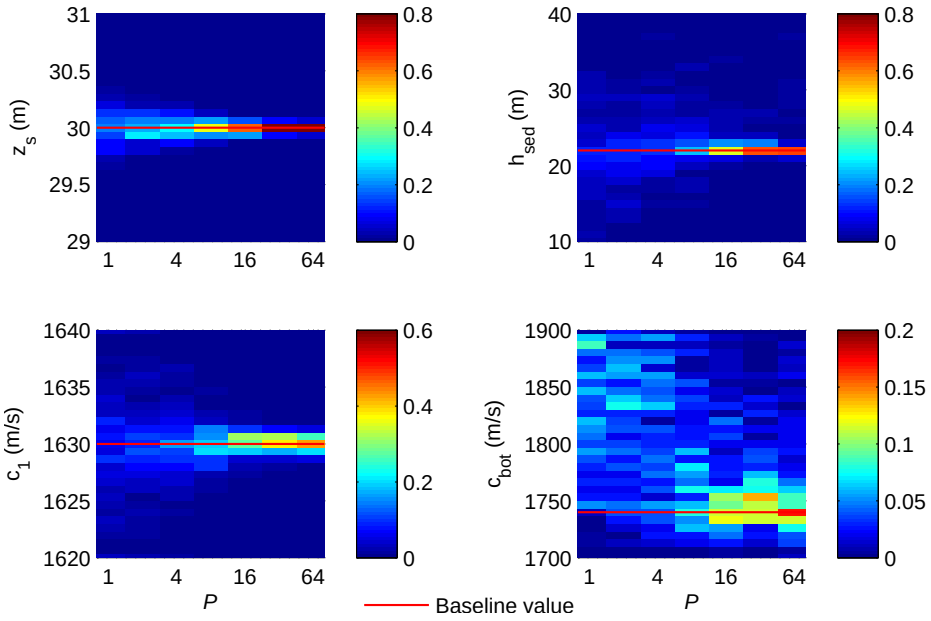

Figure 2.9: Histograms of four-parameter waveguide Doppler based inversions for the moving source / static receiver case, SNR = −6 dB and number of LFM pulses P with corresponding synthetic aperture of [2.5, 5, 10, 20, 40, 80, 160] m. Frequency sampling within ± 0.2 Hz band at every five spectral peaks.

m deep J-15 source towed by the R/V Knorr at 2.5 m/s between Waypoint 5 (WP5) and Waypoint 6 (WP6) towards VLA1. The LFM pulse width is 1 s and is repeated every second. Correspondingly, the towed source displacement or synthetic aperture is 2.5 m/s × 64 s = 160 m long. The R/V Knorr GPS range to VLA1 was 1981 m. Based on the ship and VLA1 positions, the actual source to VLA1 distance at $t = 0$ is estimated to be 2050–2100 m.

The power spectral density (PSD) of the received signal in Fig. 2.11 was generated from 60 s data. The SNR of the received signal was estimated to be 0.4 dB. Noise only data at 2024 UTC was added to the signal plus noise data at 2029 UTC to lower the SNR to −6 dB.

The nearest conductivity-temperature-depth (CTD) measurement was at 1905 UTC and about 1 km southwest of Waypoint 6 (WP6). Due to the lack of CTD measurements during this period and location, sound speed profile inversion using empirical orthogonal functions [53,54,61] (EOFs) were based on sound speed profiles (SSPs) derived from thermistors along the SHARK array, which have less

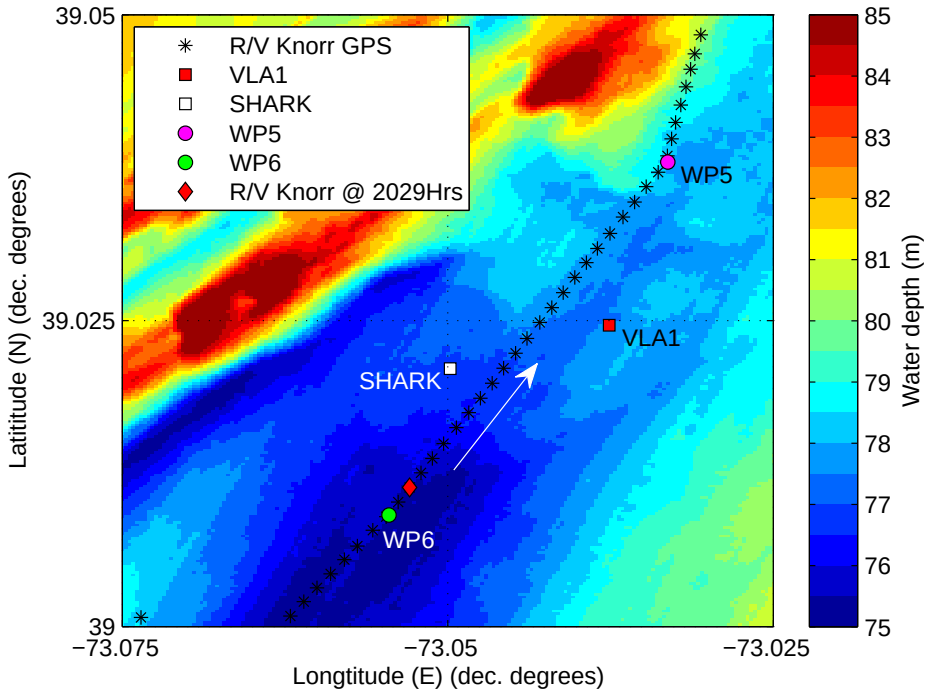

Figure 2.10: SW06 experiment site, bathymetry, source and receiver positions on JD238 (26 Aug 2006) 2000–2059 UTC.

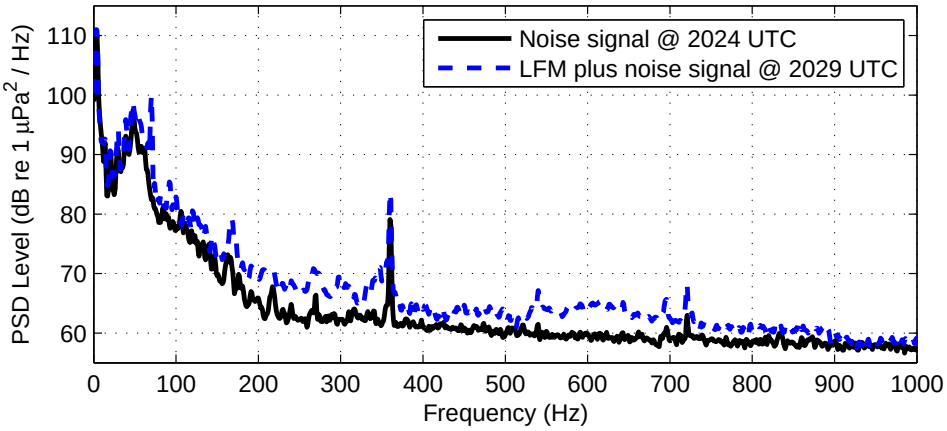

Figure 2.11: Power spectral density of received signal

depth resolution than the CTD measurements. On the other hand, the SHARK array is located in the middle between the source and VLA1. It also measured the temperatures every 30 s. To estimate the SSP, a constant salinity was assumed. Fig. 2.12(a) shows the SHARK derived SSPs over four hours. The SSPs varied between 10–70 m with the greatest velocity change at 40m. The water depth at the SHARK array was 79 m. In Fig. 2.12(b), the mean SSP and EOFs are derived from the SHARK SSPs.

Bottom reflection measurements and other analyses were done at the VLA1 site [53–56]. The bottom is characterized with a clay-rich sediment layer of lower velocities that is estimated to be around 1630 m/s $\pm$ 20 m/s. The R reflector was noted at 22 m $\pm$ 3 m based on vertical incidence chirp data.

2.4.1 Matched-field geoacoustic inversion

The inversion search bounds were set for the forward model depicted in Fig. 2.1 based on the background information at the experiment site. These are tabulated in Table 2.3. In addition, sensitivity analysis shows that parameters could be grouped into sensitive and insensitive sets. Sensitive parameters will usually dominate the inversion algorithm giving poor estimation results for insensitive parameters. Sensitive parameters are source range, source, receiver and water depth, source velocity, timing error and EOF1 and EOF2 coefficients. The matched field inversion algorithm used here is based on a multi-step approach [56] where the first step inversion inverted both sensitive and insensitive parameters and the second step inversion refine the results by significantly reducing (by a factor of 5) the search bounds of the sensitive parameters with the first step results. This gave better convergence rate for the insensitive parameters. GA performed the minimization of the cost function Eq. (2.48). The values of the GA parameters are as follows: population size 512, selection 0.5, crossover 0.8, mutation 0.02, iterations 32 and parallel populations 12. The search bounds for the first six parameters in Table 2.3 were set related to direct measurements, for example, GPS readings and the source depth sensor. The search bounds for the water SSP EOFs coefficients were determined from the distributions of the EOFs coefficients. The bounds for

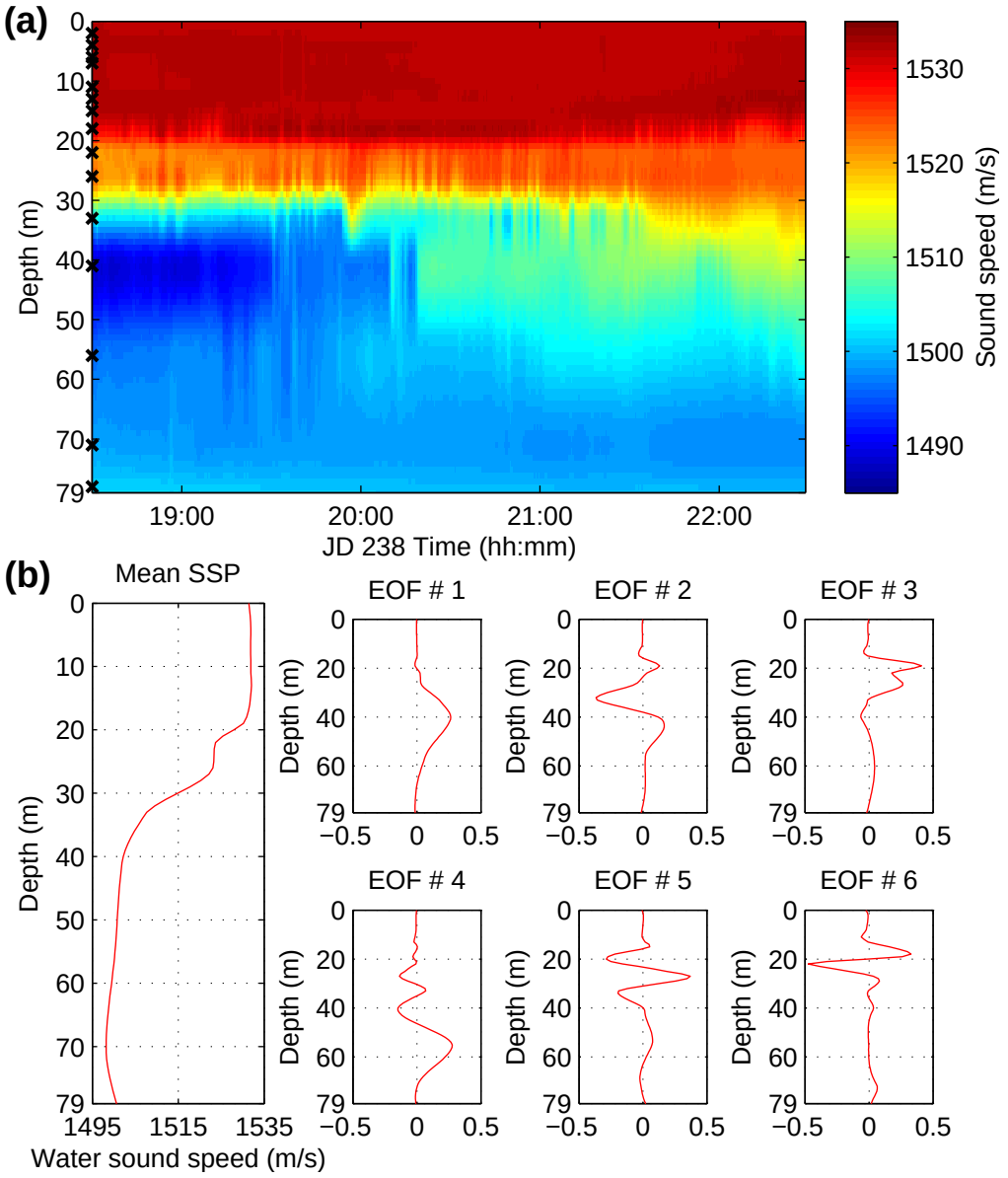

Figure 2.12: (a) SW06 SHARK interpolated sound speed profile from 1830–2229 UTC. Temperature sensor depths (×): 2, 4, 6, 7, 11, 13, 15, 18, 22, 26, 33, 41, 56, 71, 78 m. (b) Mean SSP and EOFs derived from SHARK SSPs.

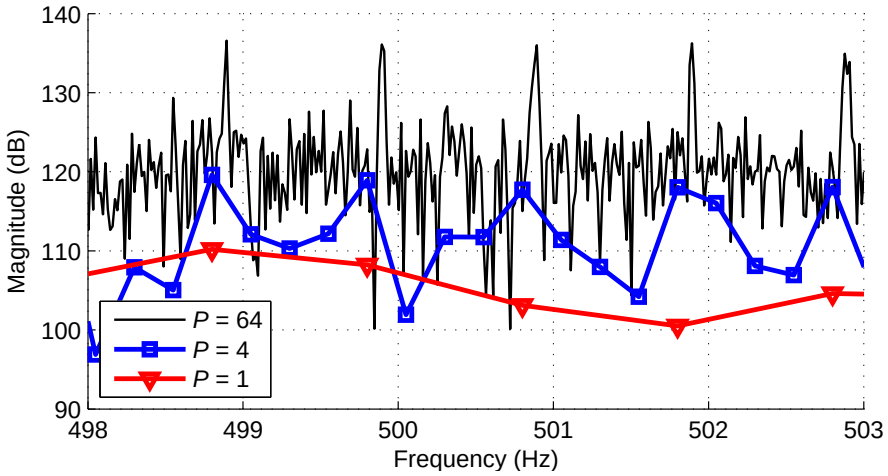

Figure 2.13: Section of SW06 received signal spectrum with LFM pulses $P = [1, 4, 64]$.

the last six bottom parameters in Table 2.3 were set based on empirical data [62] and some SW06 related publications [53–56].

Pre-processing of the single receiver data include LFM pulse matched filtering for coarse synchronization, data segmentation into various numbers of LFM pulse concatenations and finally, the fast Fourier Transform (FFT) of each data segment is carried out to obtain the measured field in the frequency domain. Fig. 2.13 shows the spectrum for $P = [1, 4, 64]$ where the spectral peaks for the 4 and 64 LFM pulses spectra can be seen clearly. The peaks in Fig. 2.13 are in agreement with the noise-free simulation in Fig. 2.8(a). Due to limited number of available LFM pulses and the large 18-parameter search space, estimation histograms, such as those simulated, cannot be replicated from the SW06 data. Only the $P = 64$ inversion results are shown here where the synthetic aperture length is 160 m long. The receiver frequencies were indexed according to the spectral peaks. Because $1/T_r = 1$ Hz, there are potentially 800 spectral peaks. For computational reasons, the frequency sampling is approximately every 5 Hz from 100–700 Hz. For each peak, frequency samples within ± 0.2 Hz were included. The FFT resolution is $(T_r P)^{-1}$.

Table 2.3 tabulates the inversion results using the waveguide Doppler model and the uniform Doppler model for 64 LFM pulses. For the waveguide Doppler

Table 2.3: SW06 data inversion parameters search bounds and results for $P = 64$.

Model parameters	Lower bound	Upper bound	Waveguide Doppler	Uniform Doppler
Src range, r_0 (m)	2050	2100	2075	2064
Src depth, z_s (m)	27	33	30.1	30.9
Rcv depth, z (m)	41	47	42.6	44.8
Timing error, ξ (msec)	-5	5	-1.3	2
Src vel., v_s (m/s)	2.3	2.8	2.55	2.53
Water depth, z_w (m)	72	82	75.6	77.4
EOF1 coef.	-50	50	30.1	5.9
EOF2 coef.	-25	25	3.8	3.6
EOF3 coef.	-10	10	1.2	0.6
EOF4 coef.	-10	10	-2.0	-1.9
EOF5 coef.	-10	10	6.1	7.5
EOF6 coef.	-6	2.5	-1.7	-3.0
Sed. dens., ρ_{sed} (g/cm^3)	1	2.5	2.01	1.73
Sed. attn., α_{sed} (dB/λ)	0.001	3	1.1	2.3
Sed. top. vel., c_1 (m/s)	1500	1700	1644	1549
Sed. vel. slope, s (1/s)	-10	10	6.2	3.5
Sed. thickness, h_{sed} (m)	10	40	22.8	22.2
Bot. vel., c_b (m/s)	1700	1900	1795	1812

model results, the estimated sediment thickness, velocity and density are consistent with other published results [53–56] at the MPL-VLA1 site. For example, these inversion results range from 1600–1650 m/s for the top sediment velocity and 21–25 m for the sediment thickness [53–56]. However, the sediment profile is estimated to have a positive gradient of about 6.2 m/s per m, while others [54–56] have estimated or assumed straight and negative gradient profiles. The top sediment velocity profile of the uniform Doppler model was not consistent and had a -100 m/s deviation when compared with other published results [53–56]. This also agree

with the uniform Doppler simulation results where the sediment velocity profile is negatively biased for increasing P, see Fig. 2.7(a) for c_1 top sediment velocity.

Scatter plots can be used to compare sensitivities and estimation uncertainties between the two inversions. Figs. 2.14 and 2.15 show the scatter plots, for selected parameters, of the cost function values plotted for waveguide Doppler and uniform Doppler evaluated in GA ($P = 64$). The scatter plots give information about the real sensitivities of the parameters by observing the envelopes of the scatter plots. A sharper minimum usually indicates lower estimation uncertainty. The geometric parameters, such as source depth, show high sensitivities since time/phase delay is important in signal correlation. The inversion is also sensitive to source radial velocity and could only tolerate mismatches on the order of 0.1 m/s [3rd row of Fig. 2.14(a)]. Source velocity sensitivity increases with P and synthetic aperture. Overall, the waveguide Doppler scatter plots indicate higher sensitivities and hence lower estimation uncertainties than the uniform Doppler. The waveguide Doppler scatter plots also show a lower minimum cost value indicating that it is a better model than the uniform Doppler. These observations are consistent with the simulation results.

Fig. 2.16 shows the estimated water column SSPs using the waveguide Doppler and the uniform Doppler models. Because the SSPs are range dependent in SW06 [53], the SHARK SSP measured at 2029 UTC is not a good substitute for a range independent SSP and, it gave inconsistent estimation results and a higher cost value. The EOFs have allowed the inversion to optimize the best range-independent SSP which is also the one using the waveguide Doppler model.

2.5 Conclusions

This chapter presented a single-receiver, broadband, frequency-coherent matched-field inversion approach that exploits coherently repeated transmissions at low SNR for a moving source and receiver. The long observation time creates a synthetic aperture due to relative source-receiver motion. The source transmission

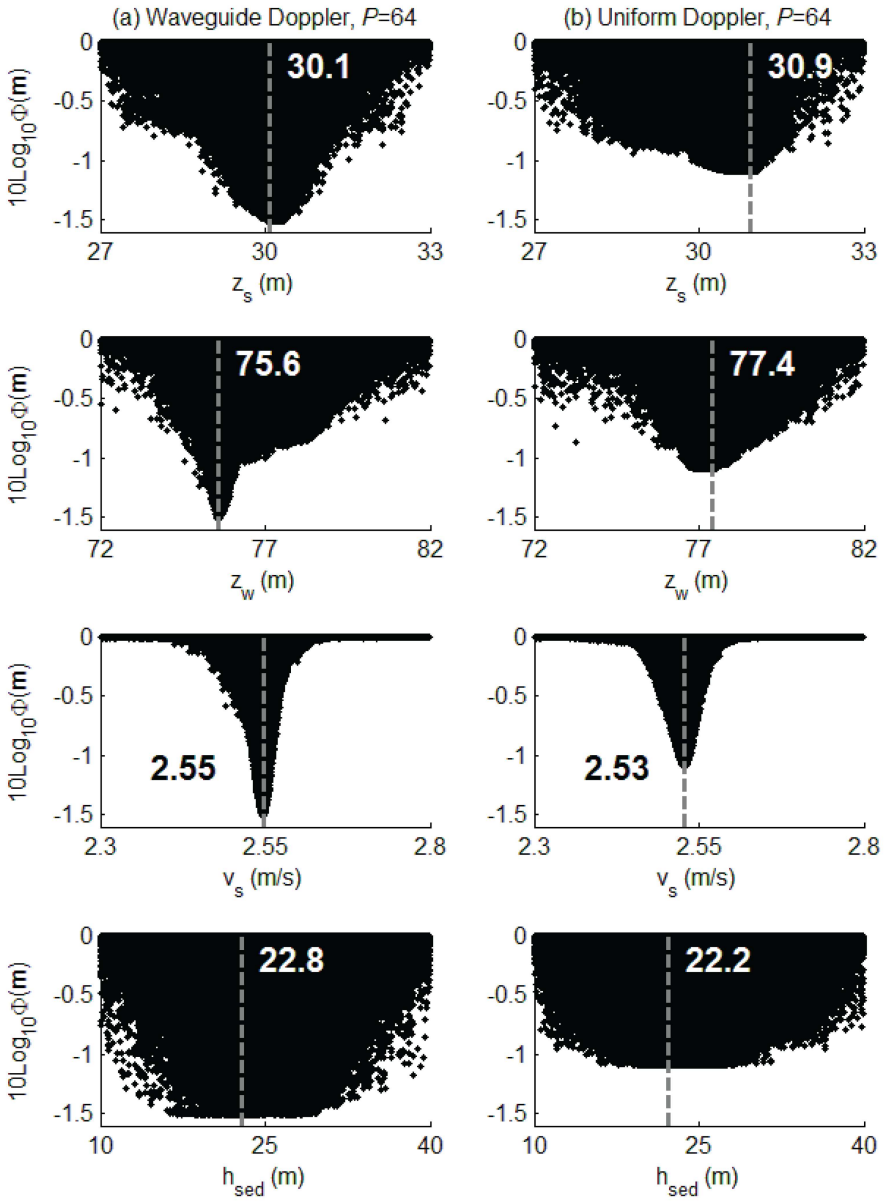

Figure 2.14: SW06 64 s data inversion scatter plots for $[z_s, z_w, v_s, h_{sed}]$ and $P = 64$ with a synthetic aperture of 160 m for (a) waveguide Doppler model and (b) uniform Doppler model. The vertical dashed line shows the final inversion results with SNR ≈ -6 dB.

consisted of multiple LFM pulses with a spectrum that approaches a multi-tonal comb with increasing Doppler sensitivity as the number of pulses increase. As a result, this requires incorporating waveguide Doppler in normal mode theory and increased frequency sampling around the spectral peaks.

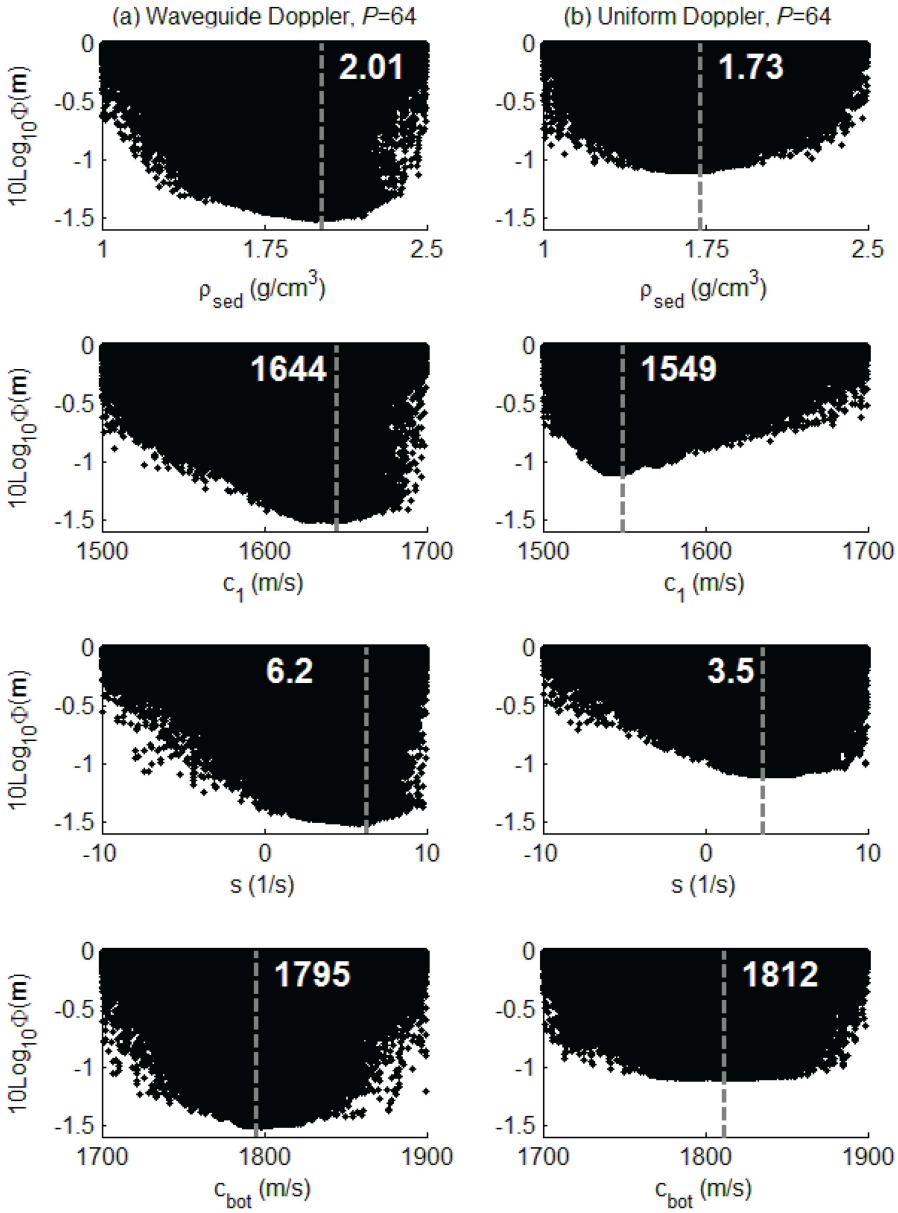

Figure 2.15: SW06 64 s data inversion scatter plots for $[\rho_{sed}, c_1, s, c_{bot}]$ and $P = 64$ with a synthetic aperture of 160 m for (a) waveguide Doppler model and (b) uniform Doppler model. The vertical dashed line shows the final inversion results with SNR ≈ -6 dB.

The waveguide Doppler inversion approach was demonstrated with low SNR data from the Shallow Water 2006 experiment with a moving source and static receiver configuration and 100–900 Hz LFM pulse transmissions. The inversion

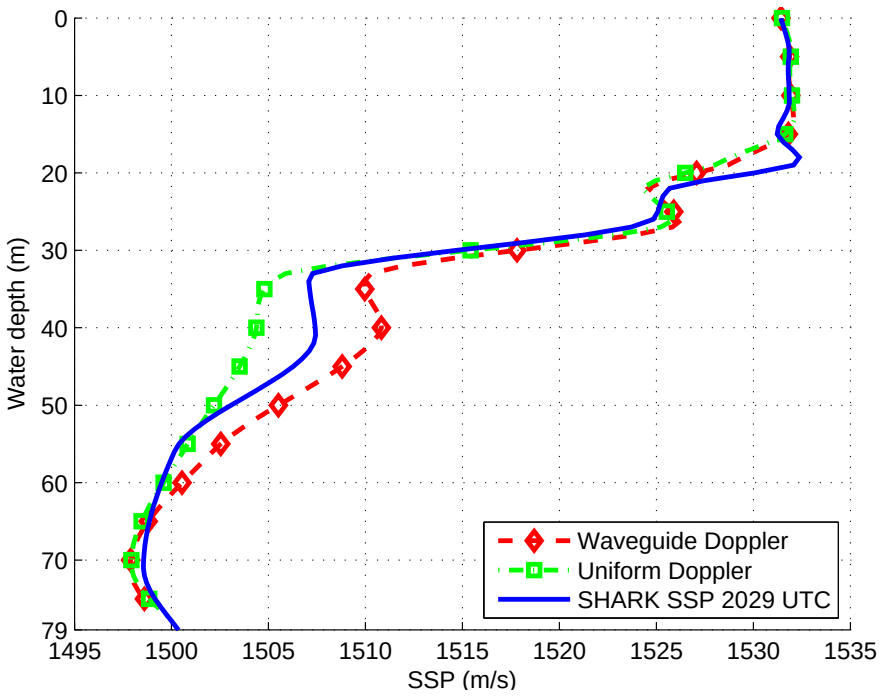

Figure 2.16: SSP inversion results using SW06 experimental data and $P = 64$ with waveguide Doppler and uniform Doppler models.

results agreed well with published results from the same site. On the other hand, the uniform Doppler model resulted in a sediment profile with a –100 m/s deviation, higher cost function value and less sensitive scatter plots.

Acknowledgments

This work was supported by the Office of Naval Research Grant No. N00014-11-0320 and the DSO National Laboratories of Singapore. The authors thank William Kuperman and Hee Chun Song for insightful discussions on Doppler in a shallow water waveguide, and Dave Ensberg for his help with the SW06 data. Chapter 2, in portion, is a reprint of material in the Journal of Acoustical Society of America as: B.A. Tan, P. Gerstoft, C. Yardim, W. Hodgkiss, "Broadband synthetic aperture geoacoustic inversion", *J. Acoust. Soc. Am.*, 134(1), 312–322, 2013. The dissertation author was the primary investigator and author of this paper.

Chapter 3

Recursive Bayesian synthetic aperture geoacoustic inversion in the presence of motion dynamics

3.1 Introduction

In Chapter 2, a single source and receiver, broadband, frequency coherent matched field inversion procedure was proposed [26]. It exploits coherently repeated transmissions to improve estimation of the geoacoustic parameters in low SNR conditions. The long observation time improves the SNR and creates a synthetic aperture due to relative source-receiver horizontal motion. However, due to the temporal extent of the data observation, source/receiver motion has to be taken in account using waveguide Doppler theory where each horizontal wavenumber or mode undergoes a different Doppler shift [26,29,30]. Though successful, the approach is limited to constant source/receiver radial velocities. Therefore, the assumptions are violated in the region near the closest point of approach (CPA) or when the radial velocities change. This chapter improves the broadband synthetic aperture geoacoustic inversion approach for cases where the radial velocity of the source/receiver changes. This is done through pulse-by-pulse coherent processing which in turn allows different source/receiver velocities.

Furthermore, processing a train of pulses all-at-once does not take advantage of the natural incremental acquisition of new data along with the ability to assess the temporal evolution of parameter uncertainty. Here, an equivalent pulse-by-pulse coherent processing approach using Bayesian updating is developed. With the Bayesian formulation, the estimated posterior distribution provides quantitative uncertainty analysis [35]. It also may be used to infer uncertainties in another usage domain (e.g. transmission loss [3]). This recursive Bayesian approach allows new data to be added incrementally without having to wait for all data to be present before processing can take place [36]. At present, most single source and receiver methods [5,8–16,18,19,26], except [37], do not use the Bayesian approach for uncertainty analysis.

The improved method is well suited for rapid environment assessment using a accelerated source and/or receiver as depicted in Fig. 3.1. The source or receiver may be towed horizontally by a ship or an autonomous underwater vehicle (AUV). Alternatively, a battery powered acoustic source may be dropped onto the ocean bottom to aid AUV-based geoacoustic inversion [21]. AUV-based inversions recently have been gaining research interest due to their operational attractiveness [22–25].

The theory of waveguide Doppler and modal propagation is reviewed briefly in Section 3.2, followed by the formulation of the inversion problem. Simulation results are presented in Section 3.3. Section 3.4 presents results from the analysis of low SNR, 100–900 Hz LFM data from the Shallow Water 2006 experiment.

3.2 Theory

An overview of the recursive Bayesian approach is illustrated in Fig. 3.2. At the lth measurement $\mathbf{y}_l$, the likelihood $p(\mathbf{y}_l|\mathbf{m})$ of the lth measurement conditioned on any particular set of model parameters $\mathbf{m}$ is computed (Sect. 3.2.2). This means computing the difference between the measured field $\mathbf{y}_l$ and the replica (modeled) field. Taking into the account of source/receiver motion, the replica field is generated using the waveguide Doppler model in Sect. 3.2.1.

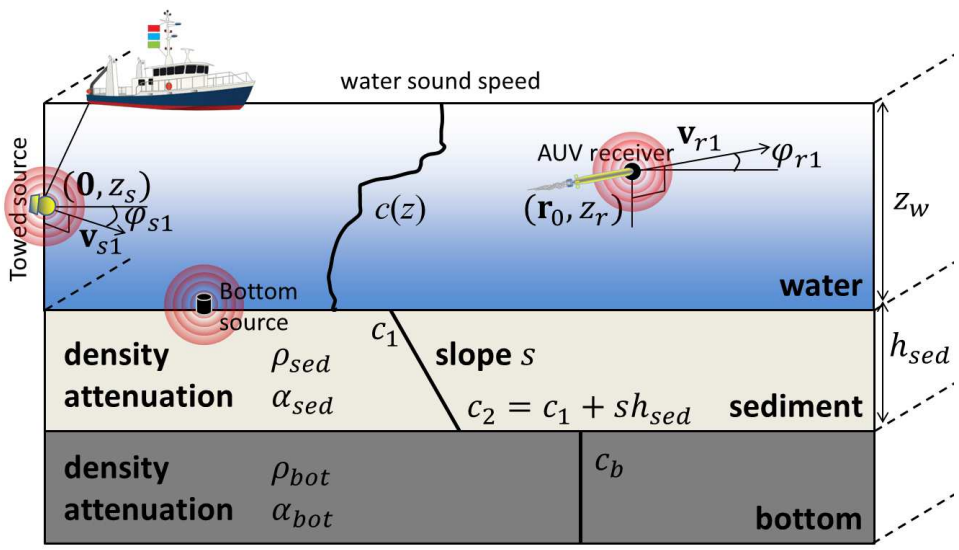

Figure 3.1: Horizontally stratified ocean with a horizontally moving source and receiver. The source is moving at initial velocity $\mathbf{v}_{s1}$ and bearing φ_{s1}, while the receiver is moving at initial velocity $\mathbf{v}_{r1}$ and bearing φ_{r1}. The range origin is the source position at time zero when the source begins transmitting.

The recursive Bayesian estimation approach is derived in Sect. 3.2.3. The general idea is to propagate the past posterior probability density $p(\mathbf{m}|\mathbf{y}_{1:l-1})$ as the prior information to improve the current posterior probability density $p(\mathbf{m}|\mathbf{y}_{1:l})$ with the current likelihood $p(\mathbf{y}_l|\mathbf{m})$ via Bayes' rule. The posterior density is represented with a set of samples of $\mathbf{m}$ and weights that are updated recursively as new measurements become available. However, as the posterior density evolves with the measurements, the importance density sampling the posterior density needs to adapt correspondingly where samples are added to the high probability regions of the posterior density. Sects. 3.2.4 and 2.2.3 address the implementation of the recursive Bayesian estimation approach using adaptive importance sampling (AIS) of the time-evolving posterior density.

The assumptions for the forward model and inversion approach are listed in Table 3.1.

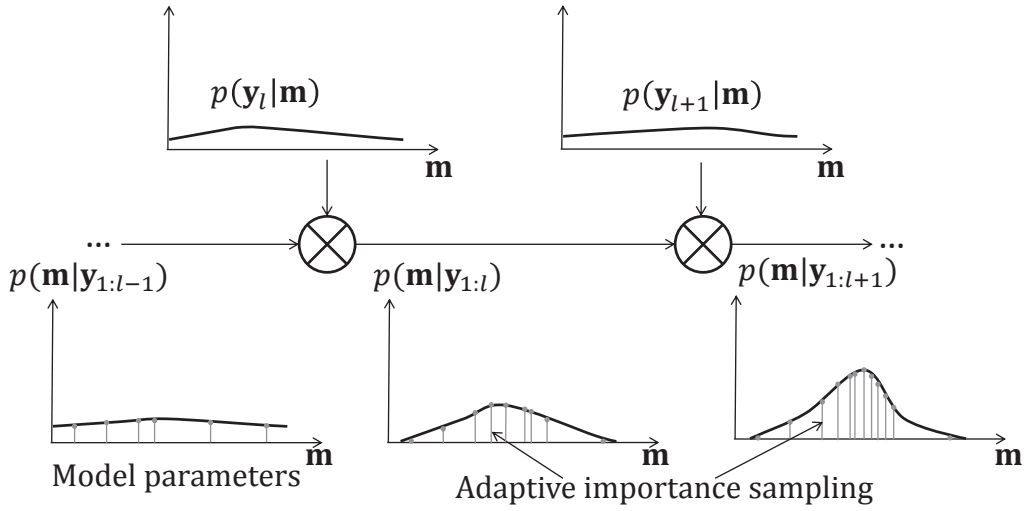

Figure 3.2: Recursive Bayesian approach. The lth measurement is $\mathbf{y}_l$ and $\mathbf{m}$ is the vector of model parameters. For illustration purpose, $\mathbf{m}$ is depicted here as a scalar. The posterior density $p(\mathbf{m}|\mathbf{y}_{1:l})$ is represented with a set of samples of $\mathbf{m}$ and weights. The importance density changes by introducing new samples from other densities as the posterior density evolves.

3.2.1 Waveguide Doppler theory model for acceleration dynamics

In a waveguide, the impact of Doppler is complicated due to multipath. Discussions of waveguide Doppler include Refs. [27–32]. In this chapter, waveguide Doppler due to source/receiver motion on a signal propagating in a range-independent waveguide is adapted from Schmidt and Kuperman [29,30]. Each horizontal wavenumber or mode undergoes a different Doppler shift. The scenario considered is depicted in Fig. 3.1. Based on constant source and receiver velocities and depth constraints, and a positive-exponent Fourier transform convention, the waveguide Doppler shifted field via a normal mode representation is [26]:

$$\psi(\mathbf{r}, z_r, \omega_r) \approx \frac{ie^{-i\frac{\pi}{4}}}{\sqrt{8\pi}\rho(z_s)} \sum_n S[\omega_s^{(k_n)}] \times \Psi_n(z_r;\omega_r)\Psi_n(z_s;\omega_r)\frac{e^{ik_n r_0}}{\sqrt{k_n r_0}} \tag{3.1}$$

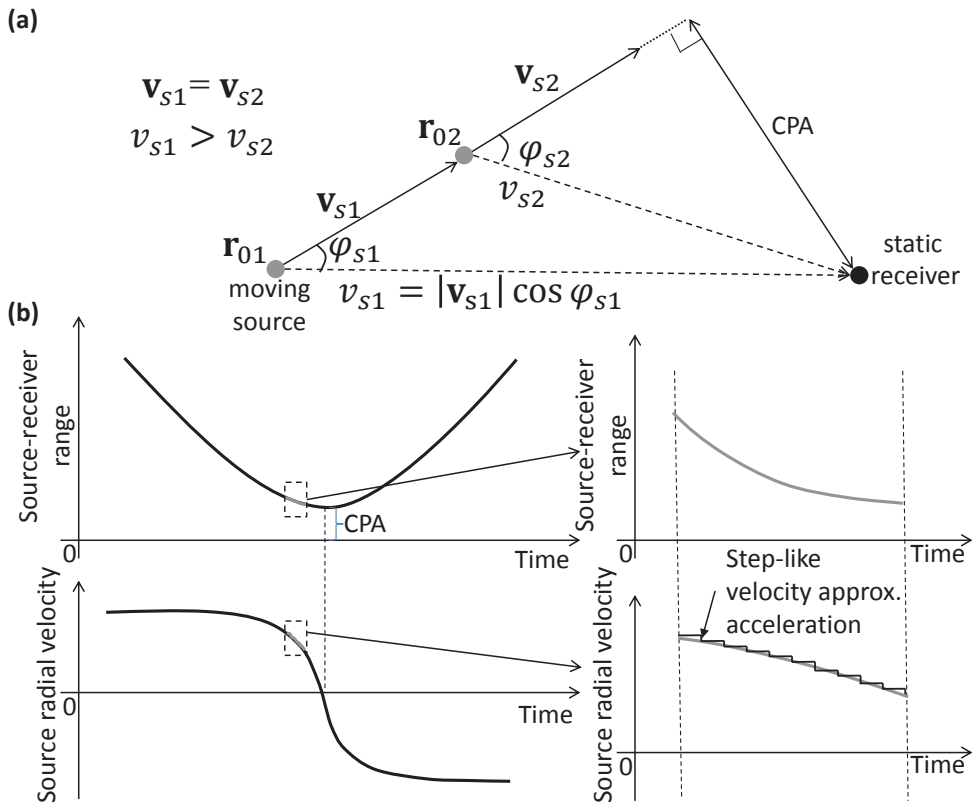

Figure 3.3: (a) Top view of a constant velocity source with changing radial velocity to the receiver due to the geometry of source/receiver positions. (b) Source–receiver range and radial velocity curves near CPA. Here, the change in source radial velocity in the dotted box approximately is linear with time corresponding to a constant acceleration.

where

$$\omega_s^{(k_n)} = \omega_r - k_n(v_s - v_r), \tag{3.2}$$

$$k_n \approx \frac{k_{rn}}{(1 - \frac{v_r}{u_{rn}})}, \tag{3.3}$$

$$S(\omega_s) = \sum_{l=1}^{L} \exp[i\omega_s(l-1)T_r] S_c(\omega_s). \tag{3.4}$$

r_0 is the source-receiver separation at $t = 0$. v_s, v_r, z_s and z_r are the radial source and receiver velocities and depths, respectively. $\rho(z_s)$ is the water density. k_n and Ψ_n are the modal wavenumbers and modal functions evaluated at propagation frequencies ω. For numerical efficiency, constructing the field in Eq. (3.1) is

facilitated by some approximations to the propagation modal wavenumbers and functions that are computed instead at the receiver frequency ω_r [see Eqs. (3.1) and (3.3)]. $\omega_s^{(k_n)}$ is the mode-dependent source frequency mapping function used to construct the field at ω_r. $u_{rn} = \frac{d\omega_r}{dk_n(\omega_r)}$ is the nth modal group velocity and $k_{rn} = k_n(\omega_r)$ is the nth modal wavenumber, both evaluated at ω_r. $S(\omega_s)$ is the source spectrum of L pulses representing the amplitude and phase of the moving point source. T_r is the pulse repetition interval (PRI) and $S_c(\omega_s)$ is the spectrum of the common or repeated source transmission.

When the source traverses past the receiver, the radial velocity v_s changes even though the source velocity $\mathbf{v_s}$ is constant (see Fig. 3.3). As shown later in Sec. 3.3, acceleration needs to be modeled in order to perform a meaningful inversion near the CPA. However, modeling acceleration is non-trivial as it results in time-dependence in the modal wavenumbers and modal functions [63]. As an approximation to a constant acceleration, a practical approach is to assume multiple short duration transmissions, e.g. multiple pulses as in Eq. (3.4), where the source/receiver radial velocities are assumed piecewise constant for the lth pulse but linearly changing from pulse to pulse. Therefore, the field can be generated for each pulse and coherently combined for L pulses to form the received spectrum. Substituting Eqs. (3.4) and (3.2) into Eq. (3.1) and introducing pulse number dependent radial velocities, the replica field may be represented as a sum of L fields $\psi_l(\mathbf{r}, z_r, \omega_r)$ such that

$$\psi(\mathbf{r}, z_r, \omega_r) = \sum_{l=1}^{L} \psi_l(\mathbf{r}, z_r, \omega_r) \tag{3.5}$$

where

$$\begin{aligned}\psi_l(\mathbf{r}, z_r, \omega_r) =& \frac{ie^{-i\frac{\pi}{4}}}{\sqrt{8\pi}\rho(z_s)} \exp[i\omega_r(l-1)T_r] \sum_n S_c[\omega_s^{(k_n,l)}] \\ & \times \Psi_n(z_r;\omega_r)\Psi_n(z_s;\omega_r)\frac{e^{ik_{nl}r_{0l}}}{\sqrt{k_{nl}r_{0l}}}\end{aligned} \tag{3.6}$$

$$\omega_s^{(k_{nl})} = \omega_r - k_{nl}(v_{sl} - v_{rl}), \tag{3.7}$$

$$k_{nl} \approx \frac{k_{rn}}{(1 - \frac{v_{rl}}{u_{rn}})}, \tag{3.8}$$

$$v_{sl} = v_{s1} + (l-1)T_r a_s, \tag{3.9}$$

$$v_{rl} = v_{r1} + (l-1)T_r a_r, \tag{3.10}$$

and

$$r_{0l} = \begin{cases} r_0, & \text{if } l = 1, \\ r_0 + \sum_{j=1}^{l-1} T_r(v_{rj} - v_{sj}), & \text{if } l = 2, \ldots, L. \end{cases} \tag{3.11}$$

Each pulse is propagated in the forward model with its corresponding values of v_{sl} and v_{rl} then coherently combined in Eq. (3.5). Note that all L pressure fields still are referenced to $t = 0$. In Eq. (3.8), the horizontal wavenumber k_{nl} depends on mode n and pulse number l. Hence, there also are mode and pulse number dependent frequency mappings when tracing back to ω_s in order to construct the field at ω_r, see Eq. (3.7). As an approximation to a constant acceleration, the source/receiver radial velocities v_{sl} and v_{rl} [Eqs. (3.9) and (3.10)] are modeled to be piecewise constant for the lth pulse but linearly changing from pulse to pulse. a_s and a_r are the source and receiver radial accelerations, respectively.

3.2.2 Likelihood functions

The broadband data model for frequency-coherent match-field based geoacoustic inversion can be expressed as L measurement vectors,

$$\mathbf{y}_l = \alpha \mathbf{E}(\xi)\mathbf{d}_l(\mathbf{m}) + \mathbf{g}_l = \alpha \mathbf{b}_l(\xi, \mathbf{m}) + \mathbf{g}_l \tag{3.12}$$

where $\mathbf{y}_l = [y_l(\omega_{r1}) \ldots y_l(\omega_{rJ})]^{\mathrm{T}}$ is the K-point fast Fourier transform (FFT) of the observed time series capturing the lth pulse for J discrete frequencies. Note the lth pulse Fourier transforms are synchronized to the first pulse transmission time ($t = 0$) so that only one timing error ξ between the source and receiver clocks needs to be resolved. $\mathbf{E}(\xi)$ is a diagonal matrix for correcting the timing error, $\mathbf{E}(\xi) = \mathrm{diag}[e^{i\omega_{r1}\xi} \ldots e^{i\omega_{rJ}\xi}]$. $\mathbf{m}$ is the subset of forward model parameters that are being estimated (see Fig. 3.1). α is a scale factor representing the unknown source level. To introduce source/receiver motion or waveguide Doppler, the corresponding replica field $\mathbf{d}_l(\mathbf{m}) = [\psi_l(\omega_{r1}, \mathbf{m}) \ldots \psi_l(\omega_{rJ}, \mathbf{m})]^{\mathrm{T}}$ is generated using Eq. (3.6) with vector $\mathbf{m}$. It is assumed the model parameters $\mathbf{m}$, α and ξ do not change

between measurements and thus the joint likelihood function will sharpen as L increases.

The distribution of the error vector $\mathbf{g}_l = [g_l(\omega_{r1}) \dots g_l(\omega_{rJ})]^{\mathrm{T}}$ defines the likelihood function. It is assumed that $\mathbf{g}_l$ for $l = 1, \dots, L$ are independent and identically distributed (i.i.d.) across L measurements. Error consists of both ambient noise and modeling errors. For low SNR processing, the colored ambient noise will be considered the dominant source of error. The frequency-dependent noise is modeled as a wide sense stationary noise $u[n]$ with power spectral density $P_{uu}(\omega_r)$. $P_{uu}(\omega_r)$ is estimated from noise only data prior to the pulse transmissions.

Taking a K-point FFT of $u[n]$, let the lth error vector $\mathbf{g}_l$ be the FFT of $u[n]$ evaluated at frequencies $[\ \omega_{r1} \dots \omega_{rJ}\ ]$ with $J \leqslant K$. We will define the frequency domain noise $\mathbf{g}_l$ as complex Gaussian with mean $\mathrm{E}[\mathbf{g}_l] = \mathbf{0}$ for $\omega_r \neq 0$ and autocovariance [51]

$$\mathbf{C}_{\mathbf{g}} = \mathrm{E}[\mathbf{g}_l \mathbf{g}_l^{\mathrm{H}}] = \gamma \mathrm{diag}[P_{uu}(\omega_{r1}) \ \dots \ P_{uu}(\omega_{rJ})], \tag{3.13}$$

where γ is a scale factor for scaling the noise spectrum in the data inversions. Thus, it is assumed that the error vector $\mathbf{g}_l \sim \mathcal{CN}(\mathbf{0}, \mathbf{C}_{\mathbf{g}})$. Factoring $\mathbf{C}_{\mathbf{g}} = \gamma \tilde{\mathbf{C}}_{\mathbf{g}}$ with $\tilde{\mathbf{C}}_{\mathbf{g}} = \mathrm{diag}[P_{uu}(\omega_{r1}) \ \dots \ P_{uu}(\omega_{rJ})]$, the joint likelihood function of the L measurements can be expressed as (based on i.i.d. measurements)

$$\begin{aligned} \mathcal{L}(\tilde{\mathbf{m}}) = p(\mathbf{y}_{1:L}|\tilde{\mathbf{m}}) = \prod_{l=1}^{L} p(\mathbf{y}_l|\tilde{\mathbf{m}}) = \prod_{l=1}^{L} \frac{1}{(\pi\gamma)^J |\tilde{\mathbf{C}}_{\mathbf{g}}|} \times \\ \exp\big\{ -[\mathbf{y}_l - \alpha \mathbf{b}_l(\xi, \mathbf{m})]^{\mathrm{H}} \tilde{\mathbf{C}}_{\mathbf{g}}^{-1} [\mathbf{y}_l - \alpha \mathbf{b}_l(\xi, \mathbf{m})] \ / \ \gamma \big\} \end{aligned} \tag{3.14}$$

where supervector $\mathbf{y}_{1:L} = [\mathbf{y}_1^{\mathrm{T}}, \dots, \mathbf{y}_L^{\mathrm{T}}]^{\mathrm{T}}$ and $\tilde{\mathbf{m}} = [\mathbf{m}^{\mathrm{T}}, \gamma, \alpha, \xi]^{\mathrm{T}}$. To simplify the notation, $\mathbf{m}$ is now redefined to also include γ, α and ξ. For this empirical Bayesian estimation problem, α and γ are estimated jointly with the model parameters [3], instead of incorporating their maximum likelihood estimates (MLE) as in [26].

3.2.3 Recursive Bayesian estimation

In low SNR conditions, long time integration is necessary for acceptable parameter estimation uncertainty. The time-dependent source-receiver range can

be recast into a set of initial value and constant parameters. This reformulation includes initial value parameter such as initial source range r_0 at $(t = 0)$ [Eq. (3.11)], initial velocities v_{s1} and v_{r1} and constant accelerations a_s and a_r [Eqs. (3.9) and (3.10)] for use with the waveguide Doppler model [Eqs. (3.5) and (3.6)]. Thus, the need to track [64,65] the time-dependent source-receiver range is circumvented and the measurements accumulate and improve the likelihood/posterior densities. It is assumed that other model parameters, such as the seafloor properties, do not change for the L measurements.

Recursive Bayesian estimation approach is inspired by recursive Bayesian online learning and particle filter theories [36,66–69]. With initial prior knowledge of the parameters $p(\mathbf{m})$ and Bayes' rule, the joint posterior probability density function (PPD) of the model parameters for l pulse measurements is [36]

$$p(\mathbf{m}|\mathbf{y}_{1:l}) = \frac{p(\mathbf{y}_{1:l}|\mathbf{m})p(\mathbf{m})}{p(\mathbf{y}_{1:l})} \tag{3.15}$$

$$\begin{aligned} &= \frac{p(\mathbf{y}_{1:l}|\tilde{\mathbf{m}})p(\tilde{\mathbf{m}})}{\int p(\mathbf{y}_{1:l}|\tilde{\mathbf{m}})p(\tilde{\mathbf{m}})\mathrm{d}\tilde{\mathbf{m}}} \\ &= \frac{p(\mathbf{y}_l|\tilde{\mathbf{m}})p(\mathbf{y}_{1:l-1}|\tilde{\mathbf{m}})p(\tilde{\mathbf{m}})}{\int p(\mathbf{y}_l|\tilde{\mathbf{m}})p(\mathbf{y}_{1:l-1}|\tilde{\mathbf{m}})p(\tilde{\mathbf{m}})\mathrm{d}\tilde{\mathbf{m}}} \\ &= \frac{p(\mathbf{y}_l|\tilde{\mathbf{m}})p(\tilde{\mathbf{m}}|\mathbf{y}_{1:l-1})p(\mathbf{y}_{1:l-1})}{\int p(\mathbf{y}_l|\tilde{\mathbf{m}})p(\tilde{\mathbf{m}}|\mathbf{y}_{1:l-1})p(\mathbf{y}_{1:l-1})\mathrm{d}\tilde{\mathbf{m}}} \\ &= \frac{p(\mathbf{y}_l|\mathbf{m})p(\mathbf{m}|\mathbf{y}_{1:l-1})}{\int p(\mathbf{y}_l|\mathbf{m})p(\mathbf{m}|\mathbf{y}_{1:l-1})\mathrm{d}\mathbf{m}}. \end{aligned} \tag{3.16}$$

Eq. (3.16) shows that the joint posterior density conditioned on l measurements can be updated recursively from the lth likelihood and the joint posterior density of the $l-1$ measurements. Thus Bayesian updating of $p(\mathbf{m}|\mathbf{y}_{1:l})$ can be done all at once [Eq.(3.15)] or recursively over time [Eq.(3.16)]. In addition, assuming constant geoacoustic model parameters for all l, no model mismatch error and no bias error between the replica and measured fields, the variance of the maximum a posteriori (MAP) parameter estimate,

$$var[\hat{\mathbf{m}}_{MAP}^{(L)}] < var[\hat{\mathbf{m}}_{MAP}^{(L-1)}] < \ldots < var[\hat{\mathbf{m}}_{MAP}^{(1)}] \tag{3.17}$$

where

$$\hat{\mathbf{m}}_{MAP}^{(L)} = \arg\max_{\mathbf{m}} p(\mathbf{m}|\mathbf{y}_{1:L}) = \arg\max_{\mathbf{m}} p(\mathbf{m}) \prod_{l=1}^{L} p(\mathbf{y}_l|\mathbf{m}) \tag{3.18}$$

Ideally, the posterior density converges to a Dirac delta function centered at the true parameter value as L approaches infinity [36]. Practically, it is difficult to attain the true parameter value as there will be some model mismatch error or bias in the estimator. In addition, only a limited number of measurements can be processed before time-dependent variations in the model parameters and model mismatch errors become significant.

3.2.4 Recursive Monte Carlo integration and importance sampling

The posterior density $p(\mathbf{m}|\mathbf{y}_{1:l})$ is used to compute metrics of interest such as the MAP estimates, posterior means, variances and marginal PPDs of the model parameter m_i [35,52](see Eqs. 3.18, 3.19–3.22). A way of generating these metrics is Monte Carlo integration and importance sampling [70–73]. Compared to Markov Chain Monte Carlo methods which sequentially sample the posterior density, the primary appeal of importance sampling is the ability to carry out large-scale sampling of the posterior density in parallel. These metrics also can be updated as new data is made available [see Eqs. (3.27)–(3.29)].

$$\mu_i = \int m_i \; p(\mathbf{m}|\mathbf{y}_{1:l}) \; \mathrm{d}\mathbf{m} \tag{3.19}$$

$$\sigma_i^2 = \int (m_i - \mu_i)^2 \; p(\mathbf{m}|\mathbf{y}_{1:l}) \; \mathrm{d}\mathbf{m} \tag{3.20}$$

$$p(m_i|\mathbf{y}_{1:l}) = \int \delta(m_i{}' - m_i) \; p(\mathbf{m}'|\mathbf{y}_{1:l}) \; \mathrm{d}\mathbf{m}' \tag{3.21}$$

$$p(m_i, m_j|\mathbf{y}_{1:l}) = \int \delta(m_i{}' - m_i)\delta(m_j{}' - m_j) \times p(\mathbf{m}'|\mathbf{y}_{1:l}) \; \mathrm{d}\mathbf{m}' \tag{3.22}$$

For a parameter of interest such as the water column sound speed profile (SSP), c_w, that is inferred from the inversion and is a function of empirical orthogonal functions (EOFs) and coefficients [26,53,54,61], $c_w = C(\mathbf{m})$, the probability distribution of c_w is [3,35]

$$p(c_w|\mathbf{y}_{1:l}) = \int \delta[c_w - C(\mathbf{m})]p(\mathbf{m}|\mathbf{y}_{1:l}) \; \mathrm{d}\mathbf{m}. \tag{3.23}$$

As shown later in Sect. 3.4.1, Eq. (3.23) is used to plot the SSP estimation uncertainty in Figs. 3.12–3.14. Using the Monte Carlo integration method [70–73], these integrals are of the form,

$$\int h(\mathbf{m})p(\mathbf{m}|\mathbf{y}_{1:l})\ \mathrm{d}\mathbf{m} = \mathrm{E}[h(\mathbf{m})] \approx \frac{1}{Q}\sum_{q=1}^{Q} h(\mathbf{m}^q), \tag{3.24}$$

where the samples $\{\mathbf{m}^q, q = 1, \ldots, Q\}$ are drawn from the distribution $p(\mathbf{m}|\mathbf{y}_{1:l})$. Drawing samples from $p(\mathbf{m}|\mathbf{y}_{1:l})$ is difficult as it usually is a non-standard and high dimensional probability density function (PDF) [71,72]. Alternatively, a standard or importance density $x(\mathbf{m})$ may be used to generate the samples. This is known as importance sampling [70–72]. Therefore,

$$\int h(\mathbf{m})p(\mathbf{m}|\mathbf{y}_{1:l})\ \mathrm{d}\mathbf{m} \approx \frac{\sum_{q=1}^{Q} h(\mathbf{m}^q)\tilde{w}_l^q}{\sum_{j=1}^{Q} \tilde{w}_l^j} \tag{3.25}$$

where

$$\tilde{w}_l^q = \frac{p(\mathbf{y}_{1:l}|\mathbf{m}^q)p(\mathbf{m}^q)}{x(\mathbf{m}^q)} \tag{3.26}$$

are the unnormalized weights and they correct under– and over–represented samples drawn from $x(\mathbf{m})$ instead of $p(\mathbf{m}|\mathbf{y}_{1:l})$. However, Eqs. (3.25) and (3.26) are non-recursive. As new data is made available, the weights may be computed recursively as [66–68]

$$\tilde{w}_l^q = p(\mathbf{y}_l|\mathbf{m}^q)\tilde{w}_{l-1}^q. \tag{3.27}$$

Let normalized weights be $w_l^q = \tilde{w}_l^q / \sum_{j=1}^{j=Q} \tilde{w}_l^j$. Eq.(3.25) becomes

$$\int h(\mathbf{m})p(\mathbf{m}|\mathbf{y}_{1:l})\ \mathrm{d}\mathbf{m} \approx \sum_{q=1}^{Q} h(\mathbf{m}^q)w_l^q. \tag{3.28}$$

Eqs. (3.27) and (3.28) are recognized as an implementation of Eq. (3.16). The PPD can be approximated by [66,67]

$$p(\mathbf{m}|\mathbf{y}_{1:l}) \approx \sum_{q=1}^{Q} \delta(\mathbf{m} - \mathbf{m}^q)w_l^q, \tag{3.29}$$

and it approaches the true PPD as $Q \to \infty$. For comparison, see Eqs. 3.21 and 3.22.

3.2.5 Adaptive importance sampling

The PPDs, $p(\mathbf{m}|\mathbf{y}_{1:l})$, evolve with each new pulse. Thus the importance density is a function of l and should adapt correspondingly to sample the evolving PPDs effectively. One solution is to employ a Gaussian mixture for the importance density. Let the importance density be given by [74,75]

$$x(\mathbf{m}; l) = \sum_{n=0}^{l} \beta_n x_n(\mathbf{m}), \tag{3.30}$$

where the mixture coefficients $\beta_n = Q_n/Q$, Q_n is the number of samples generated from the nth Gaussian density $x_n(\mathbf{m})$ and $Q = \sum_{n=0}^{l} Q_n$, and thus $\sum_{n=0}^{l} \beta_n = 1$.

Conventionally, Gaussian mixtures are used in adaptive importance sampling (AIS) to match the arbitrary and non-evolving PPD (in Bayesian applications) [74,75]. The mixture coefficients, means and covariance matrices of $x_n(\mathbf{m})$ are adaptively improved based on the previous Monte Carlo draws that sample the same PPD. In addition, the number of densities in the mixture remains constant. However, adapting the mixture coefficients β_n, means and variances of $x_n(\mathbf{m})$ is computationally demanding for each pulse measurement in the application discussed here. This is because each adaptive iteration requires hundreds or more forward model evaluations and many iterations are needed for the AIS density to converge to the current posterior density.

A simple alternative use of the Gaussian mixture that directly uses the posterior information is proposed here. The main difference between previous AIS implementations [74,75] and our proposed AIS is that the importance density here (Figs. 3.4 and 3.7) iteratively adapts as the PPD $p(\mathbf{m}|\mathbf{y}_{1:l})$ changes with l. The pseudo code for recursive Bayesian estimation using AIS is provided in Table 3.2. There are $l+1$ mixture components for a PPD conditioned on l measurements (see Eq. 3.30 and Fig. 3.4).

The initial density $x_0(\mathbf{m})$ is used in a preliminary exploration of $p(\mathbf{m}|\mathbf{y}_1)$. $x_0(\mathbf{m})$ is chosen to be a Gaussian density $\mathcal{N}((\mathbf{s}_u + \mathbf{s}_l)/2, \mathrm{diag}[(\mathbf{s}_u - \mathbf{s}_l)/2]^2)$, where $\mathbf{s}_u$ and $\mathbf{s}_l$ are upper and lower boundaries of the parameter search space. Using importance samples drawn from $x_0(\mathbf{m})$and the first pulse measurement, $\hat{\mathbf{m}}_{MAP}^{(1)}$ and the covariance matrix $\mathbf{C}_1$ of $\mathbf{m}$ can be approximated (see Eqs. (3.18), (3.19) and

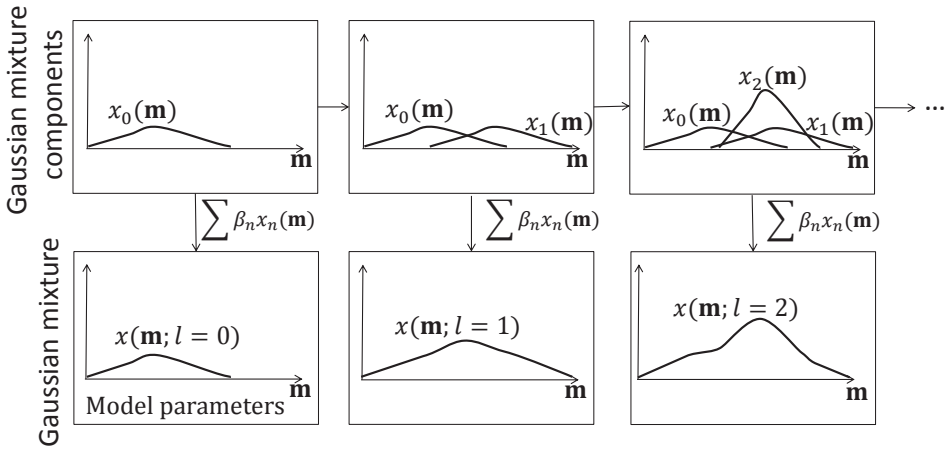

Figure 3.4: Importance density evolution with l.

(3.31)). While retaining the old importance samples for a new pulse, an additional set of importance samples is included using the density $x_1(\mathbf{m}) = \mathcal{N}(\hat{\mathbf{m}}_{MAP}^{(1)}, \mathbf{C}_1)$. Then, using $\sum_{j=0}^{1} Q_j$ importance samples from $x_0(\mathbf{m})$ and $x_1(\mathbf{m})$, $\hat{\mathbf{m}}_{MAP}^{(1)}$ and $\mathbf{C}_1$ can be updated.

It is important to note that both $\hat{\mathbf{m}}_{MAP}^{(l)}$ and $\mathbf{C}_l$ first are approximated from the PPD $p(\mathbf{m}|\mathbf{y}_{1:l})$ using the previous $\sum_{j=0}^{l-1} Q_j$ importance samples and the current pulse measurement embedded in the updated weights w_l^q. Subsequently, importance samples are drawn from $\mathcal{N}(\hat{\mathbf{m}}_{MAP}^{(l)}, \mathbf{C}_l)$ to sample the PPD $p(\mathbf{m}|\mathbf{y}_{1:l})$ more effectively. Then, using past and present importance samples $\sum_{j=0}^{l} Q_j$, $\hat{\mathbf{m}}_{MAP}^{(l)}$ and $\mathbf{C}_l$ can be updated. $\mathbf{C}_l$ is computed from (see Eqs. (3.18) – (3.19)) [71,73]

$$\mathbf{C}_l \approx \sum_{q=1}^{Q} (\mathbf{m}^q)(\mathbf{m}^q)^{\mathrm{T}} w_l^q - \boldsymbol{\mu}_l \boldsymbol{\mu}_l^{\mathrm{T}}. \tag{3.31}$$

The importance density now is dependent on l. The weight corrections (Eq. 3.26) should be applied after the weight recursion but before the weight normalization. Let un-corrected and un-normalized weights be redefined as $\hat{w}_l^q = p(\mathbf{y}_{1:l}|\mathbf{m}^q)p(\mathbf{m}^q)$ and the new recursion be $\hat{w}_l^q = p(\mathbf{y}_l|\mathbf{m}^q)\hat{w}_{l-1}^q$. The weights then are corrected by $\tilde{w}_l^q = \hat{w}_l^q / x(\mathbf{m}^q; l)$ before normalization. Importance sampling potentially can have numerical stability issues in the weight correction $\tilde{w}_l^q =$

$\hat{w}_l^q / x(\mathbf{m}^q; l)$ if $x(\mathbf{m}^q; l)$ is very small. Retaining the older densities in the mixture has the desirable effect of increasing the tails of the overall density while maintaining the main mass of samples in the high PPD region. [71,72]

The overall effect of this cumulative update of $\hat{\mathbf{m}}_{MAP}^{(l)}$ and $\mathbf{C}_l$, and accumulation of Gaussian densities is an AIS process. The last Gaussian density added will have a covariance that is an estimate of the covariance of the current PPD.

3.3 Recursive Bayesian Simulation

This section will demonstrate the recursive Bayesian estimation approach that coherently processes the data pulse-by-pulse and incrementally updates estimates of parameter uncertainty. It also approximates source/receiver radial acceleration by assuming piecewise constant but linearly changing source/receiver radial velocities. When source/receiver acceleration exists, it is demonstrated that modeling acceleration [Eqs. (3.5)–(3.11)] can further reduce the parameter estimation biases and uncertainties. The ocean model is illustrated in Fig. 3.1 and model parameters are tabulated in Table 3.3. Based on the theory presented in Sect. 2.2.1, this simulation models a constant velocity moving source that is slowing down radially with respect to the static receiver for $L = [1, \ldots, 64]$ pulses (see Fig. 3.3). The range-independent geoacoustic parameters were based on previous SW06 inversion results [26,53–56]. The source emits 100–900 Hz LFM pulses with 1 s pulse width and PRI. Thus, $v_{s64} = 1.52$ m/s. [see Eq. (3.9)]. The noise, Eq.(3.13), was generated to be similar to the measured power spectrum of SW06 ambient noise data. The frequency sampling is 5 Hz starting from 100 Hz–700 Hz. KRAKEN is used to compute the modes and wavenumbers [46].

The sediment parameters (ρ_{sed}, c_1, s, and α_{sed}) are estimated using the recursive Bayesian estimation procedure in Sect. 3.2.4, while the rest of the model parameters are assumed known. The parameter search space is kept small so that exhaustive-search based on 24^4 samples (instead of random importance samples) can be used to plot the true PPDs. Source acceleration is modeled in the replica field using Eq. (3.9). We first show that the method does indeed reduce the

parameter uncertainty as L increases. Using Eqs. (3.21), (3.22), (3.27) and (3.28), Fig. 3.5 shows both 1-D (along the diagonal) and 2-D (off-diagonal) marginal PPDs. In the 2-D PPDs, the densities are contoured according to their percentage highest posterior density (HPD) regions [35,52]. This percentage HPD is also equal to percentage of the total probability. The PPDs of the model parameters are not Gaussian. This is due to the non-linear relationship between the acoustic field and the geoacoustic parameters. Comparing the posterior densities in Figs. 3.5(a) and 3.5(b), the reduction in the HPD regions indicates that there is much improvement. The 2-D PPDs also provide information about the correlation between any two parameters.

Table 3.1: Assumptions for the forward model and inversion approach.

Waveguide Doppler model (see [26] and Sect. 2.2.1)
• Range independent environment
• Known source spectrum
• $\frac{v}{c} \ll 1$, source/receiver speed v is much less than the acoustic wave propagation speed c
• $\mathbf{v}_{sl}$ and $\mathbf{v}_{rl}$ are constant and horizontal
• Source-receiver displacement (due to motion) is much less than the source-receiver separation. Therefore, the radial velocities are approximately constant $v_{rl} = \lvert\mathbf{v}_{rl}\rvert \cos\varphi_{rl}, \quad v_{sl} = \lvert\mathbf{v}_{sl}\rvert \cos\varphi_{sl}$
• $\Psi(z;\omega) \approx \Psi(z;\omega_r) \approx \Psi(z;\omega_s)$
• Cutoffs or additions of modes due to Doppler shifts are neglected
• $k_{nl} \approx \frac{k_{rn}}{(1-\frac{v_{rl}}{u_{rn}})} \approx \frac{k_{sn}}{(1-\frac{v_{sl}}{u_{sn}})}$ where k_{nl} is approximated through Taylor's first order expansion
• Source/receiver acceleration is constant and much smaller than source/receiver speed
Recursive Bayesian inversion (see Sects. 3.2.2 and 3.2.3)
• Initial prior knowledge of the parameters
• Underlying model parameters are constant for all measurements

Table 3.2: Pseudo code for recursive Bayesian estimation using adaptive importance sampling.

Initial exploration of PPD $p(\mathbf{m}\|\mathbf{y}_1)$
Draw Q_0 samples $\{\mathbf{m}^1 \dots \mathbf{m}^{Q_0}\}$ from density
$x_0(\mathbf{m}) \sim \mathcal{N}((\mathbf{s}_u + \mathbf{s}_l)/2, \text{diag}[(\mathbf{s}_u - \mathbf{s}_l)/2]^2)$
Initialize weights $\hat{w}_0^q = p(\mathbf{m}^q)$
Recursive Bayesian Estimation
for $l = 1$ to L
Using current lth measurement $\mathbf{y}_l$ and the past importance samples $Q = \sum_{j=0}^{l-1} Q_j$:
Update weights $\hat{w}_l^q = p(\mathbf{y}_l\|\mathbf{m}^q)\hat{w}_{l-1}^q$
Correct weights $\tilde{w}_l^q = \hat{w}_l^q / x(\mathbf{m}^q; l-1)$
Normalize weights $w_l^q = \tilde{w}_l^q / \sum_{j=1}^{j=Q} \tilde{w}_l^j$
Using the $(l-1)$th importance density $x(\mathbf{m}; l-1)$
Approx. MAP estimate $\hat{\mathbf{m}}_{MAP}^{(l)}$ Eq. (3.18)
Approx. PPD Covariance $\mathbf{C}_l$ Eqs. (3.19, 3.31)
Draw Q_l importance samples from density $x_l(\mathbf{m}) \sim \mathcal{N}(\hat{\mathbf{m}}_{MAP}^{(l)}, \mathbf{C}_l)$.
For the new Q_l importance samples:
Compute weights $\hat{w}_l^q = p(\mathbf{m}^q) \prod_{j=1}^{l} p(\mathbf{y}_j\|\mathbf{m}^q)$
For all importance samples $Q = \sum_{j=0}^{l} Q_j$:
Correct weights $\tilde{w}_l^q = \hat{w}_l^q / x(\mathbf{m}^q; l)$
Normalize weights $w_l^q = \tilde{w}_l^q / \sum_{j=1}^{j=Q} \tilde{w}_l^j$
Bayesian statistical estimation for $\mathbf{y}_{1:l}$
Finalize MAP estimate $\hat{\mathbf{m}}_{MAP}^{(l)}$ Eq. (3.18)
Finalize Covariance PPD $\mathbf{C}_l$ Eqs. (3.19, 3.31)
Compute PPD estimate Eqs. (3.21, 3.22, 3.29)
Compute Bayesian inference Eqs.(3.23, 3.29)
endfor

Table 3.3: Baseline model parameters.

Simulation model parameters	value
Source range at $t = 0$, r_0 (m)	600
Source depth, z_{s1} (m)	30
Receiver depth, z_{r1} (m)	45
Source initial radial velocity, v_{s1} (m/s)	1.9
Receiver initial radial velocity, v_{r1} (m/s)	0
Source radial acceleration, a_s (mm/s^2)	-6
Receiver radial acceleration, a_r (mm/s^2)	0
Water depth, z_w (m)	78
Sediment depth, h_{sed} (m)	22
Sediment density, ρ_{sed} (g/cm^3)	1.8
Sediment attenuation., α_{sed} (dB/λ)	0.2
Sediment top velocity, c_1 (m/s)	1640
Sediment velocity slope, s (1/s)	0
Bottom density, ρ_{bot} (g/cm^3)	2.2
Bottom attenuation., α_{bot} (dB/λ)	0.2
Bottom velocity, c_b (m/s)	1740

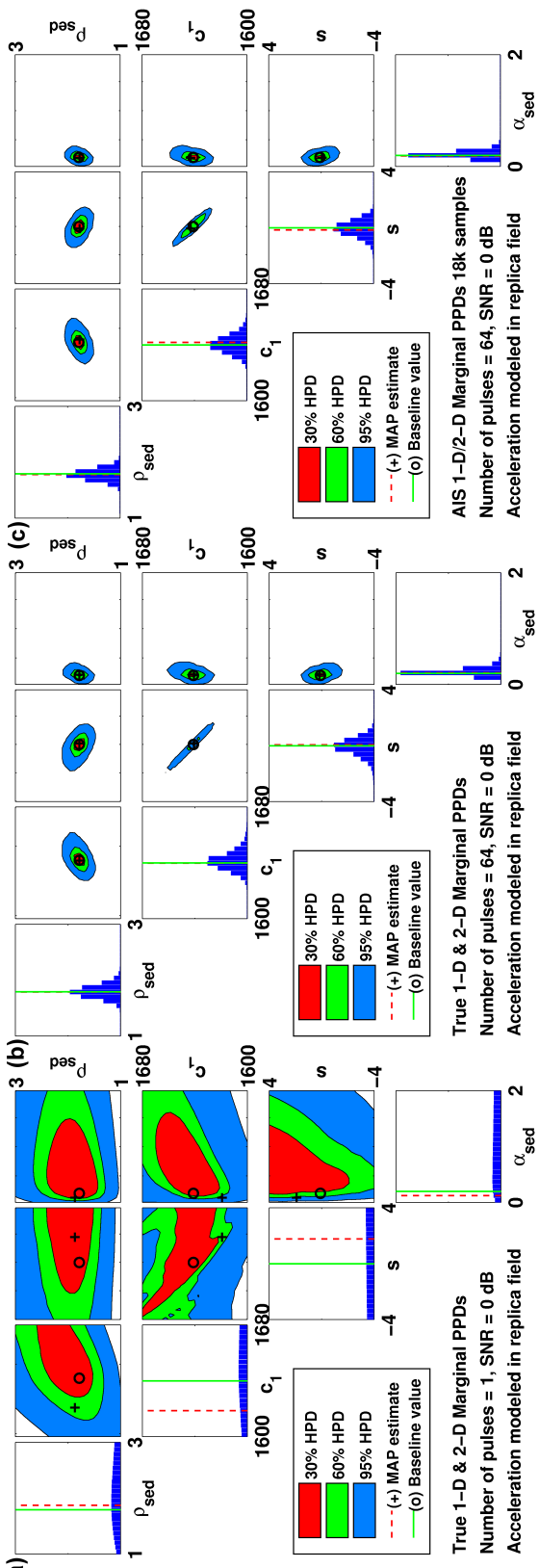

Figure 3.5: True marginal PPD via 24^4 exhaustive-search based samples with SNR fixed at 0 dB and number of LFM pulses (a) $L = 1$ (b) $L = 64$. (c) Estimated marginal PPD via AIS 18120 samples with SNR fixed at 0 dB and number of LFM pulses $L = 64$.

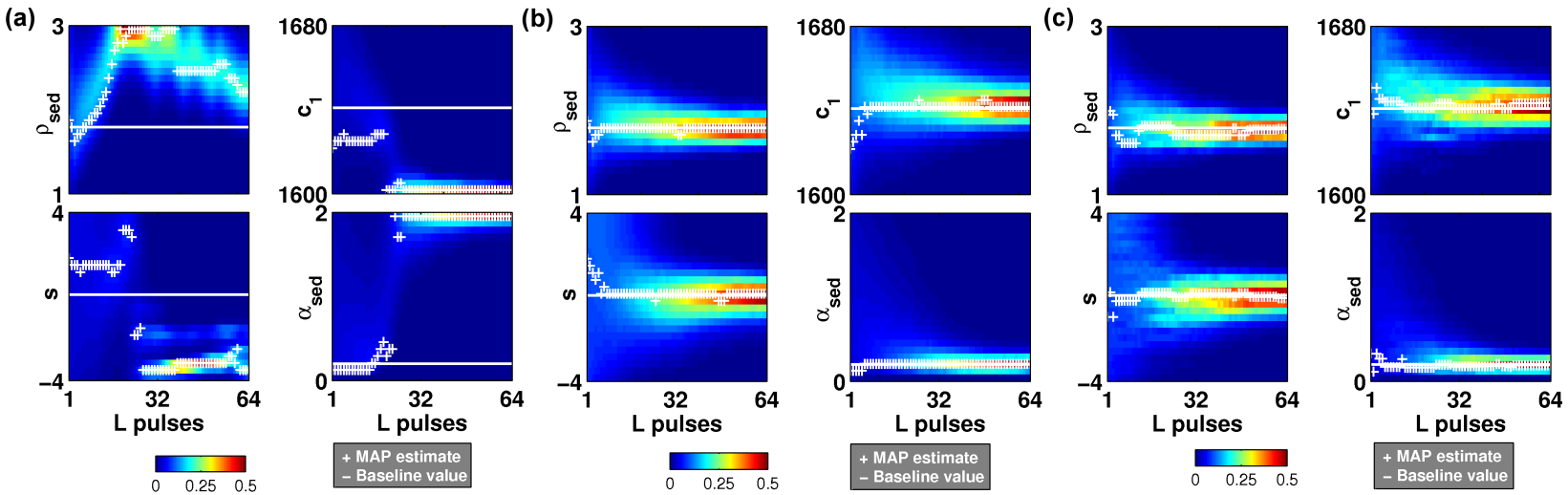

Figure 3.6: True 1-D marginal PPD evolution with $L = [1, \ldots, 64]$: (a) acceleration not modeled in the replica field (b) acceleration modeled in the replica field. (c) Estimated 1-D marginal PPD evolution with $L = [1, \ldots, 64]$ with acceleration modeled in the replica field and 3000–18120 AIS samples.

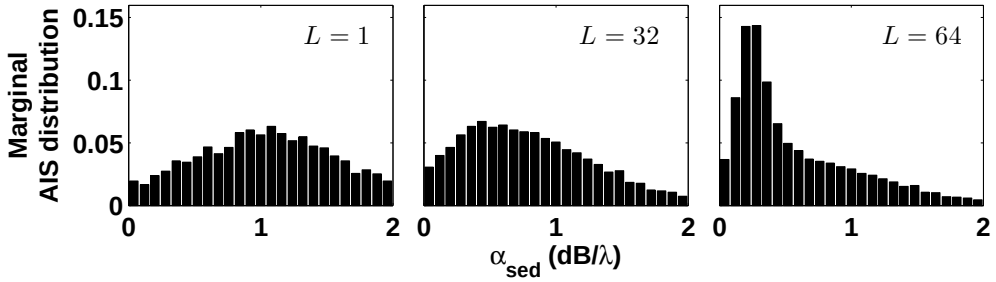

Figure 3.7: AIS importance distribution $x(\mathbf{m}; L)$ marginalized onto α_{sed} for $L = [1, 32, 64]$.

Recursive Bayesian estimation is repeated with no source acceleration modeled ($a_s = 0$ in Eq. (3.9)) in the replica field while the measured field contains $a_s = -0.006$ m/s. As the number of pulse measurements increases, the replica-to-measured field mismatch increases and the MAP and PPD estimation results deteriorate and deviate from the baseline values [see Fig. 3.6(a)]. This is due to the replica field not modeling pulse-number (l) dependent radial velocity changes. In addition, the importance sampling utilized in this recursive Bayesian formulation also will have difficulty sampling the high probability regions of parameter space since there is a range of possible radial velocities to match. As a result, the MAP estimates and 1-D marginal PPD plots in Fig. 3.6(a) were adversely affected and provided little or biased information about the geoacoustic properties.

On the other hand, if source acceleration is modeled in the replica field, the joint PPD of the model parameters will evolve and be more informative (peaky) as the number of pulse measurements increases, Eq. (3.16). Equivalently, this is observed in Fig. 3.6(b) in the evolution of the 1-D marginal PPDs with increasing number of pulse measurements.

Figs. 3.5(b) and 3.6(b) are repeated using the AIS approach starting with only 3000 samples that eventually grows to 18120 samples [see Figs. 3.5(c) and 3.6(c)]. Comparing Figs. 3.5(b) and (c), and 3.6(b) and (c), the AIS PPDs look similar to the true PPDs and they gradually will converge to the true PPD as more AIS samples are added. This has demonstrated that AIS is effective in estimating the PPD using 15 times less importance samples than the number used for the

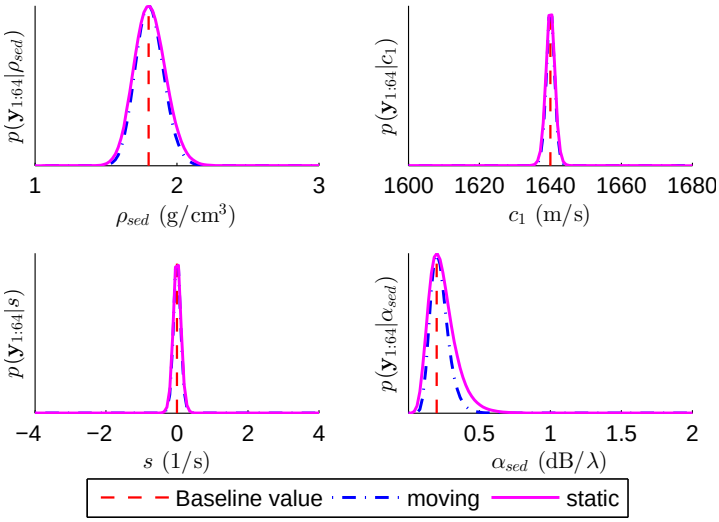

Figure 3.8: Likelihood function $p(\mathbf{y}_{1:64}|m_i)$ while fixing the remaining model parameters to the baseline value (see Table 3.3) for moving/static source-receiver configurations.

exhaustive sampling method. Fig. 3.7 shows how the AIS importance distribution $x(\mathbf{m}; L)$ adaptively changes with L to follow the evolving PPD.

These simulations have demonstrated the reduction of biases and uncertainty of parameter estimates as L increases. There are two contributions to this improvement. One is the coherent gain from processing multiple pulses. The other is the spatial gain when the source moves towards the receiver. A way to check the incremental contribution due to spatial gain is to carry out a parameter sensitivity analysis comparing static and moving source–receiver configurations for 64 pulses (see Fig. 3.8). As the synthetic aperture created in this simulation is short (109 m), the synthetic aperture/spatial gain is not significant compared to the gain from processing multiple pulses.

3.4 Experimental Data Analysis

The SW06 experiment was carried out near the shelf break on the New Jersey continental shelf from July to September 2006. The sequence of transmission in [26] do not have enough acceleration to demonstrate the effects of modeling

motion dynamics. Hence, a new sequence that is closer to the CPA was selected for analysis. The data set has a linearly changing radial velocity moving source and a static receiver over a range-independent track, see Figs. 3.9 and 3.10. The acoustic data were recorded on JD238 2040 coordinated universal time (UTC) ($t = 0$) from a 44.6 m deep single receiver (Channel 8) of a vertical line array (VLA1). The data set consisted of 64 LFM pulse (100–900 Hz) transmissions from a 29.5 m deep J–15 source towed by the R/V Knorr at an initial radial velocity of 1.6 m/s and radial acceleration of -0.006 m/s^2. The LFM pulse width was 1 s and was repeated every second. The initial R/V Knorr Global Positioning System (GPS) range to VLA1 was 525 m with a CPA distance of 410 m and the source is known to be trailing 115 m behind the ship's GPS mast. Based on the ship and VLA1 positions, the actual source to VLA1 distance at $t = 0$ is estimated to be 603 m. In addition, by factoring in that the source is trailing 115 m behind the GPS antenna, the actual radial velocity between source and VLA1 is 1.9 m/s. Correspondingly, the towed source displacement with respect to VLA1 or synthetic aperture is [1.9 m/s $-$ 64 s/2 $\times$ (0.006 m/s^2)]$\times$ 64 s = 109 m long.

The water depths measured at the source and receiver were 78 and 79 m, respectively. Water column SSPs are important and considered sensitive parameters in geoacoustic inversion. In the simulation, the SSP was assumed known to simplify and compute the true PPD. The true PPD confirms empirically that AIS in the inversion adequately samples the PPD (see Fig. 3.5). In the SW06 experimental data, the measured SSP is known to be range dependent and is not a good substitute for an averaged range independent SSP. In addition, due to the lack of conductivity, temperature and depth (CTD) measurements during this period and location, sound speed profile inversion was included using empirical orthogonal functions [53,54,61] (EOFs) based on SSPs derived from thermistors along the SHARK array (see Fig. 3.9) [26].

3.4.1 Data preprocessing and inversion results

Pre-processing of the single receiver data for all L pulses includes LFM pulse matched filtering for coarse synchronization. The data then are sliced according

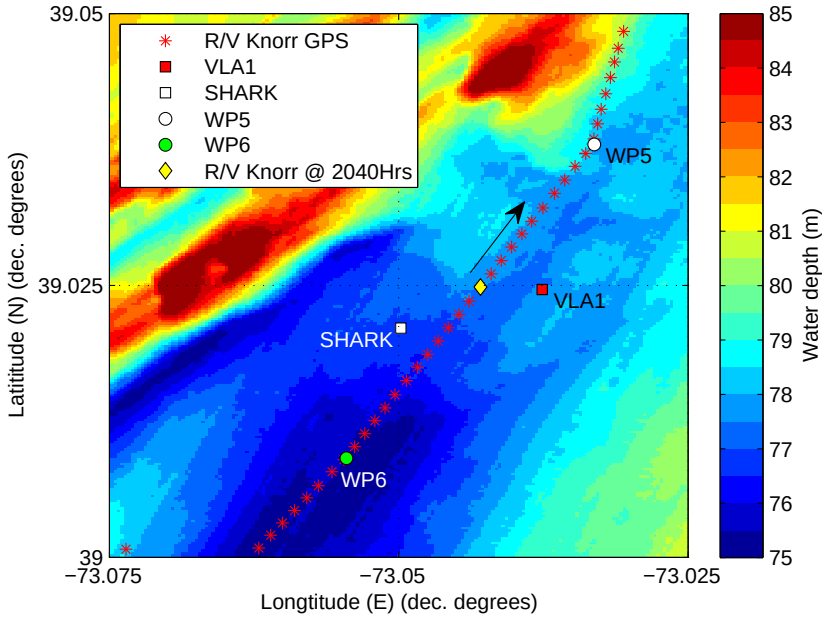

Figure 3.9: SW06 experiment site, bathymetry, source and receiver positions on JD238 (26 Aug 2006) 2000–2059 UTC.

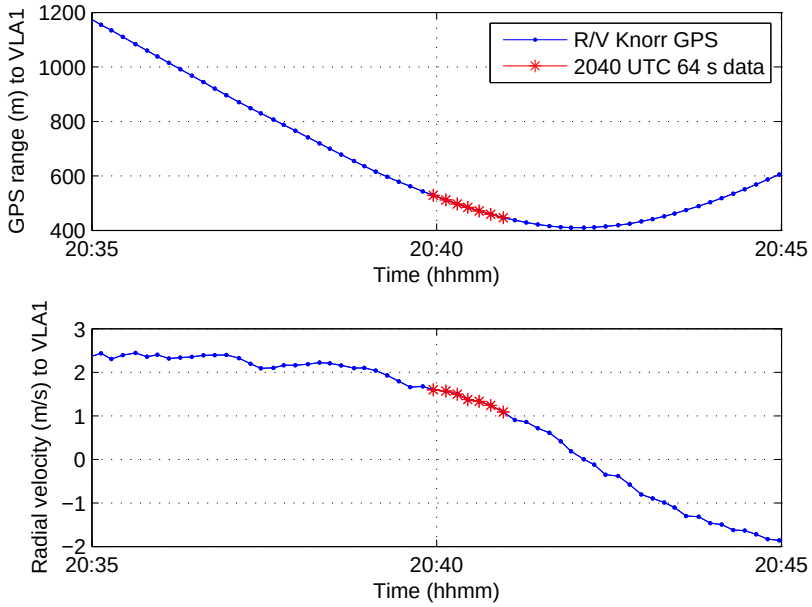

Figure 3.10: R/V Knorr range and radial velocity to VLA1. Highlighted is the period of time corresponding to the 64 s data analyzed.

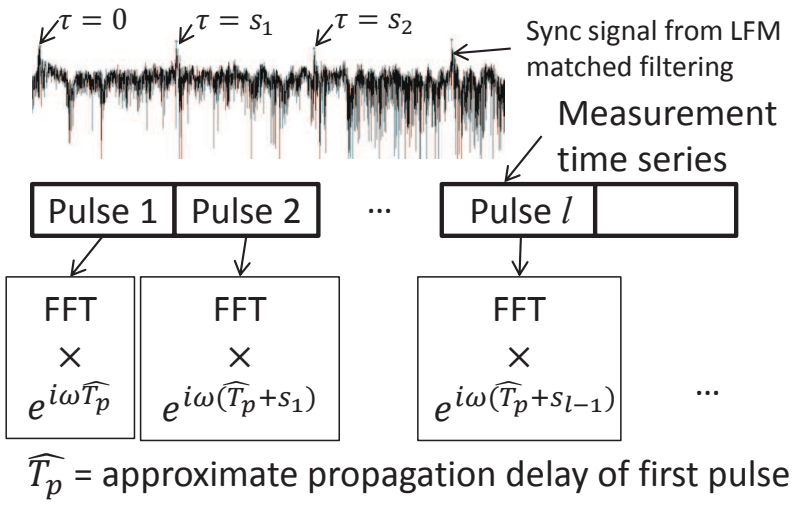

Figure 3.11: LFM pulse matched filtering for coarse synchronization.

to the synchronization and FFT'd to obtain the measured field $\mathbf{y}_l$ for each pulse in the frequency domain (see Fig. 3.11). The matched filter output are not used in the inversion itself. Finally, the frequency domain data are phase-adjusted according to the synchronization times such that coherent combination will follow Eq. (3.5). This makes the timing reference the same for all frequency domain data. For computational reasons, the frequency sampling interval is 5 Hz from 100 Hz to 700 Hz. As explained in [26] and in Section 2.2.1, the advantage of the waveguide Doppler model is that the forward model is computed on the receiver frequencies. To construct the replica field for a receiver frequency, the forward model has to trace backwards to multiple source frequencies due to mode-dependent Doppler shifts. This is done analytically using the backward frequency mapping in Eq. (3.7). The forward and backward mapping relationships between the source, propagation and receiver frequencies are provided in Table 3.4. [26]

The lower and upper bounds for the model parameters priors were set for the forward model depicted in Fig. 3.1 based on the background information at the experiment site [26,37,53–56], see Table 3.5. Importance samples are drawn from Gaussian mixtures and uniform priors are assumed. The 18-parameter recursive Bayesian inversion was done for $L = [1, \ldots, 64]$ using an initial 240,000

Table 3.4: Mapping relationships for the source, propagation and receiver frequencies.

Source	Propagation	Receiver
$\omega_s^{(k_{nl})} = \omega_r - k_{nl}(v_{sl} - v_{rl})$	$\omega = \omega_r + k_{nl} v_{rl}$	ω_r
ω_s	$\omega = \omega_s + k_{nl} v_{sl}$	$\omega_r^{(k_{nl})} = \omega_s + k_{nl}(v_{sl} - v_{rl})$

importance samples ($L = 1$) that eventually grows to 840,000 importance samples ($L = 64$). Note that a high number of importance samples is necessary for good PPD estimation [35]. On the other hand, MAP estimates require considerably fewer importance samples than required for PPD estimation [73].

Table 3.5 tabulates the inversion MAP results using waveguide Doppler without and with acceleration modeled for the 64 LFM pulses. For the inversion results using the acceleration model, the estimated sediment thickness, velocity and density are consistent with other published results [26,37,53–56] at the VLA1 site. For example, these inversion results range from 1600–1670 m/s for the top sediment velocity and 20–25 m for the sediment thickness. In addition, the geometric parameters ($r_0, z_s, z_r, v_{s1}, a_s$, and z_w,) results also agree very well with the measured or best known values. However, the gradient of the sediment velocity remains inconclusive. [37] There have been negative, zero and positive gradient sediment profile inversion results obtained by different investigators. The negative gradient sediment profile results here are similar to the results in Ref. [54].

The posterior densities of the model parameters are illustrated in Figs. 3.12−3.14, where only the 1-D (plots along the diagonal) and 2-D (plots above the diagonal) marginal PPDs are shown. Only the most relevant 11 or 12 out of 18 parameters are given in Figs. 3.12−3.14. The three EOF coefficients PPDs are difficult to interpret in terms of the water column SSP uncertainties. Therefore, the uncertainties or PPDs of the water column SSP, using Bayesian inference [Eq.(3.23)], are plotted from the PPD statistics of the EOF coefficients.

Table 3.5: SW06 data inversion parameters prior bounds and MAP results for $L = 64$.

Model parameters	Prior lwr.lim.	Prior upp.lim.	without a_s opt.	with a_s opt.
Src range at $t = 0$, r_0 (m)	520	630	550	594
Src depth, z_s (m)	27	32	28.8	29.7
Rcv depth, z_r (m)	39	46	41.0	42.6
Timing error, ξ (msec)	-50	50	9	-20
Src rad. vel., v_{s1} (m/s)	1.5	2.0	1.84	1.94
Src rad. accel., a_s (mm/s^2)	-7	-5	n/a	-6
EOF1 coef.	-50	50	22.5	42.3
EOF2 coef.	-20	20	6.6	14.0
EOF3 coef.	-10	10	0.9	5.2
Sed. thickness, h_{sed} (m)	10	30	20.5	21.5
Sed. dens., ρ_{sed} (g/cm^3)	1	3	2.5	2.1
Sed. attn., α_{sed} (dB/λ)	0.001	1	0.2	0.3
Sed. top. vel., c_1 (m/s)	1550	1700	1644	1655
Sed. vel. slope, s (1/s)	-10	10	-3.3	-4.3
Bot. vel., c_b (m/s)	1600	2200	1967	1993
Water depth, z_w (m)	74	81	74.2	76.9
Src level, α	0.1	0.8	0.2	0.5
Noise level, γ	0.5	1.9	1.5	1.1

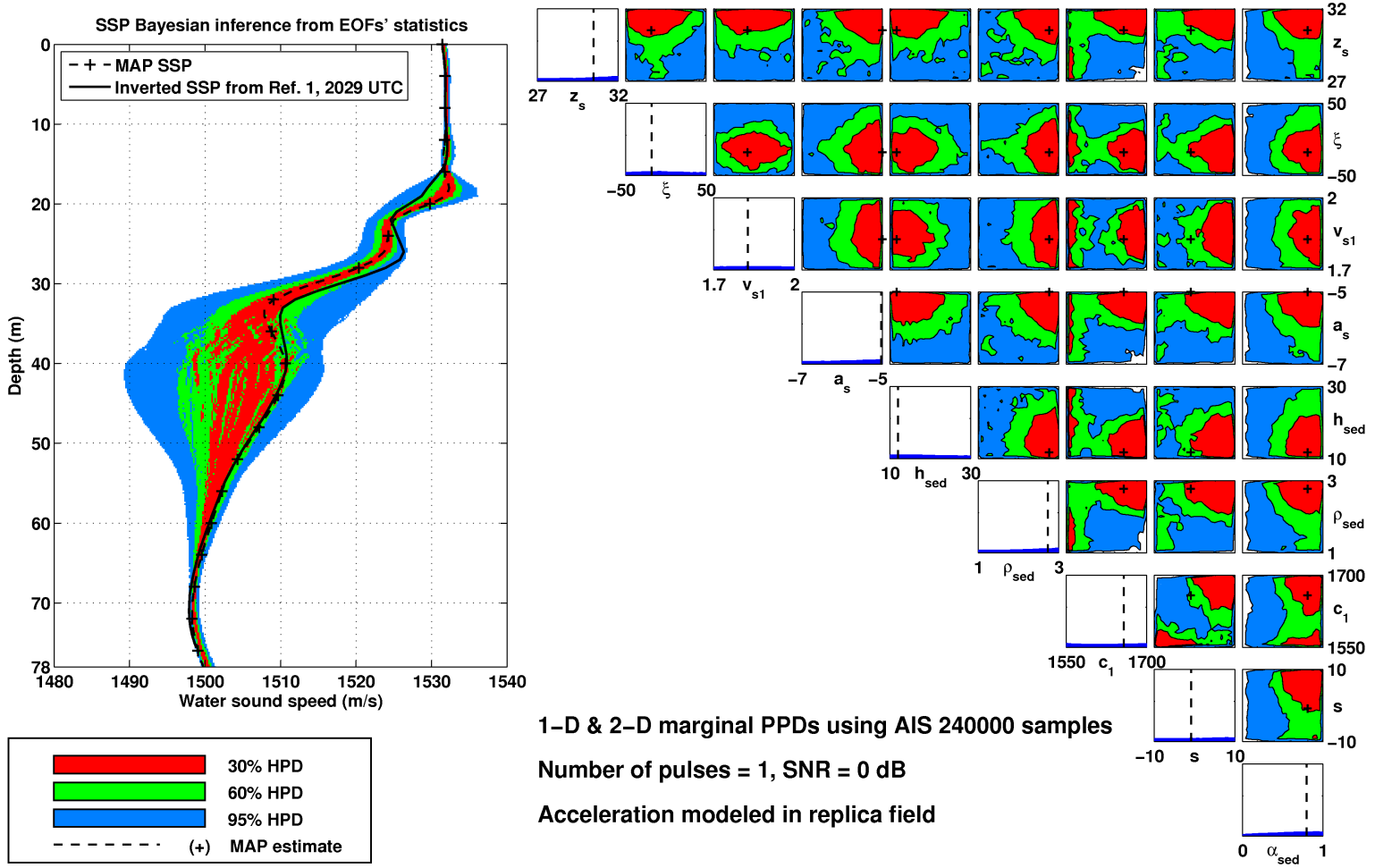

Figure 3.12: SW06 data recursive Bayesian inversion results using the waveguide Doppler model with acceleration modeled in the replica for $L = 1$.

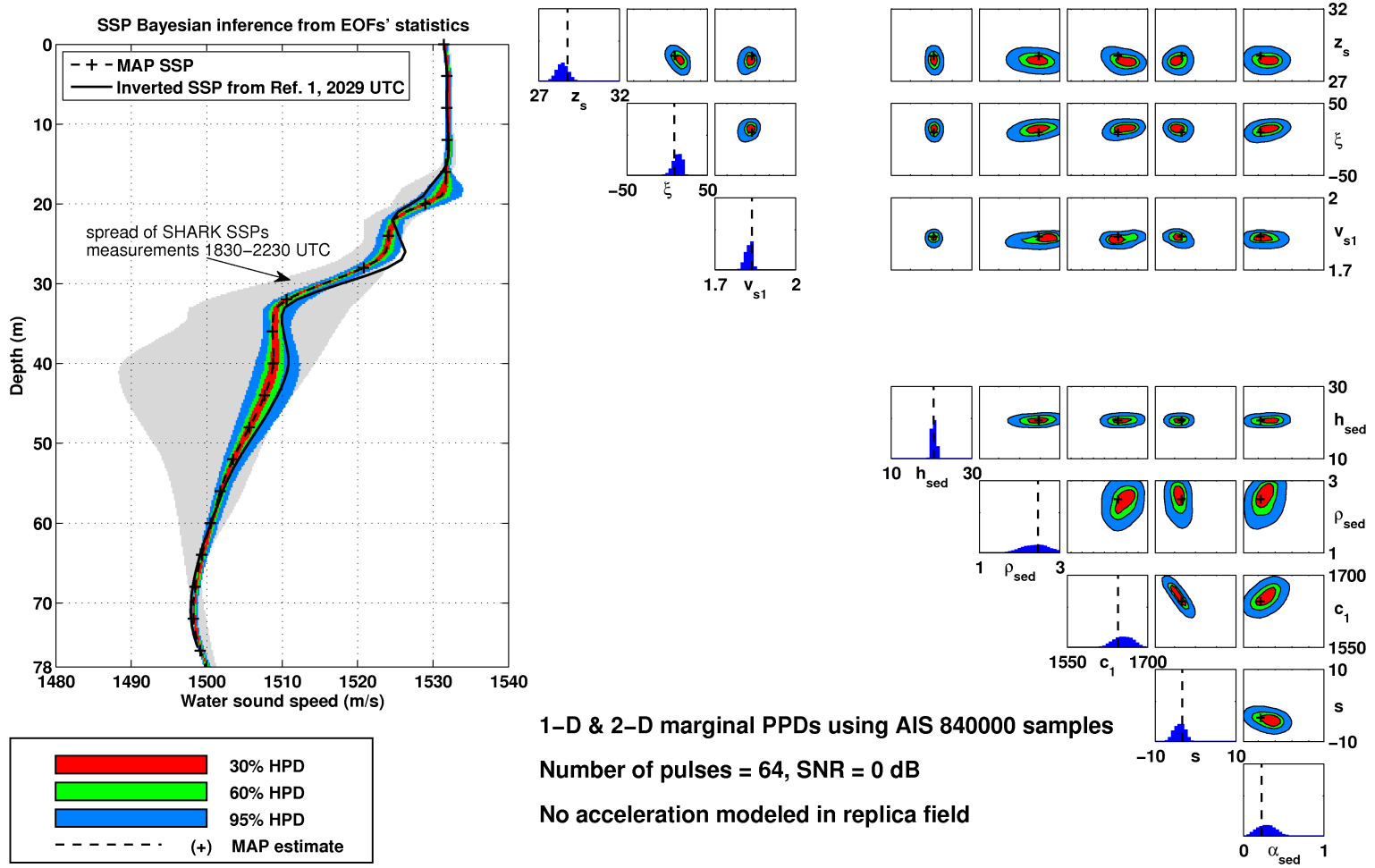

Figure 3.13: SW06 data recursive Bayesian inversion results using the waveguide Doppler model with no acceleration modeled in the replica for $L = 64$.

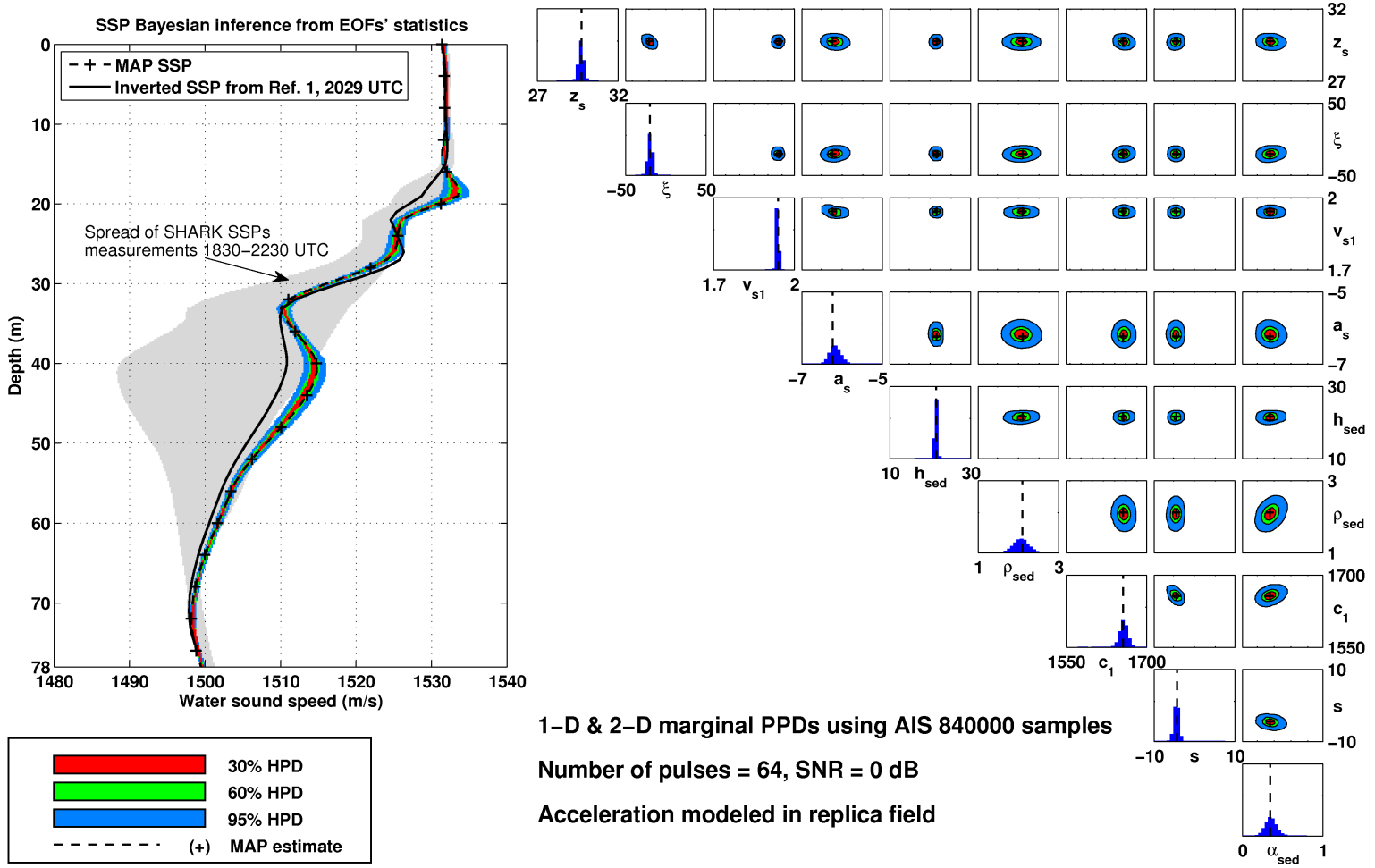

Figure 3.14: SW06 data recursive Bayesian inversion results using the waveguide Doppler model with acceleration modeled in the replica for $L = 64$.

Comparing Figs. 3.12 and 3.14, the reduction in uncertainties between $L = 1$ and $L = 64$ is remarkably good across all parameters. Uncertainty reduction in the water column SSP also is observed (see Figs. 3.12 and 3.14). The largest uncertainty in the water column SSP is between 35–45 m depth. This compares well to the SHARK SSP measurements between 1830–2229 UTC where the largest sound speed variation is around 40 m depth (see Fig. 3.14). Because the SSPs are known to be range dependent in SW06, the SHARK SSP measured at 2040 UTC was not a good substitute for an averaged range independent SSP. The EOFs have enabled the inversion to optimize for the best average SSP and the SSP inverted here is consistent with the SSP inversion results from [26].

In contrast, the MAP results in Table 3.5 for $L = 64$ without using the acceleration model yield more biased geometric and geophysical (r_0, z_s, z_r, z_w, and ρ_{sed}) results when compared to measured or best known values. The biased geometric results are an indication that this inversion is not reliable. For example, the source range r_0 is 50 m short and the water, source and receiver depths, are respectively, 4.8 m, 1.2 m and 3.6 m too shallow. These differences cannot be explained by the effective parameter calculations for a mildly range dependent environment. [76] This further is supported by the parameter estimation uncertainties or the 95% HPD region results when not using acceleration which are about 100% more than the results when using the acceleration model (compare Figs. 3.13 and 3.14). The inverted water column velocity profile also is different than the results when using the acceleration model. Thus, the quality of the inversion results without modeling acceleration is lower than that with acceleration modeled.

3.5 Conclusions

A broadband, frequency coherent matched-field inversion procedure for a moving source and receiver at low SNR using a recursive Bayesian pulse-by-pulse approach has been developed. This enabled a time-evolving uncertainty analysis of the model parameters and an approximation for a horizontally accelerating source and receiver. Through simulation and data analysis from the Shallow Water

2006 experiment, it was demonstrated that: (1) via online uncertainty analysis, parameter uncertainty reduces with an increasing number of pulses and (2) when source/receiver acceleration exists, modeling acceleration in the inversion can reduce further parameter estimation biases and uncertainties.

Acknowledgments

This work was supported by the Office of Naval Research Grant No. N00014-11-0320 and the DSO National Laboratories of Singapore. Chapter 3, in full, is a reprint of material in the Journal of Acoustical Society of America as: B.A. Tan, P. Gerstoft, C. Yardim, W. Hodgkiss, "Recursive Bayesian synthetic aperture geoacoustic inversion in the presence of motion dynamics", *J. Acoust. Soc. Am.*, in press, 2014. The dissertation author was the primary investigator and author of this paper.

Chapter 4

Change-point detection for recursive Bayesian geoacoustic inversions

4.1 Introduction

A recursive Bayesian synthetic aperture geoacoustic inversion method previously has been developed for single source/receiver mobile scenarios in low signal to noise ratio (SNR) conditions. It involves long-time coherent integration of multiple broadband pulses, recasting dynamic time-varying geometric model parameters into initial-value and constant parameters via a trajectory-based waveguide Doppler normal mode model and assumes constant underlying model parameters. [26,77]

Because of the long-time coherent integration and source-receiver motion, change in the underlying model parameters due to time or space is anticipated. Here, abrupt and gradual change in the underlying model parameters are considered. Methods for detecting abrupt model parameter change are well established and consist of offline/retrospective [38,39] and online change-point methods [40–43].

A change-point is defined as a time when the model parameters have changed.

Refs. [40,41] independently have proposed an online version of the Bayesian change-point detection method. It calculates the posterior probability density of the change-point at each time step. There is also the particle filtering approach in Bayesian online change detection in Refs. [40,42,43], with the last reference being applied to joint change-point detection and parameter estimation. However, a majority of the change-point detection approaches either treat the auxiliary model parameters (parameters not under test) as known or as nuisance parameters that eventually will be integrated out analytically, for example Refs. [39–42].

To conveniently integrate out nuisance parameters, most approaches usually assume conjugate-exponential models which inadvertently exclude geoacoustic inversion models due to their non-linear relationship between model parameters and measurements. A conjugate-exponential model solution to joint detection of change-point and parameter estimation is proposed in [43]. It does recursive maximum likelihood model parameter estimation which involves computing the Hessian using the Newton stochastic gradient algorithm.

Due to the low SNR nature of the observations and the non-conjugate-exponential model of the geoacoustic inversion application, offline/retrospective methods [38,39] are selected for detecting change-points here. Coincidentally, detecting a change-point can be done using the importance samples and corresponding weights that already are available from the recursive Bayesian inversion developed in Chapter 3 or Ref. [77]. When a change-point is detected, the current inversion concludes and a new inversion is started using post-change-point measurements.

Methods for detecting gradual model parameter change are less developed and often require strong parametric assumption. For example, time varying source/receiver geometric parameters are reparameterized into initial range, velocity and acceleration [26,77]. However, such reparameterization is done at the expense of increasing the parameter search dimension. Reparameterizing all the model parameters in the inversion will adversely increase the parameter search dimensions. Alternatively, the change-point method for abrupt change is used for the gradual change case. If the model parameters change gradually, the inver-

sion (based on constant model parameters) may proceed to estimate an average value of the parameters until the accumulated model parameter mismatch error is significant and triggers the detection of a change-point.

These change-point detections form the heuristics for controlling the coherent integration time in recursive Bayesian inversion. The method is demonstrated in simulation with parameters corresponding to the low SNR, 100–900 Hz LFM pulses observed in the Shallow Water 2006 experiment.

4.2 Theory

4.2.1 Change-point detection

Change-point models commonly are used to model discontinuity of model parameters or data over the length of the data. Given a sequence of observations, these models introduce a number of change-points which split the data into a set of disjoint segments. It then is assumed that the data arise from a single model within each segment but with different models across the segments. For the recursive Bayesian inversion approach described in Chapter 3 [77], the probability distributions (importance samples and weights) that are generated for model parameter estimates also can be used for inferences about the possible change-points.

We consider the following class of single change-point model [38]. Let the sequence of non-overlapping measurement vectors be $\mathbf{y}_{1:L} = [\mathbf{y}_1^{\mathrm{T}}, \ldots, \mathbf{y}_L^{\mathrm{T}}]^{\mathrm{T}}$ where the data propagation model, and likelihood function are based on Chapter 3 or Ref. [77]. Each measurement vector is independent and identically distributed (i.i.d.) with likelihood $p(\mathbf{y}|\mathbf{m})$. This sequence of measurements is assumed to have a change-point at r $(1 \leqslant r \leqslant l)$ where $\mathbf{y}_l \sim p(\mathbf{y}_l|\mathbf{m}_1)$ $\forall$ $l = 1, \ldots, r$ and $\mathbf{y}_l \sim p(\mathbf{y}_l|\mathbf{m}_2)$ $\forall$ $l = r+1, \ldots, L$.

$$\mathbf{y}_l = \begin{cases} \mathbf{b}_l(\mathbf{m}_1) + \mathbf{w}_l, & \text{if } l = 1, \ldots, r. \\ \mathbf{b}_l(\mathbf{m}_2) + \mathbf{w}_l, & \text{if } l = r+1, \ldots, L. \end{cases} \tag{4.1}$$

$\mathbf{m}$ and $\mathbf{w}_l$ are the model parameters and noise respectively and $\mathbf{b}_l(\mathbf{m})$ is the transformation of the model parameters into the signal observed in the data

$\mathbf{y}_l$. The objective is to determine the posterior distribution of the change-point r via the Bayesian approach.

The joint likelihood of the $\mathbf{y}_{1:L}$ conditioned on $\mathbf{m}_1$ and $\mathbf{m}_2$ is [38]

$$\begin{aligned} p(\mathbf{y}_{1:L}|r,\mathbf{m}_1,\mathbf{m}_2) &= p(\mathbf{y}_{1:r}|\mathbf{m}_1)p(\mathbf{y}_{r+1:L}|\mathbf{m}_2) \\ &= \prod_{l=1}^{r} p(\mathbf{y}_l|\mathbf{m}_1) \prod_{l=r+1}^{L} p(\mathbf{y}_l|\mathbf{m}_2) \end{aligned} \tag{4.2}$$

The change-point is assumed to have prior density $p(r)$ such that $\sum_{r=1}^{L} p(r) = 1$. Using Bayes rule, the posterior probability distribution (PPD) of the possible change-points, conditioned on all the measurements, is [38]

$$p(r|\mathbf{y}_{1:L}) \propto p(\mathbf{y}_{1:L}|r)p(r) \tag{4.3}$$

where

$$\begin{aligned} p(\mathbf{y}_{1:L}|r) &= \int p(\mathbf{y}_{1:L}|r,\mathbf{m}_1,\mathbf{m}_2)p(\mathbf{m}_1,\mathbf{m}_2)\mathrm{d}\mathbf{m}_1\mathrm{d}\mathbf{m}_2 \\ &= \int p(\mathbf{y}_{1:r}|r,\mathbf{m}_1)p(\mathbf{m}_1)\mathrm{d}\mathbf{m}_1 \\ &\times \int p(\mathbf{y}_{r+1:L}|r,\mathbf{m}_2)p(\mathbf{m}_2)\mathrm{d}\mathbf{m}_2 \end{aligned} \tag{4.4}$$

It also is assumed that the model parameters before and after the change-point are independent. [40,41] Eqs. (4.3) and (4.4) can be evaluated via Monte Carlo integration using the importance samples from the recursive Bayesian inversion in Chapter 3 or Ref. [77].

Here, we further assumed uniform priors for the change-point, the maximum likelihood estimate of the change-point is

$$\hat{r} = \arg\max_{r} p(\mathbf{y}_{1:r}|\hat{\mathbf{m}}_{1,r})p(\mathbf{y}_{r+1:L}|\hat{\mathbf{m}}_{2,r}). \tag{4.5}$$

where

$$\hat{\mathbf{m}}_{1,r} = \arg\max_{\mathbf{m}} p(\mathbf{m}|\mathbf{y}_{1:r}), \tag{4.6}$$

and

$$\hat{\mathbf{m}}_{2,r} = \arg\max_{\mathbf{m}} p(\mathbf{m}|\mathbf{y}_{r+1:L}). \tag{4.7}$$

are the maximum a posteriori (MAP) estimates of the model parameters $\mathbf{m}_1$ and $\mathbf{m}_2$ conditioned on the measurements prior to and after the hypothesize change-point r, respectively. Eq.(4.5) works only if a model parameter change-point is present in the measurements. If there is no underlying model parameter change-point in the measurements collected, then Eq.(4.5) will be equally likely for all hypotheses r. To determine the presence of a change-point, a normalized log-likelihood

$$\mathcal{L}(r) = 10\log_{10}\frac{p(\mathbf{y}_{1:r}|\hat{\mathbf{m}}_{1,r})p(\mathbf{y}_{r+1:L}|\hat{\mathbf{m}}_{2,r})}{\max\limits_{r} p(\mathbf{y}_{1:r}|\hat{\mathbf{m}}_{1,r})p(\mathbf{y}_{r+1:L}|\hat{\mathbf{m}}_{2,r})}. \tag{4.8}$$

is used and if $\max\mathcal{L}(r) - \min\mathcal{L}(r) \geqslant \beta$ then a change-point is detected. β is a threshold determined by trial and error. β is set to 10 dB which means a change-point is detected if the maximum likelihood is ten times higher than the minimum likelihood.

In Chapter 3 or Ref. [77], the importance samples and their associated uncorrected and un-normalized weights $\{\mathbf{m}^q, \hat{w}_l^q\}$ where $\hat{w}_l^q = p(\mathbf{y}_{1:l}|\tilde{\mathbf{m}}^q)p(\tilde{\mathbf{m}}^q)$ were computed recursively using $\hat{w}_l^q = p(\mathbf{y}_l|\tilde{\mathbf{m}}^q)\hat{w}_{l-1}^q$. Note that $\mathbf{m}^q$ are drawn from a Gaussian mixture as describe in Sect. 3.2.5. Using these weights, the posterior density is obtained from

$$p(\mathbf{m}|\mathbf{y}_{1:r}) \approx \sum_{q=1}^{Q} \delta(\mathbf{m}-\mathbf{m}^q)\frac{\hat{w}_r^q}{x(\mathbf{m}^q;L)}, \tag{4.9}$$

and

$$p(\mathbf{m}|\mathbf{y}_{r+1:L}) \approx \sum_{q=1}^{Q} \delta(\mathbf{m}-\mathbf{m}^q)\frac{\hat{w}_L^q p(\mathbf{m}^q)}{\hat{w}_r^q x(\mathbf{m}^q;L)}, \tag{4.10}$$

where the weights $\hat{w}_l^q$ corresponds to the $Q = \sum_{j=0}^{L} Q_j$ importance samples described in Ref. [77].

The likelihoods are also inferred using the weights in the recursive Bayesian inversion from

$$p(\mathbf{y}_{1:r}|r,\mathbf{m}^q) = \frac{\hat{w}_r^q}{p(\mathbf{m}^q)} \tag{4.11}$$

and

$$p(\mathbf{y}_{r+1:L}|r,\mathbf{m}^q) = \frac{\hat{w}_L^q}{\hat{w}_r^q}. \tag{4.12}$$

Therefore, change-point detection computationally is convenient when used with the recursive Bayesian inversion described in Ref. [77]. By re-using the weights from the recursive Bayesian inversion, there is no need to recompute likelihoods and posterior density explicitly.

4.3 Simulation

This section will demonstrate change-point detection in abrupt and gradual model parameter change. Upon detection, the current recursive Bayesian inversion will conclude and a new inversion will begin. The ocean model is illustrated in Fig. 4.1 and model parameters are tabulated in Table 4.1. Based on the theory presented in Sect. 4.2 and Ref. [77], this simulation models a source and receiver moving in the same direction as the horizontal axis r_x and at the same speed for $L = [1, \ldots, 128]$ pulses (see Fig. 4.2). The source and receiver are assume to be seperated in distance by r_{0l} in the direction r_y as depicted in Fig. 4.2. Hence, the radial velocities are equal to zero. The environment is assume range independent across the source and receiver while range dependent along the source or receiver track. The range-independent geoacoustic parameters were based on previous SW06 inversion results [26,53–56,77]. The source emits 100–900 Hz LFM pulses with 1 s pulse width and PRI. The noise, as per in Ref. [77], was generated to be similar to the measured power spectrum of SW06 ambient noise data. The frequency sampling is 5 Hz starting from 100 Hz–700 Hz. KRAKEN is used to compute the modes and wavenumbers [46].

In Fig. 4.3, the objective is to simulate and detect an abrupt change in the sediment thickness along the track in recursive Bayesian inversion. The true sediment thickness H_{sed} is fixed at 22 m for $l = 1$ to $l = 64$ and then fixed at 17 m for $l = 65$ to $l = 128$ to simulate an abrupt change in sediment thickness H_{sed}. The sediment parameters (H_{sed}, c_1, s, and α_{sed}) are estimated using the recursive Bayesian estimation procedure in Ref. [77], while the rest of the model parameters are assumed known. In addition, the weights from the inversion are being used for change-point detection detailed in Sect. 4.2. In Fig. 4.3, only the

Table 4.1: Baseline model parameters.

Simulation model parameters	value
Source range at $t = 0$, r_0 (m)	600
Source depth, z_{s1} (m)	30
Receiver depth, z_{r1} (m)	45
Source initial radial velocity, v_{s1} (m/s)	0
Receiver initial radial velocity, v_{r1} (m/s)	0
Source radial acceleration, a_s (mm/s^2)	0
Receiver radial acceleration, a_r (mm/s^2)	0
Water depth, z_w (m)	78
Sediment depth, h_{sed} (m)	22
Sediment density, ρ_{sed} (g/cm^3)	1.8
Sediment attenuation., α_{sed} (dB/λ)	0.2
Sediment top velocity, c_1 (m/s)	1640
Sediment velocity slope, s (1/s)	0
Bottom density, ρ_{bot} (g/cm^3)	2.2
Bottom attenuation., α_{bot} (dB/λ)	0.2
Bottom velocity, c_b (m/s)	1740

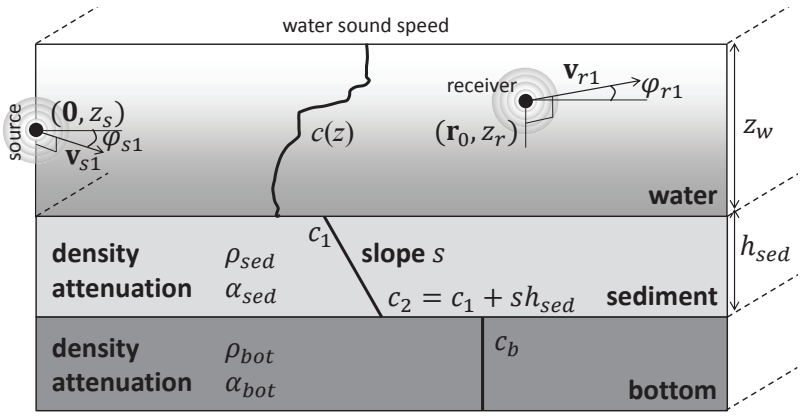

Figure 4.1: Horizontally stratified ocean with a horizontally moving source and receiver. The source is moving at initial velocity $\mathbf{v}_{s1}$ and bearing φ_{s1} while the receiver is moving at initial velocity $\mathbf{v}_{r1}$ and bearing φ_{r1}. The range origin is the source position at time zero when the source begins transmitting.

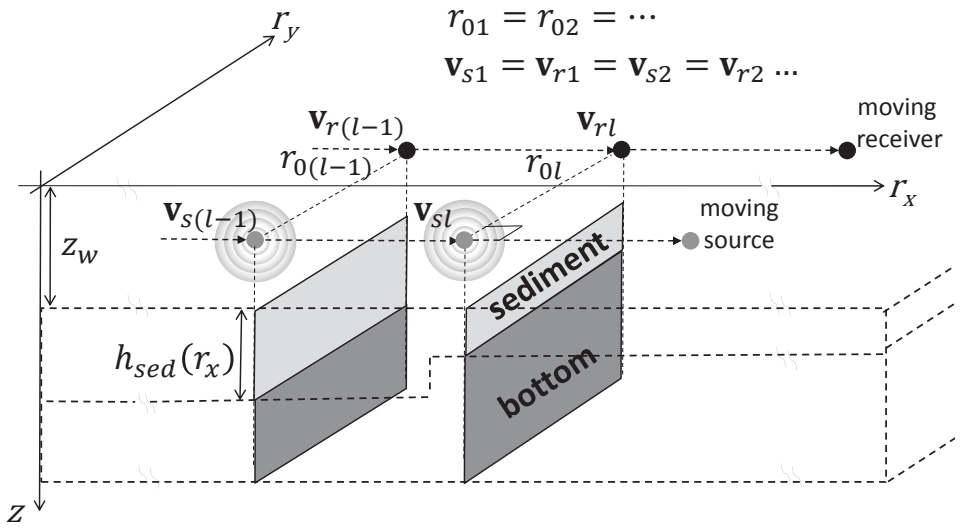

Figure 4.2: r_x and r_y are the horizontal axes where the origin is the source position at time zero when the source begins transmitting. Source and receiver are moving in the same r_x direction and at the same speed. The source-receiver separation is constant and the geoacoustic properties are assume range-independent in the r_y direction. Shown above are the source and receiver positions just prior and after the abrupt change in sediment thickness.

95% highest posterior density (HPD) regions [35,52] of the 1-D marginal PPD and MAP parameter estimates for each model parameter are reconstructed based on

$L - r$ pulses measurements where r is the most recent change-point. The change-point is detected correctly at $r = 64$ and the current inversion concludes based on $l = 1 : r$ pulses measurements. A new inversion is started using post-change-point $r+1$th pulse measurement onwards and hence the sudden increase in uncertainties at $L = 64$.

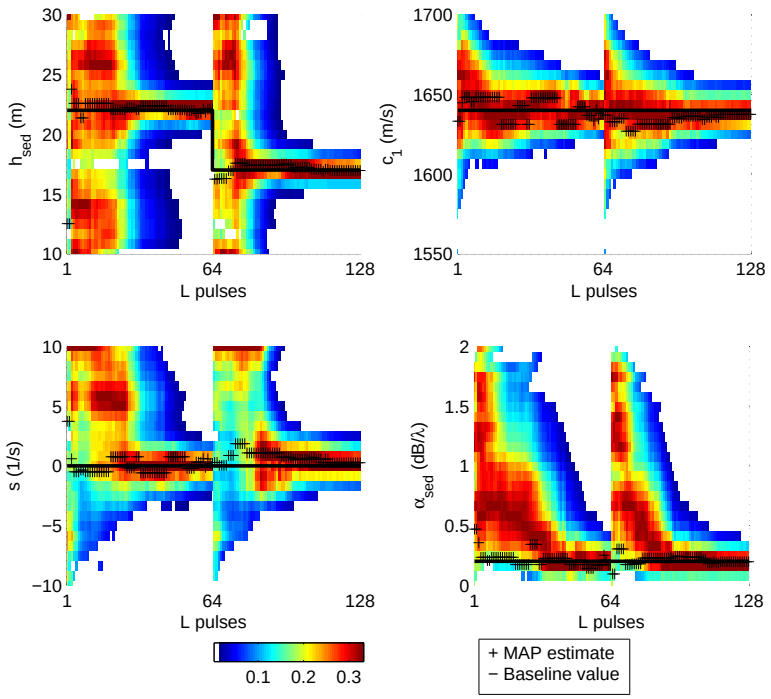

Figure 4.3: Evolution of 1-D marginal PPD with SNR fixed at 0 dB, and number of LFM pulses $L = 1$ to 128 with change-point detected at $r = 64$. Only the 95% HPD portion (non-white) PPD is plotted. When a change-point is detected, the inversion restarts and the post-change-point PPD and MAP estimates are based on $L - r$ pulses measurement where r is the most recent change-point.

Not shown in Fig. 4.3 is the number of post-change-point measurements needed for a change-point to be detected retrospectively. In Fig. 4.4, the time-evolving change-point log-likelihood $\mathcal{L}(r)$ is plotted for $L = 1$ to 71. It is noted the change-point log-likelihood is equally likely when a change-point is absent ($L < 64$). However, when a change-point is present, a peak at $r = 64$ emerges as more post-change-point measurements are collected. Finally, a change-point is

detected at $r = 64$ when $L = 71$ (threshold $\beta = 10$ dB). At this stage, only the pre-change-point importance samples are retained, while the post-change-point importance samples are discarded. Note that a change-point detection will not indicate which particular model parameters have changed. A potential extension of this method would be to determine which parameters have changed upon change-point detection and then use the posterior information from the pre-change-point inversion to assign an appropriate prior density to the post-change-point inversion.

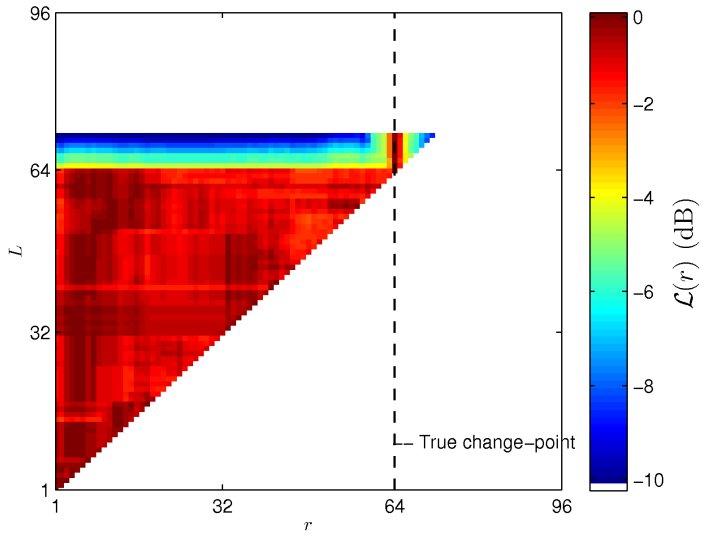

Figure 4.4: Evolution of change-point likelihood L with SNR fixed at 0 dB, and number of LFM pulses $L = 1$ to 71 with change-point detected ($\beta = 10$ dB) at $r = 64$ and $L = 71$.

The simulation is repeated with no change-point detection. Hence, the inversion (based on constant model parameters) is allowed to proceed despite an abrupt change in the sediment thickness at $L = 64$. (see Fig. 4.5). Due to the model mismatch error, the inversion results for $L > 64$ are biased (see h_{sed} and α_{sed}).

Next, a gradual change (from 22 m to 17 m) in the sediment thickness is simulated (see Figs. 4.6 and 4.7). When the accumulated model mismatched error is significant, a change-point detection is triggered. Here, two change-points have been triggered at $L = 41$ and $L = 71$. Despite the model mismatch in

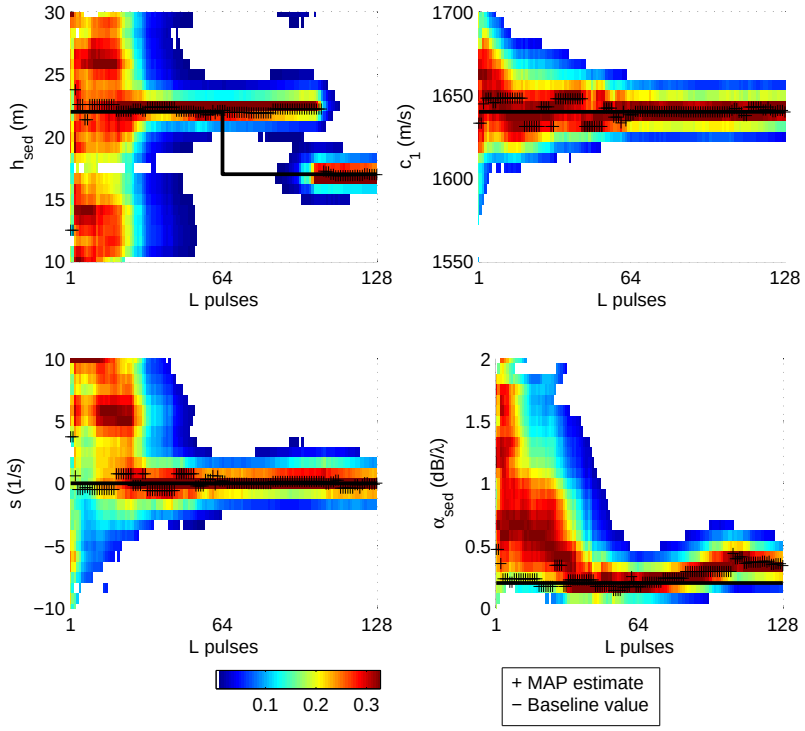

Figure 4.5: Evolution of 1-D marginal PPD with SNR fixed at 0 dB, and number of LFM pulses $L = 1$ to 128 without change-point detection. The inversion (based on constant model parameters) is allowed to proceed despite an abrupt change at $L = 64$ in the sediment thickness. Only the 95% HPD portion (non-white) PPD is plotted.

fitting a constant parameter model to a gradual change parameter model, there is no significant bias in the MAP estimates. The MAP estimates for the sediment thickness converge to an average value between the minimum and maximum value for each segment. Here, the gradually changing parameter model is segmented via the change-point detection method into three models, each with a different set of constant parameters.

Fig. 4.8 shows the time-evolving change-point log-likelihood $\mathcal{L}(r)$ for the $L = 1$ to 63. There are two difference when comparing Figs. 4.5 and 4.8. First, the change-point likelihood is less peaky across r in the gradual change case. This is expected as the method is designed for abrupt/non-gradual parameter change. Second, the number of post-change-point measurements is comparable to the number

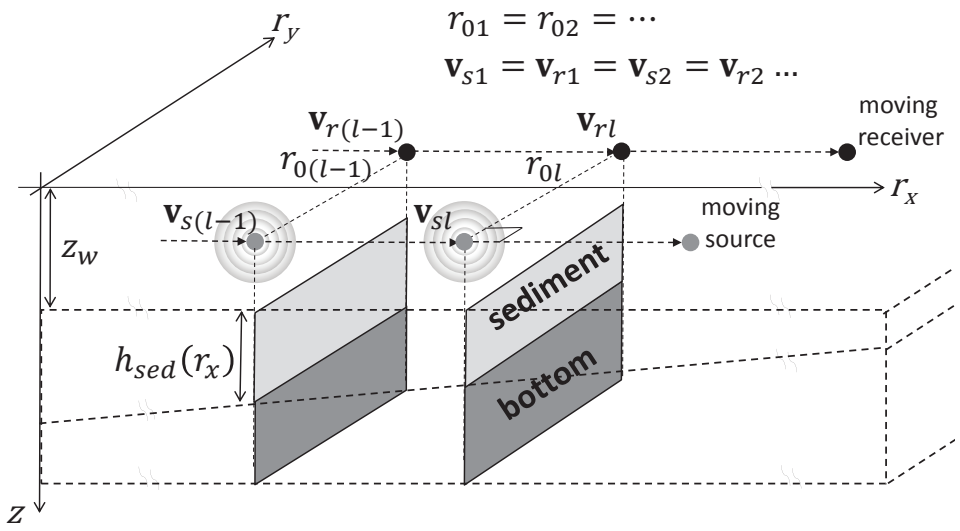

Figure 4.6: r_x and r_y are the horizontal axes where the origin is the source position at time zero when the source begins transmitting. Source and receiver are moving in the same r_x direction and at the same speed. The source-receiver separation is constant and the geoacoustic properties are assume range-independent in the r_y direction. Shown above are the source and receiver positions in the midst of gradual change in sediment thickness.

of pre-change-point measurements. This also is expected. Given a set of measurements derived from a model with a gradually changing parameter, bisecting the measurements is probably the best way to approximate the gradual parameter change with two constant models $\mathbf{m}_1, \mathbf{m}_2$.

4.4 Conclusions

A key assumption for synthetic aperture matched field geoacoustic inversions is constant underlying model parameters. Because of the long-time coherent integration and source-receiver motion, change in the underlying model parameters due to time or space is anticipated. Modeling the change parametrically is the best approach but also adversely increases the inversion search dimension. Instead, a model parameter change-point detection method that detects abrupt or gradual change in model parameters can be utilized. Combining change-point detection and recursive Bayesian inversion has enabled a data-driven verification

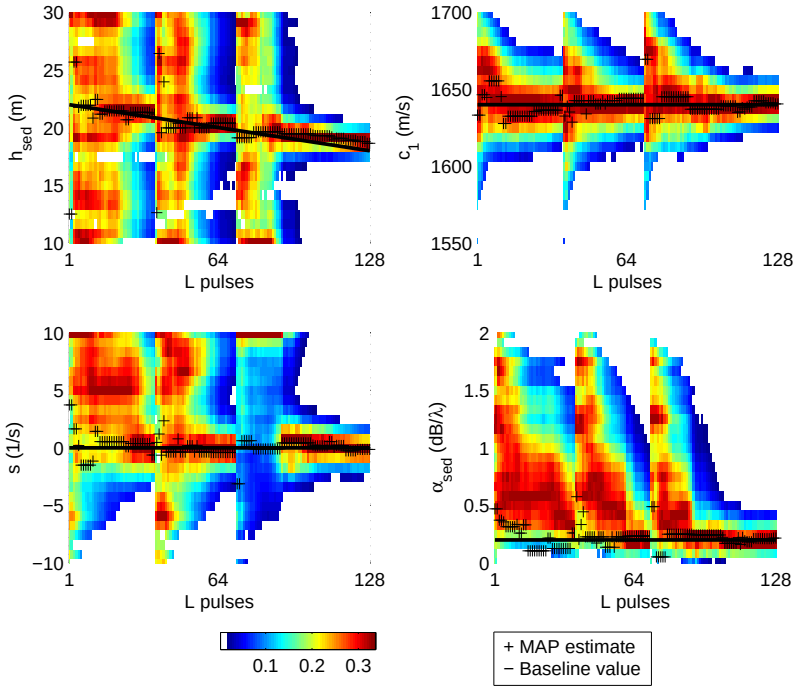

Figure 4.7: Evolution of 1-D marginal PPD with SNR fixed at 0 dB, and number of LFM pulses $L = 1$ to 128 with change-point detection. True sediment thickness changes gradually from 22 m to 17 m. Only the 95% HPD portion (non-white) PPD is plotted.

of the constant model parameter assumption. When a change-point is detected, the current inversion concludes and a new inversion is started using post change-point measurements. This method is demonstrated in simulation with parameters corresponding to the Shallow Water 2006 experiment.

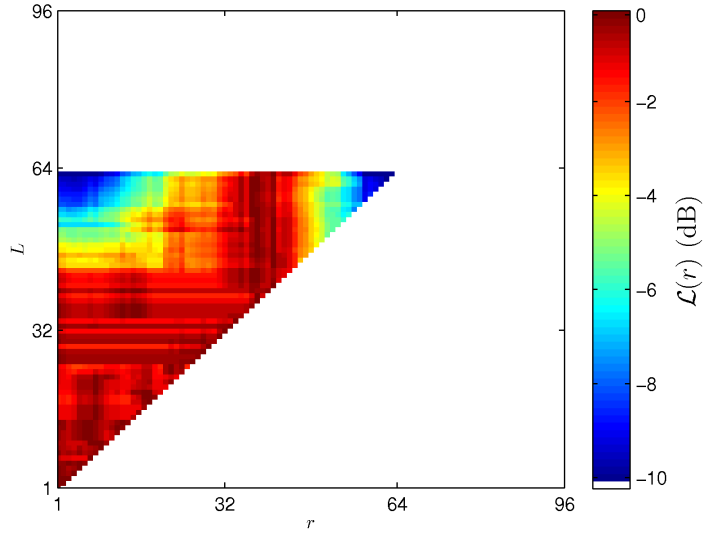

Figure 4.8: Evolution of change-point likelihood L with SNR fixed at 0 dB, and number of LFM pulses $L = 1$ to 63 with change-point detected on gradual change in H_{sed} ($\beta = 10$ dB) at $r = 41$ and $L = 63$.

Acknowledgments

This work was supported by the Office of Naval Research Grant No. N00014-11-0320 and the DSO National Laboratories of Singapore. Contents of Chapter 4, in full, are currently being prepared for submission for publication in the Journal of Acoustical Society of America as: B.A. Tan, P. Gerstoft, C. Yardim, W. Hodgkiss, "Change-point detection for recursive Bayesian geoacoustic inversion". The dissertation author is the primary author and investigator of this paper.

Chapter 5

Conclusion and Future Research

5.1 Conclusion

This dissertation presented a broadband, frequency-coherent matched-field inversion approach that exploits coherently repeated transmissions at low SNR for a moving source and receiver. The approach involves long-time coherent integration of multiple broadband transmissions, recasting dynamic time-varying geometric model parameters into initial-value and constant parameters via a trajectory-based waveguide Doppler normal mode model and assumes constant underlying geophysical model parameters. The long observation time creates a synthetic aperture due to relative source-receiver motion. The source transmission consists of multiple LFM pulses with a spectrum that approaches a multi-tonal comb with increasing Doppler sensitivity as the number of pulses increase. As a result, this requires incorporating waveguide Doppler in normal mode theory. The waveguide Doppler inversion approach was demonstrated with low SNR data from the Shallow Water 2006 experiment with a moving source and a static receiver configuration and 100–900 Hz LFM pulse transmissions. The inversion results agreed well with published results from the same experimental site. On the other hand, not incorporating waveguide Doppler in the inversion resulted in biases in the estimator such as a –100 m/s deviation in the sediment sound speed and larger uncertainties due to a poorer fit forward model.

Subsequently, a recursive Bayesian pulse-by-pulse approach to the inversion

problem was developed. This enabled accommodating an approximation for a horizontally accelerating source and receiver as well as generating a time-evolving uncertainty analysis of the model parameters. Through simulation and data analysis from the Shallow Water 2006 experiment, it was demonstrated that: (1) via online uncertainty analysis, parameter uncertainty reduces with an increasing number of pulses and (2) when source/receiver acceleration exists, modeling acceleration in the inversion can reduce further parameter estimation biases and uncertainties.

A key assumption for both methods in the above is constant underlying model parameters. Because of the long-time coherent integration and source-receiver motion, change in the underlying model parameters due to time or space is anticipated. Modeling the change parametrically is the best approach but also adversely increase the inversion search dimension. Instead, a model parameter change-point detection method that detects abrupt or gradual change in model parameters is utilized. Combining change-point detection and recursive Bayesian inversion has enabled a data-driven verification of the constant model parameter assumption. When a change-point is detected, the current inversion concludes and a new inversion is started using post change-point measurements. This is demonstrated in simulation of the Shallow Water 2006 experiment.

5.2 Future Work

Listed below are some possible extension to the work done in this dissertation

- The waveguide Doppler model also is applicable for the adiabatic range-dependent normal mode model [30]. A broadband synthetic aperture geoacoustic inversion study in a range-dependent environment would be relevant to many environments. Combining change-point detection for recursive Bayesian geoacoustic inversion and a range-dependent waveguide Doppler normal mode model will facilitate inversions being conducted in a space-time varying environment.

- In a shallow water waveguide, the spatial diversity is much higher in the

vertical direction than in the horizontal direction. The spatial diversity gain by adding vertical motion to a moving source or receiver in a geoacoustic inversion context will be significant. Using a slow moving AUV glider (typical speed is 0.4-0.6 m/s horizontally and vertically) in a synthetic aperture geoacoustic inversion is a potential extension to this research.

- The current change-point detection method is able to detect change in the model parameters but is unable to determine the specific model parameters that have changed. Developing a change-point method to also determine which parameters have changed would be useful. Knowing the changed model parameters is beneficial as it allows the posterior density of the unchanged model parameters from the pre-change-point inversion to propagate as the prior density in the post-change-point inversion when a change-point is detected.

Bibliography

[1] P. Nielsen and W. Fox, "Seabed characterization for mine hunting sonar performance and mine burial predictions," NATO Science and Technology Organization, Centre for Maritime Research and Experimentation, La Spezia, Italy, Tech. Rep. CMRE-FR-2013-002, 2013.

[2] Y. H. Goh, P. Gerstoft, W. S. Hodgkiss, and C.-F. Huang, "Statistical estimation of transmission loss from geoacoustic inversion using a towed array," *J. Acoust. Soc. Am.*, vol. 122, no. 5, pp. 2571–2579, 2007.

[3] C.-F. Huang, P. Gerstoft, and W. S. Hodgkiss, "Validation of statistical estimation of transmission loss in the presence of geoacoustic inversion uncertainty," *J. Acoust. Soc. Am.*, vol. 120, no. 4, pp. 1932–1941, 2006.

[4] C. Debever and W. A. Kuperman, "Robust matched-field processing using a coherent broadband white noise constraint processor," *J. Acoust. Soc. Am.*, vol. 122, no. 4, pp. 1979–1986, 2007.

[5] S. M. Jesus, M. B. Porter, Y. Stephan, X. Demoulin, O. C. Rodriguez, and E. M. M. F. Coelho, "Single hydrophone source localization," *IEEE J. Oceanic Eng.*, vol. 25, no. 3, pp. 337–346, 2000.

[6] J. A. Fawcett and S. E. Dosso, "Inversion for a moving spherical target's positional, structural, and speed parameters." *J. Acoust. Soc. Am.*, vol. 134, no. 1, pp. 67–76, Jul. 2013.

[7] Y.-S. Lai and N. C. Makris, "Spectral and modal formulations for the Doppler-shifted field scattered by an object moving in a stratified medium," *J. Acoust. Soc. Am.*, vol. 113, no. 1, pp. 223–244, 2003.

[8] J. Bonnel, C. Gervaise, B. Nicolas, and J. I. Mars, "Single-receiver geoacoustic inversion using modal reversal," *J. Acoust. Soc. Am.*, vol. 131, no. 1, pp. 119–128, 2012.

[9] J. Bonnel and N. R. Chapman, "Geoacoustic inversion in a dispersive waveguide using warping operators," *J. Acoust. Soc. Am.*, vol. 130, no. 2, pp. EL101–EL107, 2011.

[10] J. Bonnel, B. Nicolas, J. I. Mars, and S. C. Walker, "Estimation of modal group velocities with a single receiver for geoacoustic inversion in shallow water," *J. Acoust. Soc. Am.*, vol. 128, no. 2, pp. 719–727, 2010.

[11] C. Gervaise, B. G. Kinda, J. Bonnel, Y. Stephan, and S. Vallez, "Passive geoacoustic inversion with a single hydrophone using broadband ship noise," *J. Acoust. Soc. Am.*, vol. 131, no. 3, pp. 1999–2010, 2012.

[12] N. F. Josso, C. Ioana, J. I. Mars, and C. Gervaise, "Source motion detection, estimation, and compensation for underwater acoustics inversion by wideband ambiguity lag-Doppler filtering," *J. Acoust. Soc. Am.*, vol. 128, no. 6, pp. 3416–3425, 2010.

[13] N. F. Josso, C. Ioana, J. I. Mars, C. Gervaise, and Y. Stephan, "On the consideration of motion effects in the computation of impulse response for underwater acoustics inversion," *J. Acoust. Soc. Am.*, vol. 126, no. 4, pp. 1739–1751, 2009.

[14] J. C. Le Gac, M. Asch, Y. Stephan, and X. Demoulin, "Geoacoustic inversion of broad-band acoustic data in shallow water on a single hydrophone," *IEEE J. Oceanic Eng.*, vol. 28, no. 3, pp. 479–493, 2003.

[15] P. Hursky, M. B. Porter, M. Siderius, and V. K. McDonald, "High-frequency (8-16 kHz) model-based source localization," *J. Acoust. Soc. Am.*, vol. 115, no. 6, pp. 3021–3032, 2004.

[16] J. P. Hermand, "Broad-band geoacoustic inversion in shallow water from waveguide impulse response measurements on a single hydrophone: theory and experimental results," *IEEE J. Oceanic Eng.*, vol. 24, no. 1, pp. 41–66, 1999.

[17] O. Carriere and J.-P. Hermand, "Sequential Bayesian geoacoustic inversion for mobile and compact source-receiver configuration," *J. Acoust. Soc. Am.*, vol. 131, no. 4, pp. 2668–2681, 2012.

[18] M. Siderius, P. Gerstoft, and P. L. Nielsen, "Broadband geo-acoustic inversion from sparse data using genetic algorithms," *J. Comp. Acoust.*, vol. 6, pp. 117–134, 1998.

[19] G. V. Frisk, J. F. Lynch, and S. D. Rajan, "Determination of compressional wave speed profiles using modal inverse techniques in a range-dependent environment in Nantucket sound," *J. Acoust. Soc. Am.*, vol. 86, no. 5, pp. 1928–1939, 1989.

[20] S. D. Rajan, G. V. Frisk, K. M. Becker, J. Lynch, G. R. Potty, and J. H. Miller, "Modal inverse techniques for inferring geoacoustic properties in shallow water," in *Important Elements in: Geoacoustic Inversion, Signal Processing, and*

Reverberation in Underwater Acoustics 2008, A. Tolstoy, Ed. India: Research Signpost, 2008, ch. 7, pp. 165–234.

[21] D. P. Massa and J. I. Arvelo, "A wideband moving coil electrodynamic transducer system for autonomous underwater vehicle-based geoacoustic inversion," *J. Acoust. Soc. Am.*, vol. 132, no. 3, pp. 1920–1920, 2012.

[22] P. L. Nielsen, C. W. Holland, and L. Troiano, "Geoacoustic characterization and bottom scattering measurements using an autonomous underwater vehicle," NATO Science and Technology Organization, Centre for Maritime Research and Experimentation, La Spezia, Italy, Tech. Rep. CMRE-FR-2012-005, 2012.

[23] P. L. Nielsen, M. Siderius, J. Miller, S. Crocker, and J. Giard, "Seabed characterization using ambient noise and compact arrays on an autonomous underwater vehicle," *ICA 2013 Montreal*, vol. 19, no. 1, p. 070030, 2013.

[24] C. W. Holland, P. L. Nielsen, J. Dettmer, and S. Dosso, "Resolving mesoscale seabed variability using reflection measurements from an autonomous underwater vehicle," *J. Acoust. Soc. Am.*, vol. 131, no. 2, pp. 1066–1078, 2012.

[25] N. P. Chotiros and V. Pallayil, "Seabed characterization using acoustic communication signals on an autonomous underwater vehicle with a thin-line towed array," *IEEE J. Oceanic Eng.*, pp. 410–418, 2013.

[26] B. A. Tan, P. Gerstoft, C. Yardim, and W. S. Hodgkiss, "Broadband synthetic aperture geoacoustic inversion," *J. Acoust. Soc. Am.*, vol. 134, no. 1, pp. 312–322, 2013.

[27] K. E. Hawker, "A normal mode theory of acoustic Doppler effects in the oceanic waveguide," *J. Acoust. Soc. Am.*, vol. 65, no. 3, pp. 675–681, 1979.

[28] H. C. Song and A. B. Baggeroer, "The resolution of modal Doppler shifts in a dispersive oceanic waveguide," *J. Acoust. Soc. Am.*, vol. 88, no. 1, pp. 268–282, 1990.

[29] H. Schmidt and W. A. Kuperman, "Spectral and modal representations of the Doppler-shifted field in ocean waveguides," *J. Acoust. Soc. Am.*, vol. 96, no. 1, pp. 386–395, 1994.

[30] F. B. Jensen, W. A. Kuperman, M. B. Porter, and H. Schmidt, *Computational Ocean Acoustic*, 2nd ed., ser. Modern Acoustics and Signal Processing. New York: Springer, 2011, pp. 623–629.

[31] P. B. Weichman, "Doppler effects in heterogeneous media with applications to ocean acoustic modeling," *Phys. Rev. E*, vol. 72, no. 6, p. 066602, 2005.

[32] M. H. Brill, "Nonreciprocity of acoustic Doppler effect: Proof and physical mechanism," *Phys. Essays*, vol. 24, p. 570, 2011.

[33] S. D. Rajan, J. A. Doutt, and W. M. Carey, "Inversion for the compressional wave speed profile of the bottom from synthetic aperture experiments conducted in the Hudson canyon area," *IEEE J. Oceanic Eng.*, vol. 23, no. 3, pp. 174–187, 1998.

[34] K. Ohta, K. Okabe, I. Morishita, G. V. Frisk, and A. Turgut, "Modal inversion analysis for geoacoustic properties of the New Jersey continental shelf in the SWAT experiments," *IEEE J. Oceanic Eng.*, vol. 34, no. 4, pp. 526–538, 2009.

[35] C. Yardim, P. Gerstoft, and W. S. Hodgkiss, "Statistical maritime radar duct estimation using hybrid genetic algorithm Markov Chain Monte Carlo method," *Radio Science*, vol. 42, no. 3, p. RS3014, Jun. 2007.

[36] R. Duda, P. Hart, and D. Stork, *Pattern Classification*, 2nd ed. New York: Wiley, 2001, pp. 97-98, 531-534.

[37] J. Bonnel, S. E. Dosso, and N. Ross Chapman, "Bayesian geoacoustic inversion of single hydrophone light bulb data using warping dispersion analysis," *J. Acoust. Soc. Am.*, vol. 134, no. 1, p. 120, Jul. 2013.

[38] A. F. M. SMITH, "A Bayesian approach to inference about a change-point in a sequence of random variables," *Biometrika*, vol. 62, no. 2, pp. 407–416, 1975. [Online]. Available: http://biomet.oxfordjournals.org/content/62/2/407.abstract

[39] J. J. K. Ruanaidh and W. J. Fitzgerald, *Numerical Bayesian methods applied to signal processing.* New York: Springer, 1996, pp. 96-121.

[40] P. Fearnhead and Z. Liu, "On-line inference for multiple changepoint problems," *Journal of the Royal Statistical Society: Series B (Statistical Methodology)*, vol. 69, no. 4, pp. 589–605, 2007.

[41] R. P. Adams and D. J. MacKay, "Bayesian online changepoint detection," Cambridge, UK, 2007.

[42] J. Mellor and J. Shapiro, "Thompson sampling in switching environments with Bayesian online change detection," in *Proceedings of the Sixteenth International Conference on Artificial Intelligence and Statistics*, 2013, pp. 442–450.

[43] F. Caron, A. Doucet, and R. Gottardo, "On-line changepoint detection and parameter estimation with application to genomic data," *Statistics and Computing*, vol. 22, no. 2, pp. 579–595, Apr. 2012.

[44] A. Pierce, *Acoustics: an introduction to its physical principles and applications*. New York: Acoustical Society of America, 1989, p. 454.

[45] H. Schmidt, "OASES version 3.1: User guide and reference manual," 2004.

[46] M. B. Porter, "The KRAKEN normal mode program," SACLANTCEN Memo. SM-245 (SACLANT Undersea Research Centre, La Spezia, Italy, 1991, chap. 2.

[47] C. Soares and S. M. Jesus, "Broadband matched-field processing: Coherent and incoherent approaches," *J. Acoust. Soc. Am.*, vol. 113, no. 5, pp. 2587–2598, 2003.

[48] C. Soares, S. M. Jesus, and E. Coelho, "Environmental inversion using high-resolution matched-field processing," *J. Acoust. Soc. Am.*, vol. 122, no. 6, pp. 3391–3404, 2007.

[49] S. E. Dosso, P. L. Nielsen, and M. J. Wilmut, "Data error covariance in matched-field geoacoustic inversion," *J. Acoust. Soc. Am.*, vol. 119, no. 1, pp. 208–219, 2006.

[50] C.-F. Huang, P. Gerstoft, and W. S. Hodgkiss, "On the effect of error correlation on matched-field geoacoustic inversion," *J. Acoust. Soc. Am.*, vol. 121, no. 2, pp. EL64–EL69, 2007.

[51] A. Papoulis and S. Pillai, *Probability, random variables, and stochastic processes*, 4th ed. New York: McGraw-Hill, 2002, p. 515,519.

[52] C.-F. Huang, P. Gerstoft, and W. S. Hodgkiss, "Uncertainty analysis in matched-field geoacoustic inversions," *J. Acoust. Soc. Am.*, vol. 119, no. 1, pp. 197–207, 2006.

[53] ——, "Effect of ocean sound speed uncertainty on matched-field geoacoustic inversion," *J. Acoust. Soc. Am.*, vol. 123, no. 6, pp. EL162–EL168, 2008.

[54] Y.-M. Jiang and N. R. Chapman, "Bayesian geoacoustic inversion in a dynamic shallow water environment," *J. Acoust. Soc. Am.*, vol. 123, no. 6, pp. EL155–EL161, 2008.

[55] J. W. Choi, P. H. Dahl, and J. A. Goff, "Observations of the R reflector and sediment interface reflection at the shallow water '06 central site," *J. Acoust. Soc. Am.*, vol. 124, no. 3, pp. EL128–EL134, 2008.

[56] C. Park, W. Seong, P. Gerstoft, and W. S. Hodgkiss, "Geoacoustic inversion using backpropagation," *IEEE J Oceanic Eng.*, vol. 35, no. 4, pp. 722–731, 2010.

[57] C. Yardim, P. Gerstoft, and W. S. Hodgkiss, "Range aliasing in frequency coherent geoacoustic inversion," *J. Acoust. Soc. Am.*, vol. 130, no. 4, pp. EL154–EL160, 2011.

[58] C. H. Harrison, "The relation between the waveguide invariant, multipath impulse response, and ray cycles," *J. Acoust. Soc. Am.*, vol. 129, no. 5, pp. 2863–2877, 2011.

[59] J. P. Hermand and W. I. Roderick, "Acoustic model-based matched filter processing for fading time-dispersive ocean channels: theory and experiment," *IEEE J. Oceanic Eng.*, vol. 18, no. 4, pp. 447–465, 1993.

[60] D. Tollefsen and S. E. Dosso, "Bayesian geoacoustic inversion of ship noise on a horizontal array," *J. Acoust. Soc. Am.*, vol. 124, no. 2, pp. 788–795, 2008.

[61] P. Gerstoft and D. F. Gingras, "Parameter estimation using multifrequency range-dependent acoustic data in shallow water," *J. Acoust. Soc. Am.*, vol. 99, no. 5, pp. 2839–2850, 1996.

[62] D. Jackson and M. Richardson, *High-Frequency Seafloor Acoustics*. New York: Springer, 2010, pp. 123–151.

[63] S. C. Walker, P. Roux, and W. A. Kuperman, "Modal Doppler theory of an arbitrarily accelerating continuous-wave source applied to mode extraction in the oceanic waveguide," *J. Acoust. Soc. Am.*, vol. 122, no. 3, pp. 1426–1439, 2007.

[64] C. Yardim, P. Gerstoft, and W. S. Hodgkiss, "Geoacoustic and source tracking using particle filtering: Experimental results," *J. Acoust. Soc. Am.*, vol. 128, no. 1, pp. 75–87, 2010.

[65] ——, "Sequential geoacoustic inversion at the continental shelfbreak," *J. Acoust. Soc. Am.*, vol. 131, no. 2, pp. 1722–1732, 2012.

[66] A. Doucet, S. Godsill, and C. Andrieu, "On sequential Monte Carlo sampling methods for Bayesian filtering," *Statistics and Computing*, vol. 10, no. 3, pp. 197–208, Jul. 2000.

[67] B. Ristic, S. Arulampalam, and N. Gordon, *Beyond the Kalman Filter: Particle Filters for Tracking Applications*. Boston: Artech House, 2004, pp. 35-39.

[68] D. Lee and N. Chia, "A particle algorithm for sequential Bayesian parameter estimation and model selection," *IEEE Trans. Sig. Proc.*, vol. 50, no. 2, pp. 326–336, 2002.

[69] C. Yardim, Z. H. Michalopoulou, and P. Gerstoft, "An overview of sequential Bayesian filtering in ocean acoustics," *IEEE J. Oceanic Eng.*, vol. 36, no. 1, pp. 71–89, 2011.

[70] J. Geweke, "Bayesian inference in econometric models using Monte Carlo integration," *Econometrica1*, vol. 57, no. 6, pp. 1317–1339, 1989.

[71] J. J. K. Ruanaidh and W. J. Fitzgerald, *Numerical Bayesian methods applied to signal processing.* New York: Springer, 1996, pp. 31, 51-61.

[72] D. J. C. MacKay, *Information Theory, Inference and Learning Algorithms.* Cambridge: Cambridge University Press, 2003, pp. 357-364.

[73] P. Gerstoft and C. F. Mecklenbrauker, "Ocean acoustic inversion with estimation of a posteriori probability distributions," *J. Acoust. Soc. Am.*, vol. 104, no. 2, pp. 808–819, 1998.

[74] A. B. Owen, "Monte Carlo theory, methods and examples," 2013, Chap. 9 and 10. [Online]. Available: ://statweb.stanford.edu/ owen/mc/

[75] O. Cappé, R. Douc, A. Guillin, J.-M. Marin, and C. P. Robert, "Adaptive importance sampling in general mixture classes," *Statistics and Computing*, vol. 18, no. 4, pp. 447–459, Apr. 2008.

[76] C. Harrison and M. Siderius, "Effective parameters for matched field geoacoustic inversion in range-dependent environments," *IEEE J. of Oceanic Eng.*, vol. 28, no. 3, pp. 432–445, Jul. 2003.

[77] B. A. Tan, P. Gerstoft, C. Yardim, and W. S. Hodgkiss, "Recursive Bayesian synthetic aperture geoacoustic inversion in the presence of motion dynamics," *J. Acoust. Soc. Am.*, vol. -, no. -, pp. –, 2014, in press.